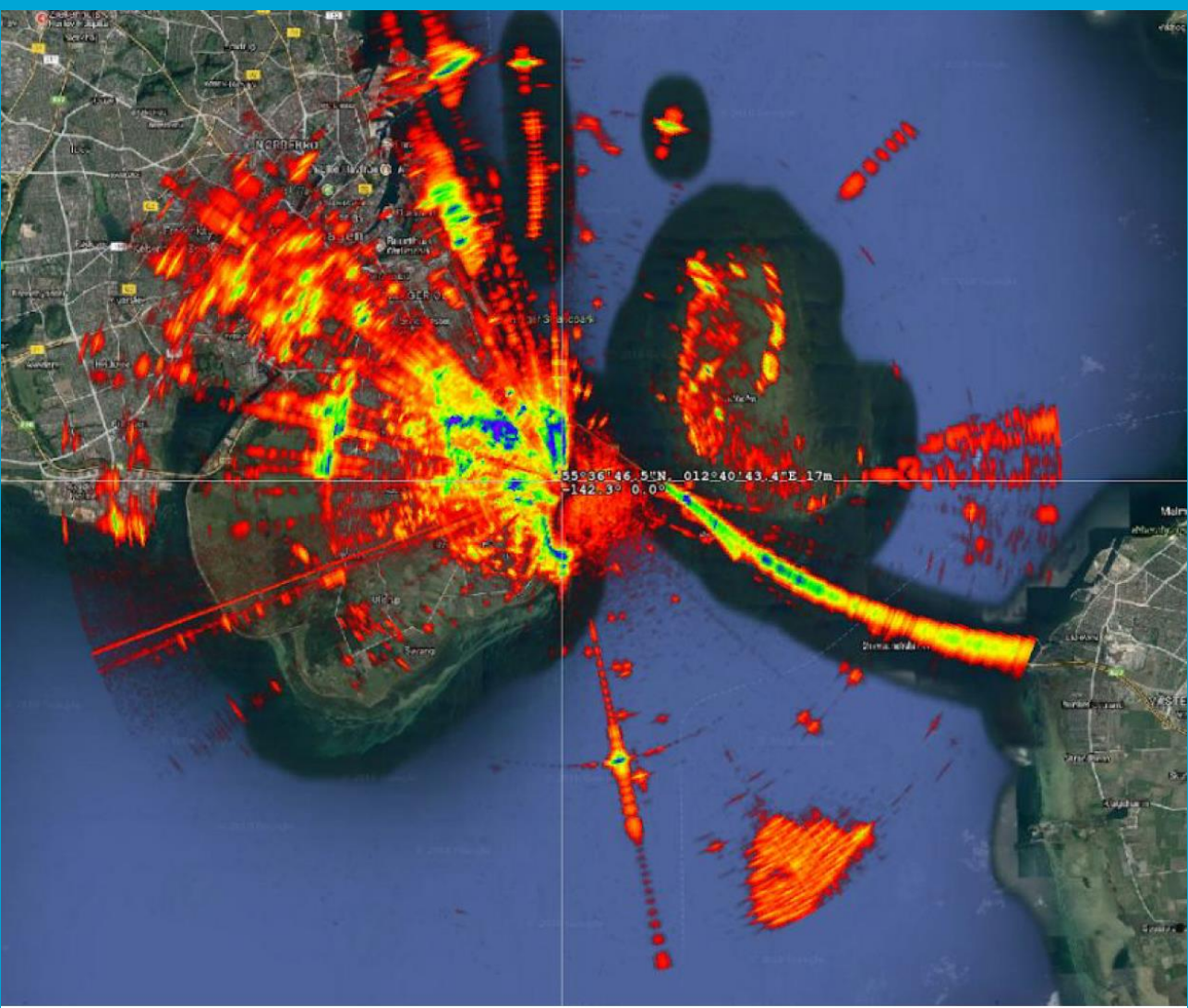


USER-CENTRIC DATA PROCESSING FOR HIGH RESOLUTION METEOROLOGICAL PHASED ARRAY RADAR



USER-CENTRIC DATA PROCESSING FOR HIGH RESOLUTION METEOROLOGICAL PHASED ARRAY RADAR

Thesis

submitted to

Faculty of Electrical Engineering, Mathematics, and Computer Science

in partial fulfillment of the requirements for the degree of
Master of Science

in

Electrical Engineering

by

Wenyi LU

Student number 5406536
Research group Microwave Sensing,
 Signals and Systems
Project duration November 2022 - August 2023
Thesis committee Prof. Dr. Alexander Yarovoy
 Asst. Prof. Dr. Oleg A. Krasnov
 Assoc. Prof. Dr. Marc Schleiss

TU Delft, Chair MS3
TU Delft, MS3, supervisor
TU Delft, Geoscience and
Remote Sensing



August 2023

PREFACE

I would like to express my sincere gratitude to all people who have contributed to my entire thesis period.

First and foremost, I extend my heartfelt gratitude to Prof. Oleg Krasnov. I am sincerely thankful for granting me the chance to participate in a summer research project and also for allowing me to work on this thesis project. Your mentorship and guidance at every step of the thesis have been invaluable, and I deeply appreciate your willingness to address all my inquiries. Moreover, I am truly grateful for the comprehensive courses on radars and electrical wave propagation that you provided, as they have been instrumental in my growth. Having you as my mentor brings me immense joy and satisfaction.

I express my gratitude to Ph.D. Tworit Dash for your unwavering assistance and support throughout this journey. Your encouragement at every stage of the thesis has been truly invaluable. Thank you for being a pillar of support and inspiration.

I thank the following MS3 group members: Dr. Alexander Yarovoy, thank you for the courses on radar applications. Dr. F. Fioranelli, thank you for the course object classification with radar. Dr.ir. J.N. Driessen, thank you for the course sensor signal and data processing and radar theory. Dr. Y. Aslan, thank you for the course antenna design. Ing. F. van der Zwan, thank you for helping me with the software installation issues. Ir. P.J. Aubry, thank you for the guidance and instructions on MATLAB during several courses in my first year of master's. Ph.D. Ignacio Roldan, thank you for managing the seminars. And the secretary of MS3, Esther de Klerk, thank you for all the guidance on administrative aspects to help arrange my defense.

I thank all my friends in MS3: Xiangwen Wang, and Huixuan Chen, thank you for all the discussions and fun activities.

I thank ing. A.P. Frehe: Thank you for your guidance on using the servers at MS3.

I thank my friends outside the MS3 group: Yue Ju, thank you for always being there from the beginning of my master's studies. When I was going through difficulties, you accompanied me, comforted me, and gave me enough warmth so that I could maintain a stable mood for my thesis project. Thank you for accompanying me for more than nine years. Yuan Wang, Haiyan Wang, I thank you for your suggestions about my career as senior. I thank Yuanyuan Hsin for all the caring.

Last but not least, I would like to extend my deepest gratitude and heartfelt thanks to my mother, Qin Gu, who gave me my life. Thank you for always cheering me on. I thank all my family members for their support and encouragement during the creation of this thesis project. Their love and understanding have been a source of strength for me, motivating me to push my limits and achieve my goals. Their patience and understanding in the late nights and busy days made this effort possible, and I am forever grateful for their sacrifice. To my parents (Qin Gu and Xiaojian Lu), your belief in my abilities inspires me to pursue this cause with passion and dedication.

I would like to express my gratitude to all the researchers and practitioners who have contributed to the development of radar technology and signal processing techniques. Their dedication and pioneering work have laid the foundation for this research.

Thank you for reading this report.

Wenyi Lu
Delft, August 2023

ABSTRACT

This thesis project is centered around the retrieval of meteorological parameters using a fast-scanning phased array radar, specifically targeting precipitation-like objects such as raindrops. The main objective is to transform radar data into variables that accurately characterize precipitation. This endeavor involves addressing various challenges, including extracting meteorological object-related variables, mapping targets from noisy radar measurements affected by phase noise, and resolving the issue of Doppler aliasing. In this report, these challenges are tackled by introducing a range of techniques and algorithms designed to enhance radar data analysis and validate the proposed methods.

The most commonly derived radar parameters for meteorological targets, known as Doppler moments, are extensively discussed, including reflectivity, mean Doppler velocity and Doppler spectrum width. An exploration of the circular calculation of Doppler spectra moments is conducted, providing valuable insights into the velocity distribution of radar targets. By analyzing higher-order moments, the characteristics and dynamics of the targets can be better understood, leading to improved target identification and tracking.

Additionally, a novel circular variance-based target mapping technique is proposed to map targets from noisy radar measurements effectively. This approach proves particularly well-suited for scenarios where traditional reflectivity-based methods fall short.

Apart from the circular variance-based technique, this thesis explores reflectivity-based target mapping approaches that offer enhanced methods for identifying and classifying different target parts. Two pipelines are proposed: the morphology-based pipeline and the entropy-based pipeline. Through simulation and real-world data analysis, the pros and cons of each pipeline are carefully evaluated. The second pipeline demonstrates significant benefits in classification, allowing for a more detailed and accurate representation of radar returns. It effectively distinguishes point targets, extended targets of interest, global noise, and phase noise, enabling a more comprehensive analysis of radar data and enhancing the interpretation of detected targets.

Furthermore, the critical issue of Doppler dealiasing is thoroughly investigated, addressing the problem of velocity ambiguity caused by the Nyquist limit. Three approaches are compared: gradient-based, existing advanced technique UNRAVEL, and optimizer-based. Based on the evaluation of the simulation model, the "ParticleSwarm" optimization approach is selected as the most effective in enhancing velocity measurements in severe weather conditions.

Throughout this report, experimental results are presented, findings are discussed, and recommendations and suggestions for future research are provided. The proposed techniques and algorithms have undergone rigorous evaluation and validation using both simulated data and real-world radar measurements. Overall, this research contributes valuable insights into radar data processing for meteorological applications, of-

fering improved accuracy and reliability for various weather-related analyses and forecasting tasks.

CONTENTS

Preface	v
Abstract	vii
List of Figures	xiii
List of Tables	xvii
List of Abbreviations and Terms	xvii
1 Introduction	1
1.1 Background	1
1.2 Problem statement	2
1.3 Research objectives	3
1.4 Research Limitations	4
1.5 Outputs of This Research	4
1.6 Structure of this Report	4
2 Literature Review and Feasibility Study Analysis	7
2.1 Meteorological phased array radar data processing pipeline	8
2.2 Noise suppression and noise clipping algorithms	9
2.2.1 Adaptive clutter filtering	9
2.2.2 Temporal filtering	12
2.2.3 Spectral processing	14
2.2.4 Noise clipping	14
2.2.5 Denoising algorithms based on wavelet transform	15
2.2.6 Singular value decomposition (SVD)	17
2.3 Doppler De-aliasing Techniques	18
2.4 Conclusion	18
3 Application of Circular Statistics on the Doppler Spectrum	19
3.1 Weather-like Spectra and signals	19
3.2 Doppler spectral moments	20
3.3 Circular Statistics	21
3.4 Circular Estimation of Mean Doppler and Spectrum Width	22
3.5 Simulation Results and Validation for Mean Doppler and Spectrum Width Estimation	23
3.5.1 Mean Doppler Estimation	23
3.5.2 Spectrum Width Estimation	24

3.6	Circular Spectrum Moments of Real-world Data	27
3.7	Target Mapping Based on Circular Variance.	29
3.7.1	Circular Variance.	29
3.7.2	Sensitivity of Circular Variance on DPP	30
3.7.3	Target Mask for Real-world Data	32
3.8	Conclusion	33
4	Target Mapping Based on Reflectivity	35
4.1	Modeling objects in an image with a 2D Gauss function	35
4.2	Simulation Model Development in MATLAB	36
4.3	Morphology-based Target Mapping Pipeline	38
4.3.1	Point Targets Detection Using CFAR	38
4.3.2	Phase Noise Detection	39
4.3.3	Wavelet Denoise	39
4.3.4	Morphological Operation	41
4.3.5	Restoration of Phase Noise Azimuths	43
4.3.6	Gap Filling	44
4.3.7	Evaluation and Performance Analysis	44
4.4	Entropy-based Target Mapping Pipeline	46
4.4.1	Point Targets Detection Using CFAR along ranges	47
4.4.2	Thermal Noise Detection Using Rényi Entropy.	47
4.4.3	Phase Noise Detection	49
4.4.4	Evaluation and Performance Analysis	51
4.5	Comparison of Two Processing Pipelines	52
4.6	Final Target Mapping of the Real-world Data	53
4.6.1	Morphology-based Pipeline Applied on Real-World Data	53
4.6.2	Entropy-based Pipeline Applied on Real-World Data.	54
4.7	Final Target Mask	56
4.7.1	Target Masks	57
4.8	Conclusion	59
5	Doppler Dealiasing	61
5.1	Model Used to Evaluate the Doppler De-aliasing Techniques	63
5.2	Simple Algorithm to Eliminate Doppler Aliasing	64
5.2.1	Approach	64
5.2.2	Results	64
5.3	Advanced Existing De-aliasing Tool UNRAVEL	65
5.4	Doppler Dealiasing by Optimizer-based Approach	68
5.4.1	Development	69
5.4.2	Optimization Comparison	77
5.5	De-aliasing techniques comparison.	79
5.5.1	Optimization Result	80
5.6	Conclusions.	80
6	Conclusion and Recommendations	81
6.1	Conclusions.	81
6.2	recommendations	83

LIST OF FIGURES

2.1 Block Diagrams of Fast Wavelet Transform and Inverse Fast Wavelet Transform	16
3.1 Doppler spectrum With and Without the occurrence of Folding	23
3.2 Mean Estimation	23
3.3 Spectrum Width Estimation with Different Methods Given Mean = $1.5 \times$ Unambiguous Doppler	24
3.4 Spectrum Width Estimation Given Different Mean Doppler Using Linear Method	25
3.5 Spectrum Estimation Given Different Mean Doppler Using Circular Method with Batschelet's Equation	26
3.6 Spectrum Estimation Given Different Mean Doppler Using Circular Method with Mardia's Equation	26
3.7 Spectrum Width Estimation Given Different Mean Doppler Using Shift-back Method	27
3.8 Range-Doppler map of the received signal at a specific azimuth and elevation	28
3.9 Mean Doppler of Real-world Data Using Conventional Linear Method and Proposed Circular Method	28
3.10 Spectrum Width of Real-world Data Using Conventional Linear Method and Proposed Circular Method	29
3.11 Circular variance Derived from the Real-world Data	30
3.12 Modeling the Doppler Spectrum within One Range Gate	31
3.13 Sensitivity of Circular Variance on DPP Under Different Signal Standard Deviations	31
3.14 Apply Circular-variance Based Mask on Reflectivity	32
3.15 Apply Circular-variance Based Mask on Mean Doppler	32
4.1 Reflectivity Model in MATLAB	37
4.2 Point Target Mask and Result After Point Target Removal	38
4.3 Scaled Mean Along Range Dimension	39
4.4 Result After Removing Azimuths Existing Phase Noise	39
4.5 Result After Wavelet Denoising	41
4.6 Primary Binary Mask by Thresholding the Denoised Values and Removing Azimuths Existing Phase Noise	42
4.7 Binary Image After Applying Morphological Operation on the Primary Binary Mask	43
4.8 Result After Restoring Azimuths Existing Phase Noise with Zeros	43

4.9	Final Binary Mask Derived from the Simulation Model Using Morphology-based Target Mapping Pipeline	44
4.10	Model Used to Evaluate Target Mapping Pipelines at SNR = 20dB	45
4.11	Performance Measures Dependence on SNR for Morphological-based Target Mapping Pipeline	46
4.12	Decision Tree for Classifier (Entropy-based Target Mapping Pipeline)	47
4.13	Distribution Sets to Validate the Threshold Provided by Renyi's Entropy	48
4.14	Mask for Thermal Noise and Result After Removing Thermal Noise	49
4.15	Mask for Phase Noise Detected by CFAR	50
4.16	Scaled Mean Along the Range Dimension	50
4.17	Mask for Phase Noise	50
4.18	Result After Phase Noise Removal	50
4.19	Mask for Extended Targets	51
4.20	Performance Measures Dependence on SNR for Entropy-based Target Mapping Pipeline	52
4.21	Comparison of the Performance Measure for Morphology-based and Entropy-based Target Mapping Pipelines	53
4.22	Results of Morphology-based Pipeline on Real-world Data	54
4.23	Results of Entropy-based Pipeline on Real-world Data	55
4.24	Class Identification of Real-world Data Provided by Entropy-based Target Mapping Pipeline	56
4.25	Before and After-processed PPI for Real-world Reflectivity Using Entropy-based Target Mapping Pipeline	56
4.26	Mask Provided by Circular Variance of the Doppler Spectrum	57
4.27	Mask Provided by Entropy-based Target Mapping Pipeline on Reflectivity	57
4.28	Combination of the Mask Provided by Circular Variance and the Mask Provided by Entropy-based Target Mapping Pipeline on Reflectivity	58
4.29	Intersection of the Mask Provided by Circular Variance and the Mask Provided by Entropy-based Target Mapping Pipeline on Reflectivity	58
4.30	Union of the Mask Provided by Circular Variance and Mask Provided by Entropy-based Target Mapping Pipeline on Reflectivity	58
4.31	Apply Union of the Mask Provided by Circular Variance and Mask Provided by Entropy-based Target Mapping Pipeline on the Real-world Reflectivity	58
4.32	Reflectivity Model (target only)	59
4.33	Reflectivity Model (target only but with lower bound)	59
5.1	Demonstration of Raindrop Velocity with Elevation Angle Not Equal to Zero	63
5.2	Velocity at Azimuths with Occurrence of Doppler Folding	63
5.3	Doppler to dealiase	64
5.4	De-aliased Doppler Based on the Continuity Along Range	65
5.5	Results of UNRAVEL for Scenario: Targets Diffuse in All pixels and Targets Only	66
5.6	Results of UNRAVEL for Scenario: Targets Diffuse in All pixels and Targets, Thermal Noise Both Exist	66

5.7	Results of UNRAVEL for Scenario: Targets Diffuse in All pixels and Targets, Phase Noise Exist	66
5.8	Results of UNRAVEL for Scenario: Targets Diffuse in All Pixels and Targets, Thermal Noise and Phase Noise All Exist	67
5.9	Results of UNRAVEL for Scenario: Targets Diffuse in Certain Pixels and Targets, Thermal Noise and Phase Noise All Exist	68
5.10	Performance of "fmincon" Optimization for Different Actual Max Velocities	70
5.11	Performance of "fmincon" Optimization for Different Fluctuations Caused by Noise	70
5.12	Performance of "fmincon" Optimization for Different Fractions of Invalid Data Caused by Noise	71
5.13	Performance of "patternsearch" Optimization for Different Actual Max Velocities	72
5.14	Performance of "patternsearch" Optimization for Different Fluctuations Caused by Noise	72
5.15	Performance of "patternsearch" Optimization for Different Fractions of Invalid Data Caused by Noise	73
5.16	Dependence of Objective Function on Parameters for Optimization Process	74
5.17	Performance of "particleswarm" Optimization for Different Actual Max Velocities	75
5.18	Performance of "particleswarm" Optimization for Different Fluctuations Caused by Noise	76
5.19	Performance of "particleswarm" Optimization for Different Fractions of Invalid Data Caused by Noise	76
5.20	Dependence of Cost on Actual Max Velocity for Three Optimizers	77
5.21	Dependence of Cost on Fluctuation Caused by Noise for Three Optimizers	78
5.22	Dependence of Cost on Fraction of Invalid Data for Three Optimizers . . .	78
5.23	Comparison of De-aliasing Techniques	79
5.24	Before and After Optimization Doppler Velocity	80

LIST OF TABLES

4.1	Characteristics of the Four Classes in Radar Data	46
4.2	Summary of Performance Measures for Morphology-based and Entropy-based Pipelines	59
5.1	Performance of UNRAVEL	67
5.2	RMSE of Doppler De-aliasing Techniques	80

LIST OF ABBREVIATIONS AND TERMS

- AWF** Adaptive Wiener filtering. 9, 10
- AWOS** Automatic Weather Observation Stations. 12
- CFAR** Constant False Alarm Rate. 5, 9, 10, 14, 18, 38, 49, 50
- CUT** Cell Under Test. 38
- DPP** Difference between Peak of signal and Peak of noise. xiii, 19, 30, 31
- DWT** Discrete Wavelet Transform. 40
- FMCW** Frequency-Modulated Continuous Wave. 1–4, 8, 18, 23
- FN** False Negative. 45
- FWT** Fast Wavelet Transform. 15
- IDWT** Inverse Discrete Wavelet Transform. 40
- IFWT** Inverse Fast Wavelet Transform. 15
- IoU** Intersection over Union. 45
- MSE** Mean Square Error. 45, 50, 51, 68
- OCXO** Oven-controlled Crystal Oscillator. 2
- PSO** Particle Swarm Optimization. 74
- RMSE** Root Mean Square Error. 17, 18, 65–68
- SCC** Spectral Correlation Coefficient. 14
- SDA** Spectral Domain Averaging. 14
- SNFC** Spectral Noise Floor Clipping. 14
- SNR** Signal-to-Noise Ratio. 17, 18, 44–46, 51–53, 59

SVD Singular value decomposition. 7, 17, 18

TCXO Temperature-compensated Crystal Oscillator. 2

TP True Positive. 45

UNRAVEL Unfold RAdar VELOCITY algorithm. xiv, xv, xvii, 5, 18, 65–68

WGN White Gaussian Noise. 1, 44

1

INTRODUCTION

1.1. BACKGROUND

Meteorological observations are essential for weather forecasting and monitoring. In recent years, phased array FMCW (Frequency-Modulated Continuous Wave) radar systems have become increasingly popular for remote sensing of meteorological objects due to their ability to provide accurate and high-resolution data. These systems transmit a modulated continuous-wave signal and receive the scattered echoes from hydrometeors in the atmosphere, and then process the data to obtain information about the location, size, shape, and movement of the hydrometeors.

However, the raw data collected by the radar can be noisy and contain artifacts, bringing challenges to extracting meaningful information. Besides the WGN, which exists globally, phase noise could be another challenge. Phase noise refers to random fluctuations in the phase of the transmitted signal, which can cause distortion and degradation of the received signal. In FMCW radar, the transmitted signal is modulated with a frequency sweep, which is then transmitted and reflected back by the target. The received signal is mixed with the transmitted signal, and the difference frequency is measured to determine the range and velocity of the target. Any phase noise in the transmitted signal will also be present in the received signal, and this can affect the accuracy and resolution of the radar measurements. Phase noise in FMCW radar can arise from a variety of sources, including oscillator instability, thermal noise, and electromagnetic interference. The magnitude and frequency of the phase noise depend on the characteristics of the oscillator used in the radar system and the environmental conditions. In range-Doppler radar systems, phase noise is an undesirable but unavoidable characteristic, adversely affecting the performance of the radar [1]. One of the influences is that phase noise in radar transmitters raises the noise floor around large targets, making impossible the detection and tracking of small targets nearby [2].

The Robin Radar's 3DMAX radar, working as a meteorological radar, is a phased array FMCW radar that is highly disturbed by thermal noise and additional phase noise. Therefore, this thesis project aims to develop a set of data processing algorithms to convert radar signals into a set of user-defined derivative variables. These variables are only

relevant to the perceptual objects that the user is interested in, with a specific level of precision and quality. In meteorological FMCW radars, Doppler processing is used to obtain information about the motion of precipitation particles within the observed weather volume, enabling the derivation of several important meteorological Doppler moments, such as reflectivity, mean Doppler velocity, and spectral width. Reflectivity measures the intensity of the radar signal reflected back from precipitation particles, providing insights into the size and number of particles within the radar's range. Mean Doppler velocity is a measure of the average velocity of precipitation particles along the direction of the radar beam. The spectral width provides information about the distribution of velocities within the observed weather volume. Analyzing the Doppler moment is critical for understanding the dynamics of precipitation systems and can be used for weather forecasting and monitoring.

1.2. PROBLEM STATEMENT

Despite the significant advancements in phased array FMCW radar systems, analyzing radar data is still challenging due to noise and interference. There are four significant challenges for this thesis project.

The first challenge is to compute the accurate Doppler spectrum related to the meteorological objects of interest.

The second one is to reduce the impact of noise on the radar data to improve the quality of the derived variables. Phase noise is a critical issue. One way to mitigate the effects of phase noise in FMCW radar is to use a stable and high-quality oscillator, such as a temperature-compensated crystal oscillator (TCXO) or an oven-controlled crystal oscillator (OCXO). These oscillators have low phase noise and high stability, which can improve the accuracy and resolution of the radar measurements. This approach is not applicable to this thesis project. Another approach is to use signal processing techniques, such as phase noise compensation algorithms, to remove the effects of phase noise from the received signal. These algorithms typically require additional hardware, such as a reference oscillator, and can be computationally intensive. Hence, the two approaches do not apply to this case since this project is focused on data processing. It requires a multi-dimensional analysis of the data. Target detection and noise-suppressing algorithms are developed based on the proper interpretation of the data. The proposed data processing algorithms must effectively suppress noise while preserving the object of interest, particularly at high-noise azimuth angles.

In remote sensing applications, ground truth data is often used as a reference to validate the accuracy of algorithms. However, obtaining ground truth data can be difficult or impossible, posing a significant challenge for algorithm validation. This is particularly true in meteorological radar systems, where it is difficult to obtain accurate ground truth data due to the nature of the observed meteorological phenomena. Thus the third challenge is to evaluate the performance of these algorithms in terms of their accuracy and quality and to propose improvements to the algorithms as needed.

Last but not least problem to be solved is Doppler de-aliasing. Doppler de-aliasing is a critical process in radar data processing that addresses a significant limitation known as the Nyquist limit. This limitation occurs when radar uses the Doppler effect to measure the speed of a moving target. The Doppler effect causes a change in the frequency

of the radar signal when it reflects off a moving object, such as a raindrop in the atmosphere. However, radar can only accurately measure speed within a specific range, called the "unambiguous speed range". Velocities outside this range can lead to an effect known as "aliasing", where measured velocities are misinterpreted due to the Nyquist limit.

1.3. RESEARCH OBJECTIVES

The goal of this project is to develop and implement a data processing algorithm for a phased array FMCW weather radar system that can effectively suppress noise and interference of radar data and provide users with preprocessed information that is easy to understand and of a certain quality. The proposed algorithm can be based on a combination of standard, adaptive, and other techniques and will be designed to handle large amounts of radar data. The performance of the algorithm will be evaluated using both simulated and real-world data, with a focus on its effectiveness in mitigating noise, object detection, improving the accuracy of wind speed measurements, and detecting objects of interest to the user. Based on this, the research objectives of this paper are as follows:

1. How to efficiently obtain precipitation-related parameters from radar data to enhance meteorological analysis?
This research question explores in depth the development of robust and accurate methods to extract important meteorological parameters from radar data, such as traditional Doppler spectrum moments. Its purpose is to explore innovative techniques to improve the precision of parameter derivation.
2. How effective is the target mapping pipeline, including clipping global thermal noise, detecting phase noise, and removing its effect on detecting extended targets in noisy radar measurements?
This research question focuses on evaluating the feasibility and performance of a specific radar data processing pipeline designed to enhance the detection of extended targets, such as large precipitation systems, in noisy radar surveys. Its purpose is to investigate the impact of each step in the pipeline (from thermal noise reduction to phase noise detection and cancellation) on the accuracy and reliability of object recognition. By quantifying the effectiveness of this pipeline, the study aims to provide insights for improving radar data quality and object mapping techniques.
3. What novel Doppler anti-aliasing techniques can be proposed to accurately resolve the velocity ambiguity induced by the Nyquist limit in Doppler radar measurements?
This research problem addresses a key challenge in Doppler radar data processing: the accurate estimation of velocities beyond the Nyquist limit. It seeks to explore innovative ways to mitigate the adverse effects of velocity aliasing through advanced mathematical algorithms or signal-processing techniques.
4. How can the proposed processing pipeline and techniques be rigorously validated to assess their reliability and performance in characterizing meteorological targets

and improving radar data analysis?

This research question validates the proposed radar data processing flow and technique. It aims to establish a comprehensive and systematic validation method to assess the reliability, accuracy, and overall performance of the developed method.

1.4. RESEARCH LIMITATIONS

Despite the potential benefits of the proposed data processing algorithms, there are several limitations to this research project. The first limitation is the dependence on the specific characteristics of the radar system being used. The proposed algorithms and techniques may not apply to other types of radar systems or atmospheric conditions. Secondly, the effectiveness of the proposed algorithms is subject to various factors, such as the quality and resolution of the raw radar data, the frequency of signal interference, the atmospheric conditions in the observed region, and the user-defined criteria for accuracy and quality. Other limitations include the computational complexity and practical implementation of the proposed algorithms in real-time radar systems. Moreover, while the proposed algorithms will enhance the accuracy and resolution of wind speed measurements, they may not fully address other limitations of phased array FMCW meteorological radar systems, such as their limited range and resolution.

1.5. OUTPUTS OF THIS RESEARCH

This research is concentrated on developing and applying data processing algorithms tailored for a phased array FMCW weather radar system. These algorithms are aimed to diminish the noise and phase noise interference within radar data while furnishing users with comprehensible preprocessed information. This study exclusively centers on objects resembling precipitation, specifically raindrops to convert phased array radar data into measurable quantities that help users characterize precipitation. To address the research problem defined previously, the outputs of this research compose of the following parts:

- Developed algorithms for the phase noise presence detection in the post-Doppler processed radar data;
- Developed algorithms for thermal noise detection and suppression, facilitating the target detection;
- Weather FMCW radar signal models for the validation of developed algorithms;
- Examples of processed data that were measured with Robin 3DMax Radar and results of provided analysis;
- MSc thesis report.

1.6. STRUCTURE OF THIS REPORT

The overview of the rest of the chapters in the report is provided below.

Chapter 2 provided an overview of the latest relevant research problems, including the typical data processing pipeline for the weather phased array radar, existing noise

suppression, and noise clipping algorithms. The developed Doppler de-aliasing techniques are studied.

Chapter 3 shows the importance and conventional estimation of Doppler spectrum moments, namely reflectivity, mean Doppler, and spectrum width. A novel estimation method based on circular statistics is proposed and validated with the developed model. The results of implementing this novel approach on Robin radar data are presented in detail. Moreover, the circular variance of the Doppler spectrum is demonstrated to be effective for filtering out the noise, facilitating to create the target binary masks. The target mask of the real-world data measure with Robin radar provided by the circular variance method is displayed.

Chapter 4 proposed two reflectivity-focused target mapping processing pipelines. The 2D Gaussian function-based model for object representation is developed to evaluate the two processing pipelines. The first processing pipeline is based on morphology and involves CFAR detection, phase elimination, wavelet denoising, morphological mapping, phase noise restoration, and gap filling. The second employs entropy-based radar data classification with CFAR detection, Renyi's Entropy for noise, and normalized mean for phase noise. Simulation evaluates both processing pipelines and real radar data results are presented.

Chapter 5 presents three Doppler de-aliasing methods, which are gradient-based algorithm, existing advanced UNRAVEL technique, and optimizer-based approach. Their performance is compared and evaluated by the developed Doppler azimuth curve model. In addition, the most suitable optimization algorithm is selected according to the evaluation results of the optimization method.

Finally, conclusions and recommendations are drawn in chapter 6.

2

LITERATURE REVIEW AND FEASIBILITY STUDY ANALYSIS

This chapter begins by exploring the processing pipeline for meteorological phased array radar data, highlighting its significance in enhancing radar measurements and extracting valuable information. Various steps and techniques involved in the pipeline are discussed, including adaptive clutter filtering, temporal filtering, spectral processing, noise clipping, denoising algorithms based on wavelet transform, and singular value decomposition (SVD).

The section on noise suppression and noise clipping algorithms presents an in-depth analysis of different approaches used to mitigate noise and interference in radar data. Adaptive clutter filtering techniques are investigated, which adaptively suppress clutter signals to improve the signal-to-noise ratio. Temporal filtering methods, which exploit the temporal correlation in radar data to remove noise, are also examined. Additionally, spectral processing techniques, such as filtering in the frequency domain, are discussed for noise reduction.

Moreover, the chapter explores noise-clipping techniques that aim to remove outliers and extreme values from radar data, improving data quality and enhancing subsequent analysis. Denoising algorithms based on the wavelet transform are investigated for their effectiveness in reducing noise while preserving essential signal features. The application of singular value decomposition (SVD) as a denoising technique is also explored, highlighting its potential to enhance radar data quality.

Furthermore, this chapter studies the developed Doppler de-aliasing techniques and analyzes their applicability to this situation.

Overall, This chapter provides a comprehensive overview of the existing literature on meteorological phased array radar data processing pipelines, various noise suppression and clipping algorithms, and Doppler de-aliasing techniques. The feasibility study in this chapter forms the foundation for the subsequent chapters, enabling the development of an improved radar data processing and analysis framework.

2.1. METEOROLOGICAL PHASED ARRAY RADAR DATA PROCESSING PIPELINE

As proposed in the book [3] and the article [4], the data processing pipeline for meteorological phased array FMCW radar is similar to that of traditional meteorological radar but with some additional steps specific to phased array technology. The following are the general steps involved in processing phased array FMCW radar data for meteorological applications:

- **Raw Data Acquisition** The first step is to acquire the raw radar data. The phased array FMCW radar emits a signal composed of multiple frequencies, and each array element receives the reflected signal. The received signals are digitized and stored as raw radar data.
- **Data Preprocessing** Similar to traditional meteorological radar, data preprocessing is used to remove noise, artifacts, and unwanted signals from the raw data. This can include range and velocity unfolding, clutter filtering, and attenuation correction.
- **Digital Beamforming** In phased array FMCW radar, the digital beamforming process is used to form a beam in the desired direction, which is achieved by weighing the received signals from each element of the array. The beamforming process can also improve the signal-to-noise ratio and reduce interference.
- **Doppler Processing** After the beamforming process, the Doppler processing algorithm is applied to the data. This step calculates the Doppler shift of the reflected signals to estimate the radial velocity of the targets in the radar field of view. The resulting Doppler moments include reflectivity, mean Doppler velocity, and Doppler spectral width.
- **Target Detection** The Doppler moments are then used in target detection algorithms to identify weather targets, such as raindrops or snowflakes, and to distinguish them from non-meteorological targets, such as birds or insects.
- **Product Generation** Finally, meteorological products such as reflectivity maps, velocity maps, and precipitation estimates can be generated using the target detection results. These products are used for weather forecasting, research, and monitoring.

Additionally, radar data quality control should be applied at various steps throughout the meteorological phased array FMCW radar data processing pipeline [5]. During data acquisition, quality control checks may be applied to the raw data as it is collected from the radar hardware to ensure that the data is appropriately sampled and that there are no issues with the hardware. In the stage of preprocessing, quality control checks may be applied to the preprocessed data to ensure that any noise or interference is removed correctly and that the data is appropriately calibrated. In the beamforming stage, quality control checks may be applied to the Doppler-processed data to ensure that the velocity and reflectivity data are accurate and that there are no spurious signals. As for

Doppler processing, quality control checks may be applied to the Doppler-processed data to ensure that the velocity and reflectivity data are accurate and that there are no spurious signals. The target detection stage requires quality control checks to ensure that the detected targets are valid and that there are no false alarms or missed targets.

As mentioned in the articles [6] and [7], some common quality control algorithms used in meteorological radar data processing are:

- **Data filtering**
This involves removing unwanted noise or interference from the data, such as ground clutter or noise from other sources. Filtering may be performed using techniques such as spectral analysis, wavelet analysis, or adaptive filtering.
- **Calibration**
This involves adjusting the data to account for any systematic errors in the radar hardware or data processing algorithms. Calibration may be performed using reference targets such as calibration spheres or known precipitation types.
- **Range and azimuth correction**
This involves correcting for any geometric distortions in the radar data due to the radar beam geometry or the curvature of the earth. Correction may be performed using geometric models or radar ray tracing.
- **Doppler velocity dealiasing**
This involves correcting for errors in the measured radial velocity due to the limited range of the Doppler velocity measurement. Velocity dealiasing may be performed using techniques such as velocity folding or phase unwrapping.
- **Signal quality assessment**
This involves evaluating the signal-to-noise ratio and other metrics of the radar signal quality to identify any data that may be corrupted or unreliable. This may be performed using techniques such as signal-to-noise ratio (SNR) analysis or signal power analysis.

2.2. NOISE SUPPRESSION AND NOISE CLIPPING ALGORITHMS

Noise suppression and noise clipping are essential aspects of phased array weather radar data processing, and various techniques have been developed for these purposes. Some commonly used techniques are introduced as follows.

2.2.1. ADAPTIVE CLUTTER FILTERING

This technique uses statistical methods to estimate the clutter in the radar data and then remove it. This technique has been widely used in phased array weather radar systems. Various adaptive clutter filtering algorithms have been developed, such as the constant false alarm rate (CFAR) algorithms, adaptive Wiener filtering (AWF), adaptive filtering based on morphological processing, the fuzzy logic-based algorithm, and the maximum likelihood algorithm.

CONSTANT FALSE ALARM RATE (CFAR) ALGORITHMS

In the book [8], CFAR algorithms have been introduced comprehensively. The core is to divide the radar range cell into several sub-cells and compares the power level in each sub-cell to the average power level of a certain number of neighboring sub-cells. If the power level of the target cell exceeds the threshold value, the cell is declared a target. The advantages and disadvantages are summarized in the following texts.

Advantages

- Easy to implement and computationally efficient.
- Can be used for both ground clutter and atmospheric clutter suppression.
- Can handle different clutter statistics and can adapt to changing clutter conditions.

Disadvantages

- Can produce false alarms in areas with high noise levels or non-homogeneous clutter distribution.
- Can have limited performance in complex terrain environments.

ADAPTIVE WIENER FILTERING (AWF)

In the article [9], AWF is introduced as a technique that employs an adaptive filter that adjusts its coefficients according to the characteristics of the input signal. The filter coefficients are updated iteratively based on the statistical properties of the signal and noise.

Advantages

- Can effectively suppress both ground clutter and atmospheric clutter.
- Can significantly improve signal-to-noise ratio and enhance target detection performance.
- Can be used for both stationary and non-stationary clutter environments.

Disadvantages

- High computational complexity and memory requirements.
- Requires an accurate estimate of the covariance matrix, which can be difficult to obtain in practice.
- Can introduce some distortion or artifacts in the filtered data.

ADAPTIVE FILTERING BASED ON MORPHOLOGICAL PROCESSING

This technique is based on mathematical morphology, which is a non-linear signal processing technique that uses the shape and structure of the signal to extract useful information. The morphological filter is applied to the input signal, and the resulting signal is compared to a threshold value to detect targets. [10] develops an approach for robustly detecting targets of different sizes and shapes (fixed/non-fixed), using a combination of image frame time difference, deep-threshold, target shape, and size analysis with non-linear morphological operations.

Advantages

- Can effectively suppress ground clutter and preserve the target signals.
- Can be used for both range and Doppler filtering.
- Can be robust to noise and outliers.

Disadvantages

- Can be sensitive to the choice of structural element or kernel.
- Can introduce some smoothing or blurring effects in the filtered data.
- May not perform well in complex clutter environments or with non-uniform clutter distribution.

FUZZY LOGIC-BASED ALGORITHM

Fuzzy logic is a mathematical technique that deals with uncertainty and imprecision. In this technique, a fuzzy system is designed that considers the input signal's characteristics and the noise to estimate the probability of the cell containing a target. Some applications are present in [11] and [12].

Advantages

- Can adaptively adjust filtering parameters in real-time.
- Effective in reducing clutter and preserving target signals.
- Robust to non-stationary clutter environments.

Disadvantages

- Requires a high number of fuzzy rules for optimal performance.
- Difficult to design and optimize fuzzy rules.
- High computational complexity.

MAXIMUM LIKELIHOOD ALGORITHM

The maximum likelihood algorithm is a statistical technique used for detecting targets in the presence of clutter noise. This technique estimates the probability of the cell containing a target based on the statistical properties of the signal and noise. The advantage of this technique is its ability to handle non-Gaussian clutter, but it can be computationally intensive, as introduced in the article [13].

Advantages

- Highly effective in reducing clutter and noise.
- Can estimate clutter and target parameters simultaneously.
- Can be used with other filtering techniques to improve performance.

Disadvantages

- High computational complexity.
- Requires accurate statistical models of clutter and target signals.
- Sensitive to model assumptions and parameter estimation errors. Reference:

2.2.2. TEMPORAL FILTERING

Temporal filtering involves filtering the data in the time domain. A moving average filter can be used to remove noise from the data. Various temporal filtering algorithms have been developed, such as the Kalman filter, the adaptive moving average filter, and the weighted average filter.

KALMAN FILTER

The Kalman filter is a state estimation algorithm that uses a set of mathematical equations to estimate the state of a system based on the observations made. The filter estimates the form of a system by incorporating measurements over time and minimizing the error between the predicted state and the observed state. In the article [14], numerical results show that when the Kalman filter is executed with radar reflectivity measurements observed around a large number of automatic weather observation stations (AWOS) locations, the mean squared errors of the Kalman filter rainfall estimates are smaller than the ones obtained with empirical reflectivity (Z) - rainfall (R) relationships.

Advantages

- Can handle noisy and incomplete data
- Can estimate both state and parameters
- Can incorporate system model and measurement uncertainties Disadvantages:

Disadvantages

- Computationally expensive
- Sensitive to modeling errors
- Requires prior knowledge of system dynamics

MOVING AVERAGE FILTER

The moving average filter is a simple temporal filter that works by averaging a set of consecutive data points over a defined time interval. The filter is commonly used to suppress noise in phased array FMCW weather radar data. The moving average filter can effectively reduce noise, but it can also introduce signal delay and distortion. Thesis report [15] shows a properly designed moving average filter can be used to reduce fluctuations in digital signal processing.

Advantages

- Simple and easy to implement
- Computationally efficient
- Effective in reducing random noise

Disadvantages

- Not effective in reducing non-random noise or outliers
- Can introduce lag in the signal
- May not preserve signal features

SAVITZKY-GOLAY FILTER

The Savitzky-Golay filter is a type of digital filter that works by fitting a polynomial to a set of adjacent data points and using the polynomial to estimate the value of each point in the set. This filter can be used to reduce noise in phased array FMCW weather radar data. The Savitzky-Golay filter can effectively reduce noise, but it can also introduce signal distortion and phase shift. Paper [16] describes a new filter developed for reducing speckle noise in SAR images.

Advantages

- Can handle noisy and unevenly sampled data
- Preserves signal features such as peaks and valleys
- Can remove random and non-random noise
- Can differentiate the signal

Disadvantages

- May introduce artifacts or distortions in the signal
- May require tuning of filter parameters,
- Not effective in reducing outliers or extreme noise

2.2.3. SPECTRAL PROCESSING

Spectral processing involves analyzing the frequency spectrum of the radar signal and applying appropriate filtering methods. Some of the commonly used techniques introduced in the article [17] include the spectral correlation coefficient (SCC) algorithm, the spectral domain averaging (SDA) algorithm, and the spectral noise floor clipping (SNFC) algorithm.

The SCC algorithm calculates the correlation coefficients between adjacent range bins and performs noise suppression by rejecting data with low correlation. The main advantage of the SCC algorithm is its ability to suppress non-stationary noise, which cannot be removed using traditional filtering methods. However, the SCC algorithm is computationally expensive and may cause signal loss in regions with low correlation.

The SDA algorithm calculates the average of the power spectra over a range of adjacent range bins to reduce the noise floor. The SDA algorithm effectively reduces the noise floor and enhances the signal-to-noise ratio (SNR), especially for weak signals. However, the SDA algorithm may cause blurring of the radar image and distortion of the signal waveform.

The SNFC algorithm estimates the noise floor in the spectral domain and removes the noise below a certain threshold. The SNFC algorithm effectively eliminates noise and preserves the signal waveform. However, the SNFC algorithm may remove weak signals below the noise floor, and its performance is highly dependent on the accuracy of the noise floor estimation.

2.2.4. NOISE CLIPPING

Noise clipping involves removing data that is above or below a certain threshold. Various noise-clipping algorithms have been developed. In addition to CFAR, there are the amplitude thresholding algorithm and the adaptive thresholding algorithm.

AMPLITUDE THRESHOLDING ALGORITHM

Amplitude thresholding algorithms apply a fixed threshold to the received signal, and any values above this threshold are retained, while any values below are discarded as noise. This method is simple to implement and computationally efficient, but it can result in the loss of weak signals, especially in areas with high noise levels. The advantages of amplitude thresholding algorithms include their simplicity and computational efficiency. However, they can result in the loss of weak signals.

ADAPTIVE THRESHOLDING ALGORITHM

On the other hand, adaptive thresholding algorithms dynamically adjust the threshold value based on the local statistics of the received signal. This allows for better retention

of weak signals while still removing noise, even in areas with high noise levels. However, these algorithms can be computationally expensive and may require much processing power. Adaptive thresholding algorithms, while more computationally expensive, can better retain weak signals and adapt to changing noise levels.

2.2.5. DENOISING ALGORITHMS BASED ON WAVELET TRANSFORM

Wavelet analysis is a powerful tool for analyzing signals with both temporal and spectral content. It involves the convolution of a signal with a wavelet, a mathematical function well-localized in both the time and frequency domains.

WAVELET TRANSFORM

In the book [18], the fundamentals of wavelet have been explained thoroughly. Similar to Fourier transform, the wavelet transform of the signal $f(t)$ can be formulated as:

$$F(\tau, s) = \frac{1}{\sqrt{|s|}} \int_{-\infty}^{+\infty} f(t) \phi^* \left(\frac{t-\tau}{s} \right) dt \quad (2.1)$$

The width of the wavelet $\phi(x)$ and its central frequency can be adjusted by changing the scale parameter s as it is moved across the signal. This results in a stretch or compression of the wavelet, corresponding to a frequency change. Larger values of s correspond to lower wavelet frequencies, resulting in an expanded wavelet better at resolving low-frequency signal components with poor time resolution. In contrast, smaller values s correspond to higher frequencies, resulting in a shrunken wavelet, better at resolving high-frequency signal components with good time resolution. The parameter τ represents the translation of the wavelet across the signal. To perform wavelet analysis, various windows are used, which are the dilated or compressed and shifted versions of the mother wavelet $\phi(t)$. The choice of mother wavelet and the scale and translation parameters used in the analysis can significantly impact the results obtained.

Calculating wavelet coefficients at every possible scale produces a lot of data. If s and τ are discrete samples, the wavelet transform won't generate massive amounts of data. If s and τ are based on powers of two (dyadic), then analysis becomes much more efficient and accurate.

$$D[a, b] = \frac{1}{\sqrt{b}} \sum_{m=0}^{p-1} f[t_m] \phi \left[\frac{t_m - a}{b} \right]$$

where $a = \tau, b = s$, and $a = k2^{-j}, b = 2^{-j}$ with j as the scale index and k as the wavelet transformed signal index. In Fig. 2.1, the block diagrams of fast wavelet transform and inverse fast wavelet inverse transform are given.

In this figure, $f[t_m]$ is the input signal, A_j and D_j are the Approximation and Detail components, respectively, at j^{th} decomposition level obtained through recursive low pass filtering (for Approximation component) and high pass filtering (for Detail component), and $\downarrow 2$ and $\uparrow 2$ are down-sampling and up-sampling, respectively, by a factor of 2. The process of FWT and IFWT leads to Discrete Wavelet Transform (FWT) and Inverse Discrete Wavelet Transform (IFWT), and hence they are used interchangeable Eq. (2.2)

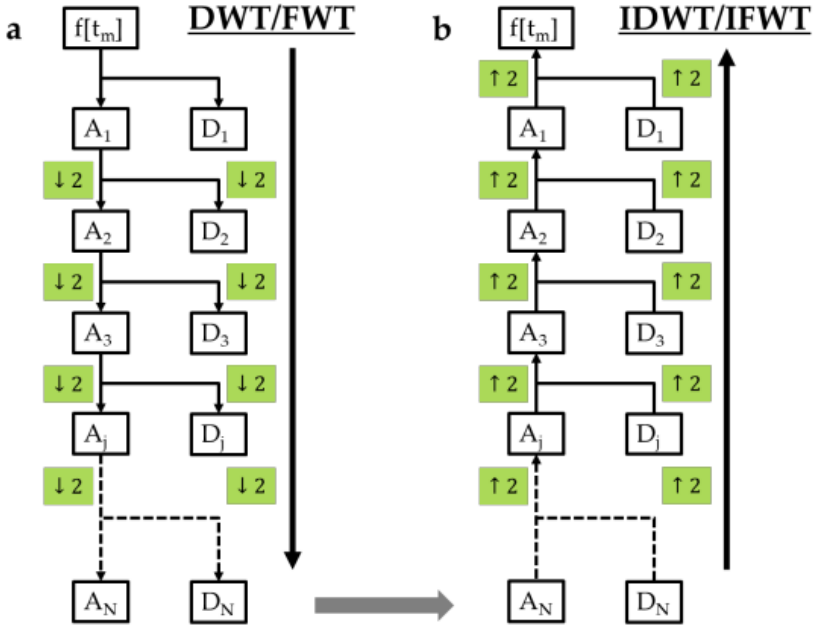


Figure 2.1: Block Diagrams of Fast Wavelet Transform and Inverse Fast Wavelet Transform

and Eq. (2.3) to describe the low pass and high pass filtering process.

$$A_{j+1}[k] = \sum_{n=0}^{L-1} l[n] A_j[2k + n] \tag{2.2}$$

$$D_{j+1}[k] = \sum_{n=0}^{L-1} h[n] A_j[2k + n] \tag{2.3}$$

where $l[n]$ and $h[n]$ are low and high pass signal decomposition filters, respectively. And L is the length of both the filters (and the scaling and wavelet functions). The filter values are the coefficient values of the scaling and wavelet functions.

TYPICAL WAVELETS

Orthonormal, semi-orthogonal, and biorthogonal wavelets are different types of wavelet bases that can be used in wavelet analysis.

Orthonormal wavelets form a complete and orthonormal basis for the signal space, meaning that any signal can be decomposed into a linear combination of orthonormal wavelet basis functions without losing any information.

Semiorthogonal wavelets form a complete basis for the signal space but are not necessarily orthogonal. This means that some information can be lost during the wavelet transform.

Biorthogonal wavelets use two sets of basis functions, one for the analysis (decomposition) and one for the synthesis (reconstruction) stages of the wavelet transform.

are not orthogonal but satisfy a set of bi-orthogonality conditions that allow for accurate reconstruction of the original signal.

Before selecting a wavelet for a specific signal, it is crucial to analyze the characteristics of the signal itself. Some essential features to consider include the signal's frequency content, its temporal behavior, and the presence of any noise or artifacts.

The frequency content of the signal can inform the choice of wavelet, as different wavelets have different frequency responses. For example, a wavelet with good high-frequency resolution may be more suitable if the signal has significant high-frequency components. The temporal behavior of the signal can also inform the choice of wavelet, as different wavelets have different time-frequency trade-offs. If the signal contains rapid changes, a wavelet with good time resolution may be preferred, while for slowly varying signals, a wavelet with better frequency resolution may be more appropriate. Finally, the presence of noise or artifacts in the signal can also impact the choice of wavelet. Wavelets with good denoising capabilities may be preferred for signals with significant noise. In contrast, wavelets that are robust to certain types of artifacts may be selected for signals with known sources of interference.

In general, wavelets with good time-frequency localization and low reconstruction error are preferred for processing noisy radar signals. Since it is difficult to get the best wavelet for all types of signals and noise. Therefore, an empirical analysis is needed to determine which wavelet is suitable for processing noisy weather radar signals with high phase noise at certain azimuth angles.

WAVELET DENOISING ALGORITHMS

Wavelet denoising algorithms are a class of techniques that leverage wavelet transforms to reduce noise in radar signals. These methods are based on multi-resolution analysis, which involves breaking the signal into different frequency bands. In wavelet denoising, the signal is decomposed into varying levels of detail using wavelet transform. The high-frequency coefficients, which represent noise in the signal, are then thresholded and eliminated, while the remaining coefficients are used to reconstruct a denoised signal. One advantage of wavelet denoising is its ability to reduce noise while preserving signal features effectively. This technique has been shown to outperform other methods in signal-to-noise ratio (SNR) improvement and preservation of signal features. However, the choice of wavelet basis function and thresholding method can significantly affect the denoising performance. Various wavelet denoising algorithms have been developed, such as the thresholding-based algorithm, the wavelet packet denoising algorithm, and the wavelet domain Wiener filtering algorithm.

2.2.6. SINGULAR VALUE DECOMPOSITION (SVD)

SVD is a matrix factorization technique that decomposes a matrix into three components: a left singular matrix, a diagonal matrix of singular values, and a right singular matrix. The diagonal matrix of singular values contains information about the relative importance of each singular vector in the decomposition. The article [19] shows that SVD and proper orthogonal decomposition can decompose velocity field data into spatiotemporal modes. It provides a method to estimate the noise level in a noise dataset and the root-mean-square error (RMSE) of the SVD modes, hence filtering the noise us-

ing only the SVD modes that have low enough RMSE.

One advantage of using SVD for noise suppression is that it can effectively separate the signal and noise components based on their singular values. Generally, the signal component has larger distinct values than the noise component, so the noise can be suppressed by setting a threshold on the distinct values and discarding the corresponding singular vectors. Another advantage of using SVD for noise suppression is that it can be applied to both spatial and temporal domains.

However, one limitation of using SVD for noise suppression in phased array FMCW weather radar is that it requires knowledge of the noise statistics, which may not be available in some cases. Moreover, the effectiveness of SVD for noise suppression may be limited by the SNR and the complexity of the noise structure.

2.3. DOPPLER DE-ALIASING TECHNIQUES

The majority of Doppler velocity dealiasing techniques rely on spatial continuity principles, spanning from one-dimensional solutions [20], to more complex two-dimensional approaches [21], and even further to three-dimensional methodologies [22], and occasionally extending into four dimensions by incorporating temporal continuity [23]. Despite these advancements, a central challenge persists: areas devoid of substantial returns, which are often censored or omitted from displays, disrupt the velocity field's continuity. Furthermore, robust wind shears associated with severe weather conditions compound the intricacies of correcting velocity aliasing. In cases where preceding neighbors are absent, alternative strategies have emerged, including leveraging upper-air soundings as references [24], or relying on velocity-azimuth display winds [25]. In addition, there is one advanced dealiasing tool, named "UNRAVEL" introduced in the article [26].

While these methods do provide a logically feasible path to Doppler de-aliasing, it is worth noting that simulation validation specifically for the FMCW radar environment is lacking so far.

2.4. CONCLUSION

This chapter gives the state of the art of the typical weather phased array FMCW radar data processing flowchart and covers the related developed algorithms which aim to enhance the data quality, noise suppression, and target detection. The possible solutions consist of adaptive and standard algorithms. They are validated to work for target detection and mitigating the interference existing in the radar data. The strengths and weaknesses of these algorithms are evaluated. It came to the conclusion that to address this research project problem, a combination of various algorithms, such as denoising using wavelet techniques, and target mapping using CFAR detector, morphological operations, or thresholding, can be the potential approach, resulting in a target mapping processing pipeline tailed for Robin Radar's 3DMax phased array radar.

Furthermore, within this chapter, a summary of the newly developed Doppler de-aliasing techniques is provided. This summary not only highlights the inherent potential of checking continuity but also underscores the need for further validation of the UNRAVEL approach.

3

APPLICATION OF CIRCULAR STATISTICS ON THE DOPPLER SPECTRUM

This chapter focuses on the application of circular statistics for Doppler spectrum analysis. It begins by discussing the characteristics of weather-like spectrum and signals, which exhibit circular properties due to the cyclical nature caused by Doppler ambiguity. It introduces the concept of Doppler spectral moments, which provide valuable information about the velocity distribution of radar targets. To analyze these moments, it explains the principles of circular statistics specifically designed to handle circular data. The different methods for estimating the mean Doppler and spectrum width are evaluated. Simulation results and validation are provided to demonstrate the effectiveness of the circular moments approach. Furthermore, the application of circular moments on real-world data is shown, highlighting their utility in analyzing actual radar measurements. In addition, this chapter proposes the circular variance-based target mapping technique. It introduces circular variance as a measure of the dispersion of radar echoes around the mean Doppler frequency, thereby measuring the concentration of targets within one radar range gate. The effectiveness of circular variance as a criterion to filter out noise is proved. The sensitivity of circular variance to DPP, which is the difference between the peak of signal and peak of noise is discussed. According to that, the threshold value of circular variance is elected to design the real-world target binary mask.

3.1. WEATHER-LIKE SPECTRA AND SIGNALS

The weather echo and receiver noise have very similar statistical properties, between which the difference is that the signal power is usually larger and its spectrum is not broadband [27]. The in-phase, I , and the quadrature-phase, Q , components at one range

gate for the i_{th} sample can be written as:

$$\begin{aligned} I(i) &= s(i) \cos \phi(i) + n(i) \cos \psi(i) \\ Q(i) &= s(i) \sin \phi(i) + n(i) \sin \psi(i) \end{aligned} \quad (3.1)$$

In Eq. (3.1), $s(i)$ is the Rayleigh distributed signal envelope, and $\phi(i)$ is a uniformly distributed phase. Equation (3.1) can be expressed as regards a discrete Fourier series summed over the spectral record of length T_{prf}^{-1} :

$$I(i) + Q(i) = \frac{1}{n} \sum_{k=1}^n P_k^{\frac{1}{2}} \exp(j\theta_k) \exp\left(-j\frac{2\pi}{n} ki\right) \quad (3.2)$$

where P_k is the exponentially distributed instantaneous power of signal plus noise, in which the signal is frequency independent, and noise is white. θ_k is a uniformly distributed phase. P_k and θ_k are statistically independent. S_k is the frequency-dependent signal power density. Since the noise is white, the noise per discrete frequency can be expressed as $N = \frac{\text{total noise power}}{\text{frequency band}}$. Hence, the probability density of P_k is:

$$P(P_k) = \frac{1}{S_k + N} \exp\left[-\frac{P_k}{S_k + N}\right] \quad (3.3)$$

The average signal-to-noise ratio is then:

$$\frac{\text{signal}}{\text{noise}} = \frac{\sum_{k=1}^n S_k}{nN} \quad (3.4)$$

3.2. DOPPLER SPECTRAL MOMENTS

For atmospheric radars, at each range bin, the Doppler power spectrum is assumed to be in Gaussian shape. The extracting desired information or measuring some attributes of the signal may often relate to the fundamental base parameters:

Radar reflectivity factor	Z	dBZ
Mean Doppler velocity	V	ms ⁻¹
Spectral width	W	ms ⁻¹

Let the Doppler power spectrum of the received signal be denoted by $A(v)$, and then the three spectrum moments can be computed as:

$$M_0 = \int |A(v)|^2 dv \quad (3.5)$$

$$M_1 = \frac{1}{M_0} \int v |A(v)|^2 dv \quad (3.6)$$

$$M_2 = \sqrt{\frac{1}{M_0} \int (v - M_1)^2 |A(v)|^2 dv} \quad (3.7)$$

The zeroth moment is the area under $A(v)$ and represents the total signal, clutter, and noise power from the radar volume at a specific range from radar. The first moment,

mean Doppler velocity, is the power spectrum's mean. In the frequency domain representation, the Doppler-shifted frequencies caused by the motion of precipitation particles are observed as peaks or spikes along the frequency axis. Each peak corresponds to a specific Doppler velocity, indicating the radial velocity of the particles relative to the radar. The white noise biases the velocity towards zero. For a pure noise spectrum, the mean Doppler velocity is identically zero. The second moment represents the velocity spectrum width and is equal to the square root of the velocity variance within the resolution volume. Wind shear, turbulence, and the variability of particles' falling velocities with their size contribute to this spectral moment [28].

3.3. CIRCULAR STATISTICS

Doppler ambiguity occurs when a target's Doppler shift exceeds the pulse repetition frequency (PRF) of the radar system. PRF represents the transmission rate of radar pulses. When the Doppler shift exceeds this threshold, this wrapping of the spectrum leads to overlapping and uncertainty, making it difficult to determine the true frequency components. The target radial velocity that can be measured unambiguously must lie within well-defined limits, defined as

$$|v_{\text{unamb}}| \leq \frac{\lambda \cdot \text{PRT}}{4} \quad (3.8)$$

As discussed above, the standard Doppler moments are derived as equations 3.5, 3.6, and 3.7 assuming the Doppler velocity is defined in a 1-D linear space from $-\infty$ to $+\infty$. Due to the Doppler ambiguity, the measured Doppler spectrum, which is the representative of the precipitation particles' motion, wraps around the circle whose interval is $[-v_{\text{unamb}}, v_{\text{unamb}}]$. As a result, the standard estimation of the mean Doppler velocity, which characterizes the environmental wind speed, can shift the linear mean closer to zero and incorrect spectrum width. For example, if the spectrum will have two strong modes at $[-v_{\text{unamb}} + \Delta u]$ and $[+v_{\text{unamb}} - \Delta u]$, the mean velocity, which is defined using linear space Eq. (3.6), will be equal to 0 instead of a more realistic value of $\pm v_{\text{unamb}}$.

To overcome the challenges posed by Doppler's ambiguity, this project turns to the field of circular statistics. Circular statistics, also known as directional statistics, deals with data measured in cyclic or circular units. This makes it particularly suitable for analyzing wrapped data, such as the wrapped Doppler spectrum. By leveraging the principles and tools of circular statistics, we can effectively estimate the Doppler spectrum moments while accounting for the ambiguity caused by wrapping.

In the book [29], Mardia gave an overview of circular statistics. Given unit vectors $\mathbf{x}_1, \dots, \mathbf{x}_n$ with corresponding angles $\theta_1, \dots, \theta_n$, the mean direction $\bar{\theta}$ is the direction of the center of mass $\bar{\mathbf{x}}$ of $\mathbf{x}_1, \dots, \mathbf{x}_n$. Denote the x_j in the Cartesian coordinates, the center of mass in the Cartesian coordinates are (\bar{C}, \bar{S}) , where

$$\bar{C} = \frac{1}{n} \sum_{j=1}^n \cos \theta_j, \quad \bar{S} = \frac{1}{n} \sum_{j=1}^n \sin \theta_j \quad (3.9)$$

The mean resultant length \bar{R} is given by

$$\bar{R} = (\bar{C}^2 + \bar{S}^2)^{1/2} \quad (3.10)$$

When $\bar{R} > 0$, the mean direction is given by

$$\begin{cases} \tan^{-1}(\bar{S}/\bar{C}), & \text{if } \bar{C} \geq 0 \\ \tan^{-1}(\bar{S}/\bar{C}) + \pi, & \text{if } \bar{C} < 0 \end{cases} \quad (3.11)$$

To measure the dispersion, the circular variance and circular standard deviation are given by

$$V = 1 - \bar{R} \quad (3.12)$$

$$\nu = \{-2\log(1 - V)\}^{1/2} = \{-2\log\bar{R}\}^{1/2} \quad (3.13)$$

For small variances, Batschelet[30] approximates the circular variance and circular standard deviation to

$$V = 2(1 - \bar{R}) \quad (3.14)$$

$$\nu = \{2(1 - \bar{R})\}^{1/2} \quad (3.15)$$

3.4. CIRCULAR ESTIMATION OF MEAN DOPPLER AND SPECTRUM WIDTH

Supposed that Doppler spectrum samples d_1, \dots, d_n for a resolution volume, and corresponding velocity samples v_1, \dots, v_n , the angle samples a_1, \dots, a_n can be derived from

$$a_i = \frac{\pi}{v_{\text{unamb}}} \cdot v_i \quad (3.16)$$

The center of mass can be represented as (c,s) in the Cartesian coordinates where

$$c = \frac{\sum_{j=1}^n \cos a_j}{\sum_{j=1}^n d_j}, \quad s = \frac{\sum_{j=1}^n \sin a_j}{\sum_{j=1}^n d_j} \quad (3.17)$$

Then the resultant length is

$$r = (c^2 + s^2)^{1/2} \quad (3.18)$$

The mean of the Doppler spectrum refers to the central tendency or the dominant velocity components of the scatterers or objects within the resolution cell. The circular mean of the Doppler spectrum can be estimated as

$$M_{1\text{circ}} = \frac{v_{\text{unamb}}}{\pi} \cdot \begin{cases} \tan^{-1}(\bar{s}/\bar{c}), & \text{if } \bar{C} \geq 0 \\ \tan^{-1}(\bar{s}/\bar{c}) + \pi, & \text{if } \bar{C} < 0 \end{cases} \quad (3.19)$$

The spectrum width measures the velocity dispersion. With Mardia's circular theory [31], the circular spectrum width of the Doppler spectrum is

$$M_{2\text{circMardia}} = \frac{v_{\text{unamb}}}{\pi} \cdot \{-2\log r\}^{1/2} \quad (3.20)$$

And using Batschelet's theory [30], the circular spectrum width of the Doppler spectrum for small variance is

$$M_{2\text{circBatschelet}} = \frac{v_{\text{unamb}}}{\pi} \cdot \{2(1 - r)\}^{1/2} \quad (3.21)$$

3.5. SIMULATION RESULTS AND VALIDATION FOR MEAN DOPPLER AND SPECTRUM WIDTH ESTIMATION

In this project, MATLAB software is used to develop the algorithms and perform the necessary calculations to validate the proposed methods. The models of unfolded and folded Doppler spectrum are shown in the figures 3.1, with $v_{unamb} = 7.3938 [m/s]$. This value of unambiguous Doppler is obtained from real-world data collected by the Robin Radar's 3D-Max FMCW radar.

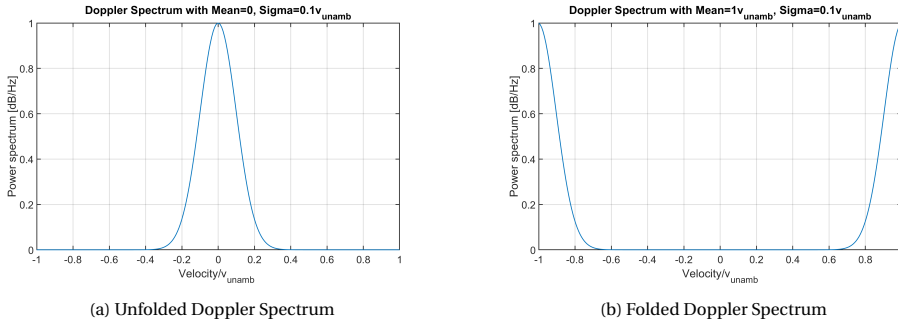


Figure 3.1: Doppler spectrum With and Without the occurrence of Folding

3.5.1. MEAN DOPPLER ESTIMATION

For the simulation evaluation, this work implemented three methods of calculating the mean Doppler, respectively: (1). Linear estimation; (2). Circular estimation; (3) Shift-back estimation. Setting the spectrum width as $0.1 \times v_{unamb} \approx 0.74 [m/s]$, the mean estimation results of three methods are plotted in Fig. 3.2.

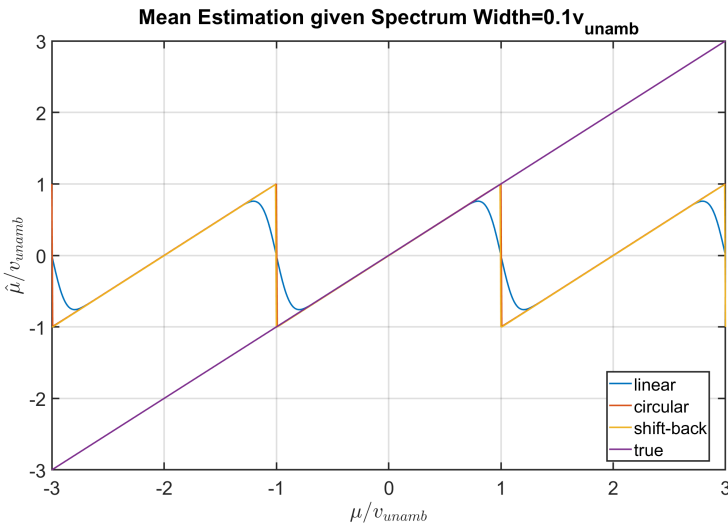


Figure 3.2: Mean Estimation

The first two are explained in the texts above. The shift-back method is commonly used in radar and remote sensing applications to estimate the parameters of the Doppler spectrum. In the frequency domain representation, the Doppler-shifted frequencies caused by the motion of precipitation particles are observed as peaks or spikes along the frequency axis. Each peak corresponds to a specific Doppler velocity, indicating the radial velocity of the particles relative to the radar. The shift-back method leverages the identification and alignment of the peak in the Doppler spectra to accurately estimate the mean Doppler and spectrum width.

3.5.2. SPECTRUM WIDTH ESTIMATION

For the Doppler spectrum width, there are four methods in need to validate in simulation evaluation: (1). Linear estimation; (2). Circular estimation using Batschelet's equation; (3). Circular estimation using Mardia's equation; (4). Shift-back method. The different thing with the mean Doppler estimation is that there are two available equations. One formula 3.20 is proposed by Mardia and the other one 3.21 is put forward by Batschelet with a different approximation method. In MATLAB, after Doppler processing, the shift-back method to calculate the spectrum width is implemented following the steps:

1. Find the location of the dominant velocity component;
2. Shift the spectrum to align the dominant velocity component to zero;
3. Estimate the spectrum width using the linear method.

Setting the mean Doppler as $\mu = 1.5 \times v_{unamb} \approx 11.09$ [m/s], the mean estimation results of four methods are plotted in Fig. 3.3.

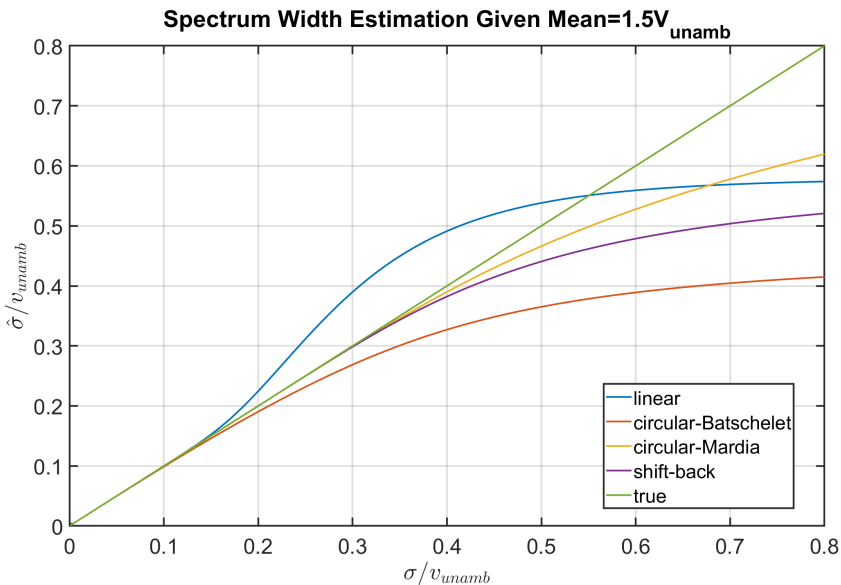


Figure 3.3: Spectrum Width Estimation with Different Methods Given Mean = 1.5 × Unambiguous Doppler

From Fig. 3.3, there are some conclusions can be drawn:

1. When the spectrum width is located at the interval (0, 0.15] times the unambiguous Doppler, all of the four methods give the correct estimation.
2. When the spectrum width increases to the interval (0.15, 0.8) times the unambiguous Doppler, the circular method using Mardia's equation gives the least error estimation.
3. In the case where the actual spectrum width lies in the interval (0.15, 55) times the unambiguous Doppler, the linear method gives the spectrum width estimation higher than the true value. While in the interval (0.55, 0.8) times the unambiguous Doppler, the linear method estimate is lower than the true value.

From the initial investigations into the statistical characteristics of spectral width provided by [32], in most cases without extreme weather, the spectrum width should lie below 3 [m/s], which is around $0.4 \times \nu_{unamb}$. Take a focus on the interval where $\sigma/\nu_{unamb} \in (0, 0.4)$, the circular method using Mardia's equation has the most accurate estimation.

In addition, it is necessary to analyze each method's spectral width estimation performance under different mean Doppler since the methods may have different underlying assumptions and algorithms, which can impact their performance under different mean values. The simulation results are shown in figures 3.4, 3.5, 3.6, and 3.7.

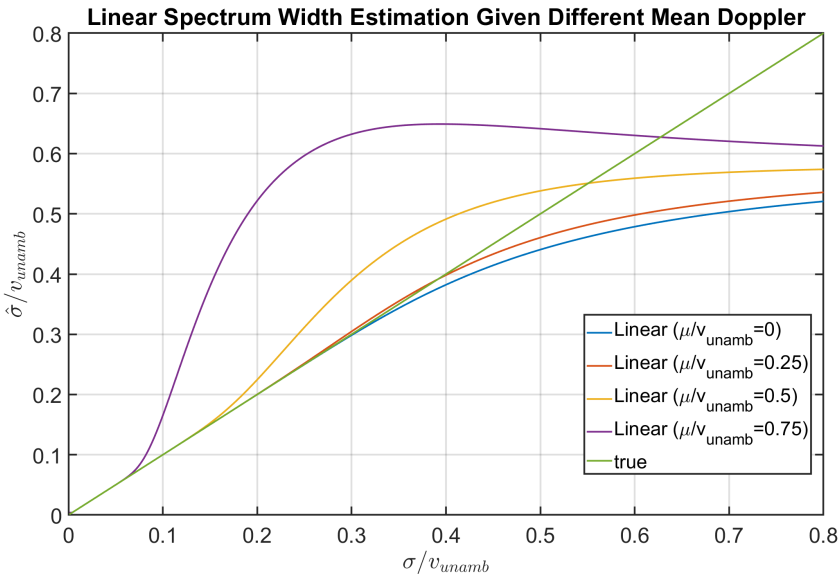


Figure 3.4: Spectrum Width Estimation Given Different Mean Doppler Using Linear Method

Circular Spectrum Width Batschelet Estimation Given Different Mean Doppler

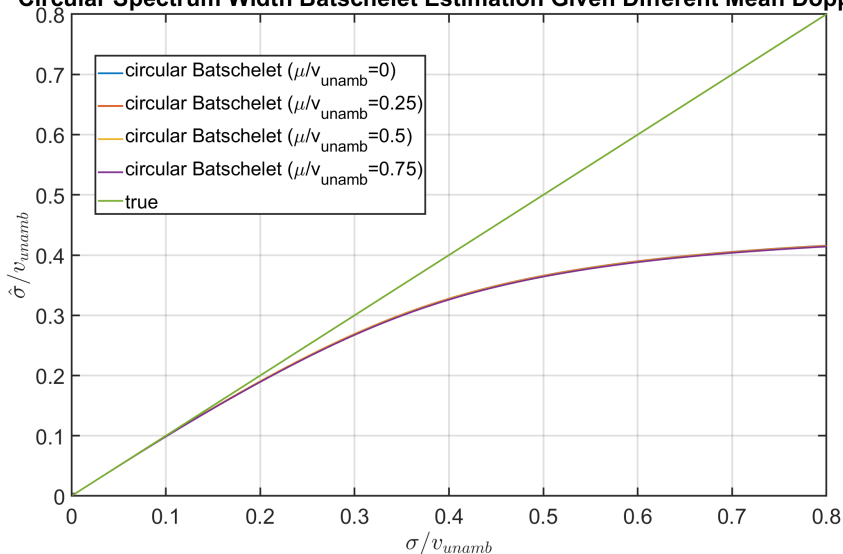


Figure 3.5: Spectrum Estimation Given Different Mean Doppler Using Circular Method with Batschelet's Equation

Circular Spectrum Width Mardia Estimation Given Different Mean Doppler

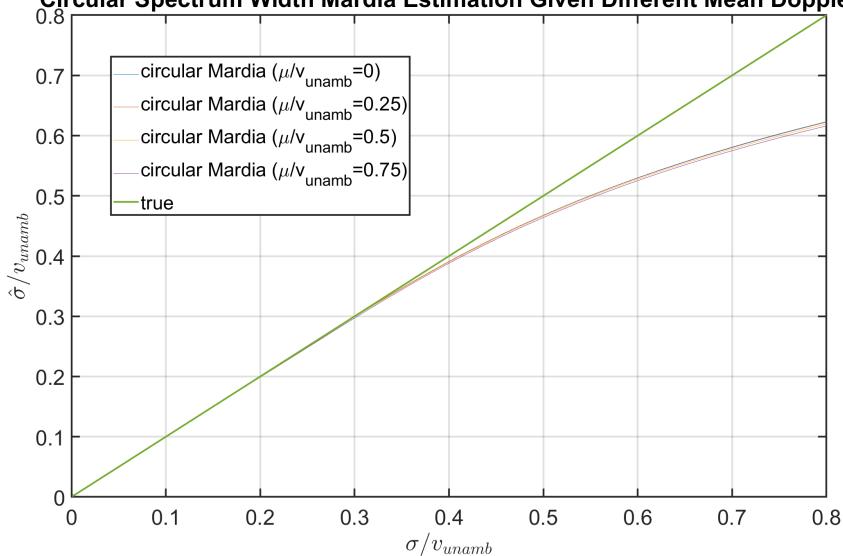


Figure 3.6: Spectrum Estimation Given Different Mean Doppler Using Circular Method with Mardia's Equation

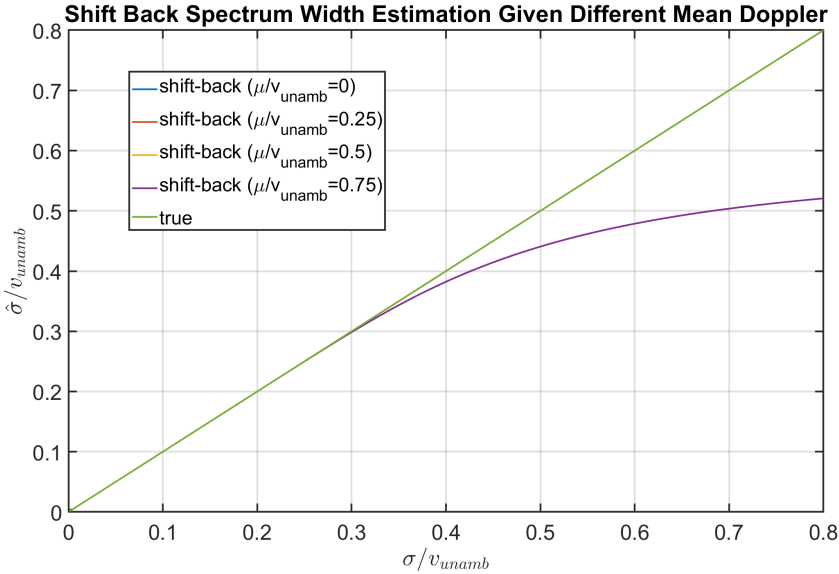


Figure 3.7: Spectrum Width Estimation Given Different Mean Doppler Using Shift-back Method

There are some conclusions can be drawn from the figures above:

1. Examining the results, it becomes evident that the linear estimation of spectrum width reacts particularly sensitively to shifts in the mean Doppler's placement, shown in Fig. 3.4. When the mean Doppler approaches closer to 0, a noticeable enhancement in the precision of the spectrum width estimation becomes apparent.
2. The remaining three methods: two circular estimations using different equations and the shift-back method, demonstrate remarkable robustness in the face of mean Doppler variations.
3. The circular estimation utilizing Mardia's equation stands out for its consistent stability across conditions with various mean Doppler values while also exhibiting the least significant margin of error.

Taking all these factors into consideration, it came to the conclusion that the circular estimation with Mardia's equation has the best performance both in the mean Doppler and the spectrum width estimation.

3.6. CIRCULAR SPECTRUM MOMENTS OF REAL-WORLD DATA

After performing discrete Fourier transformation processing on samples within a single range bin, the Doppler spectrum of each resolution volume can be acquired from the gathered radar data. One example of the Range-Doppler map of the received signal at a specific azimuth and elevation is shown in Fig. 3.8. In Fig. 3.8, the black dots represent

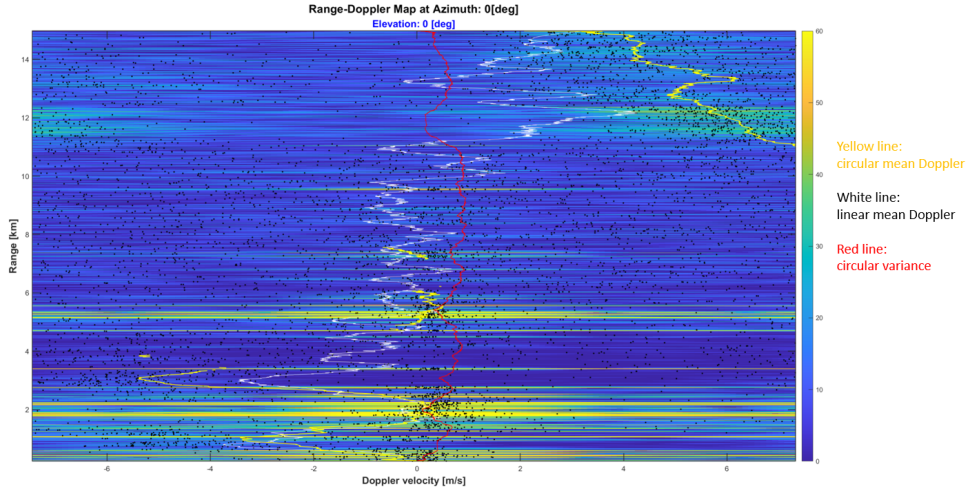
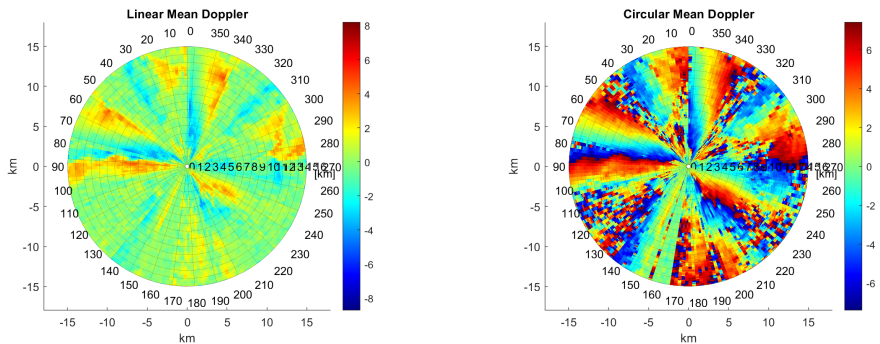


Figure 3.8: Range-Doppler map of the received signal at a specific azimuth and elevation

the power spectrum values. The concentrated Doppler region has high values, which is meant by the yellow region from the colorbar. It can be observed that the yellow line (circular estimation of the mean Doppler) is more following the dominant Doppler than the white line (linear estimation of the mean Doppler).

Fig. 3.9 and Fig. 3.10 illustrate the conventional linear and the proposed circular determination of Mean Doppler and Spectrum width. Notably, compared with the linear method, the circular moments reveal more pronounced Discontinuities resulting from Doppler ambiguity. The employment of the circular method enhances the precision of mean Doppler and spectrum width estimation.

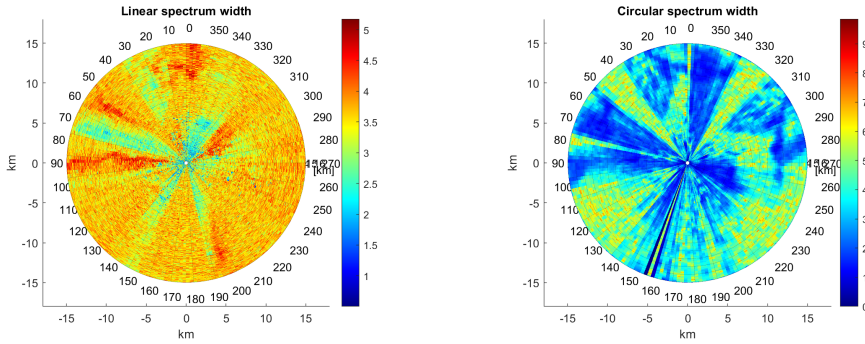
Besides that, it's important to highlight that Fig. 3.9b distinctly indicates whether the



(a) Mean Doppler of Real-world Data Using Conventional Linear Method

(b) Mean Doppler of Real-world Data Using Proposed Circular Method

Figure 3.9: Mean Doppler of Real-world Data Using Conventional Linear Method and Proposed Circular Method



(a) Spectrum Width of Real-world Data Using Conventional Linear Method

(b) Spectrum Width of Real-world Data Using Proposed Circular Method

Figure 3.10: Spectrum Width of Real-world Data Using Conventional Linear Method and Proposed Circular Method

pixel represents noise or effective Doppler velocity, given the intricate pattern of data. The noise area identified by the mean Doppler aligns with the portion of the spectral width plane where oscillations hover around 0. This alignment implies that spectrum moments derived from circular statistics can potentially facilitate recognition in distinguishing between objects and noise.

3.7. TARGET MAPPING BASED ON CIRCULAR VARIANCE

This section presents the proposed circular variance-based target mapping technique.

3.7.1. CIRCULAR VARIANCE

As previously mentioned, circular statistics encompasses a variety of statistical measures and techniques specifically designed to handle circular data. Besides circular mean and circular spectrum width, circular variance can be used as a factor to filter out noisy data. The circular variance quantifies the spread or dispersion of the data around the circular mean. It measures the variability of the angles or directions in a circular dataset. Using Eq. (3.12), the circular variance of the real-world radar measurements, is shown in Fig. 3.11.

From Fig. 3.11, it can be observed that there are distinct regions with high circular variance, which are shown in red. Within the specified range gates, the circular variance is denoted in blue, indicating that its value remains below 0.3.

The circular variance is a metric that spans a range from 0 to 1, encapsulating the degree of variation within angular measurements. A circular variance value of 0 indicates a high degree of consistency and alignment among measurements. Data points cluster tightly around a central angle, forming a compact grouping. This scenario manifests as a sharply peaked circular distribution, reflecting a coherent target signal.

Conversely, a circular variance of 1 indicates an absence of a preferred or dominant direction. Data points are uniformly scattered across the entire circular range, resulting in an even distribution. In practical terms, a circular variance of 1 signifies the presence

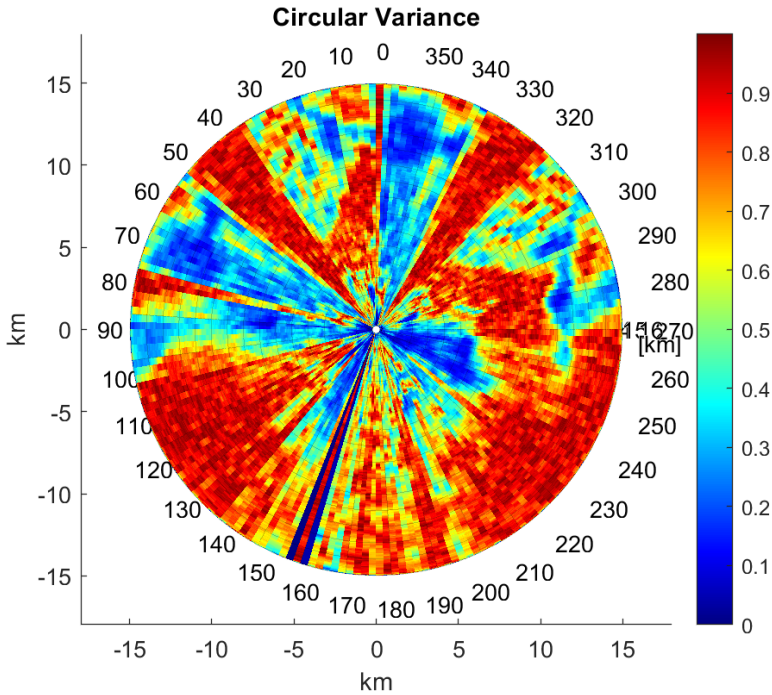


Figure 3.11: Circular variance Derived from the Real-world Data

of random noise within the measurements.

Within a single range gate, a higher circular variance value implies a greater likelihood of noise-like behavior. Consequently, the circular variance can serve as an indicator of noise presence. By setting a threshold for circular variance, it becomes possible to filter out data points that are potentially noisy or unreliable. The selection of an appropriate threshold is a topic explored in the subsequent sections.

3.7.2. SENSITIVITY OF CIRCULAR VARIANCE ON DPP

The determination of the specific circular variance threshold value hinges on the intrinsic characteristics of the data and the requisite noise elimination level. To ascertain this threshold value, a detailed analysis is conducted, focusing on the sensitivity of circular variance about the Difference between the Peak of the signal power spectrum and the Peak of the noise power spectrum (referred to as DPP)—measured in decibels. In this context, DPP quantifies the variation between the highest points of the signal and noise power spectra. Within each range gate, the power spectrum of thermal noise is presumed to be uniformly distributed, while the target's power spectrum conforms to a Gaussian distribution. To explore the interplay between circular variance and DPP, the Doppler spectrum within a specific range gate is conceptualized, as depicted in Figure 3.12.

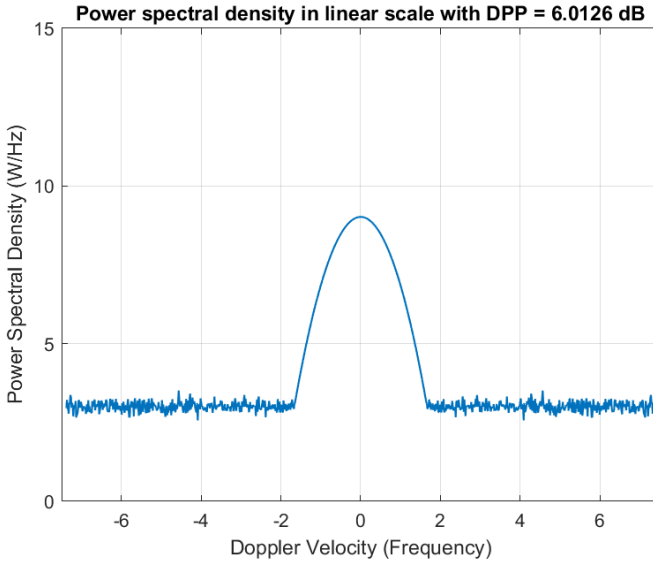


Figure 3.12: Modeling the Doppler Spectrum within One Range Gate

By varying the value of DPP, a series of circular variance estimation plots corresponding to different DPP scenarios can be generated. As depicted in Figure 3.13, these plots take into account distinct standard deviations of the signal power spectrum.

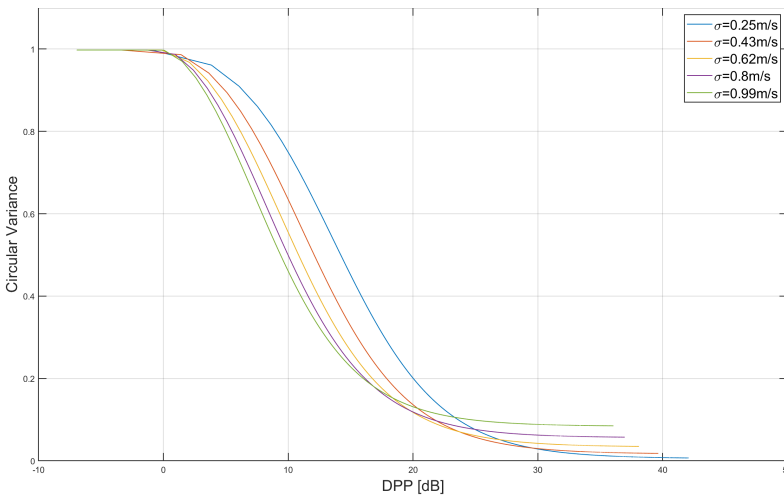


Figure 3.13: Sensitivity of Circular Variance on DPP Under Different Signal Standard Deviations

From the illustration, a clear pattern emerges that as the circular variance value increases, the inherent noise in the data becomes more pronounced. This relationship

emphasizes the fact that larger circular variance values correlate with a higher level of noise within the measurements.

3.7.3. TARGET MASK FOR REAL-WORLD DATA

For real-world radar measurements provided by Robin 3DMax radar, data points with corresponding circular variance above the threshold are filtered out. From Fig. 3.13, the smaller threshold means to be more stringent and filter out more data points. Setting the threshold as 0.8 to generate the target mask and apply it in the circular mean Doppler and reflectivity planes. The results are shown in Fig. 3.14 and Fig. 3.15.

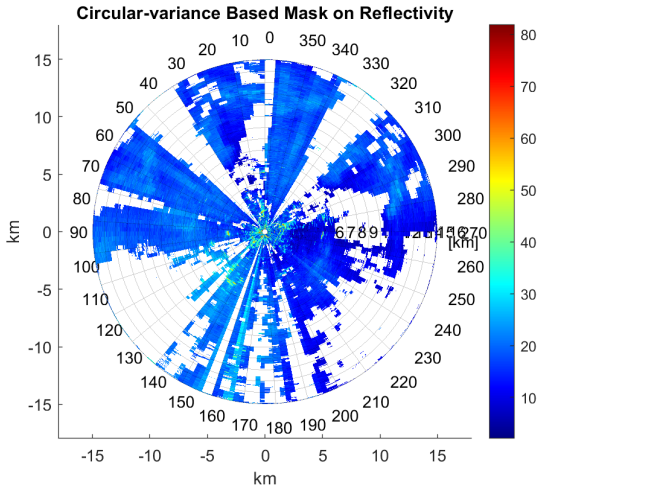


Figure 3.14: Apply Circular-variance Based Mask on Reflectivity

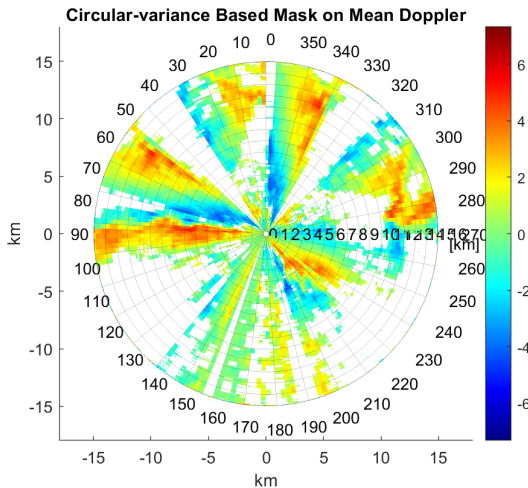


Figure 3.15: Apply Circular-variance Based Mask on Mean Doppler

3.8. CONCLUSION

In this chapter, the characteristics of weather-like spectrum and signals are analyzed, exhibiting the circular properties caused by Doppler ambiguity. The importance of the three essential Doppler spectrum moments: reflectivity, mean Doppler, and spectrum width, are explained. The conventional estimation of the Doppler spectrum moments is considered in linear statistics, strongly affected by the circular properties of the Doppler spectrum.

The concepts of circular mean, circular variance, and circular standard deviation are then introduced. The application of such circular concepts on the Radar Doppler spectrum is then analyzed. Based on the circular method, the novel estimation of mean Doppler and spectrum width are derived. This proposed technique is verified to have more accurate results and more robust performance against the other factors in the simulation compared to the conventional method. Utilizing the technique to plot the range-Doppler map of the Robin radar's received signal at a specific azimuth and elevation, it is clear that the circular method can provide the mean Doppler more following the dominant component in the spectrum. Especially, with regards to the mean Doppler estimation, the circular method using Mardia's equation is validated to be more effective than that using Batschelet's equation. The results of applying the circular method to compute the mean Doppler and spectrum width of the real-world data are displayed.

4

TARGET MAPPING BASED ON REFLECTIVITY

The ability to map targets accurately from radar measurements is of paramount importance for military, civil, and environmental purposes. This chapter presents two target mapping approaches focusing on reflectivity in radar data analysis. It begins by discussing the modeling of objects in an image using a 2D Gauss function, which provides a mathematical representation of target reflectivity. This modeling approach allows for accurate estimation and characterization of target properties based on their reflectivity patterns. A simulation model in MATLAB is developed to validate the target mapping pipelines. The first pipeline is based on morphology and contains stages such as CFAR detection of the point targets, detecting the azimuth where phase exists and making them void, wavelet denoise, applying morphological operations to map the targets, restoration of phase noise azimuths, and morphological filling gaps. The second one is classifying the radar data types based on entropy, incorporating the following stages: CFAR detection for point targets, thresholding using Renyi's Entropy for white Gaussian noise detection, and detection using normalized mean along range for phase noise. Evaluation and performance analysis is conducted to assess the effectiveness of the pipeline using simulated data. The results of applying these two pipelines to real-world radar measurements are present.

4.1. MODELING OBJECTS IN AN IMAGE WITH A 2D GAUSS FUNCTION

One of the challenges in this project is that there is no ground truth. To validate and evaluate the algorithms proposed, the algorithm can be operated on a well-defined model or simulation. This involves defining specific scenarios and evaluating the algorithm's behavior and outcomes within those scenarios. The ideal weather measurement reflectivity samples \mathbf{Z} are comprised of the echoes from targets (weather signal samples) \mathbf{S} and

noise \mathbf{N} :

$$\mathbf{Z} = \mathbf{S} + \mathbf{N} \quad (4.1)$$

To fit an elliptical contour to a two-dimensional Gaussian in an image, the signal matrix \mathbf{S} involves two random variables, \mathbf{s}_x and \mathbf{s}_y , with mean values $\bar{\mathbf{s}}_x$ and $\bar{\mathbf{s}}_y$. A particular combination of \mathbf{s}_x and \mathbf{s}_y can be represented as a column vector:

$$\mathbf{s}^T = (\mathbf{s}_x, \mathbf{s}_y) \quad (4.2)$$

where \mathbf{s}_x , \mathbf{s}_y consists of M and N samples respectively. The mean values corresponding to each variable can be written as a vector $\bar{\mathbf{s}} = (\bar{\mathbf{s}}_x, \bar{\mathbf{s}}_y)^T$. Each variable will have a variance σ_x^2 and σ_y^2 . Denote the covariance σ_{xy}^2 and σ_{yx}^2 with $\sigma_{xy}^2 = \sigma_{yx}^2$, which can be incorporated into a variance-covariance matrix:

$$\mathbf{Q} = \begin{pmatrix} \sigma_x^2 & \sigma_{xy}^2 \\ \sigma_{yx}^2 & \sigma_y^2 \end{pmatrix} \quad (4.3)$$

The Gaussian is then given by

$$\begin{aligned} f(\mathbf{s}) &= \frac{1}{\sqrt{(2\pi)^2 |\mathbf{Q}|}} \exp \left[-\frac{1}{2} (\mathbf{s} - \bar{\mathbf{s}})^T \mathbf{Q}^{-1} (\mathbf{s} - \bar{\mathbf{s}}) \right] \\ &= A \cdot \exp \left[-\frac{1}{2} (\mathbf{s}_x - \bar{\mathbf{s}}_x, \mathbf{s}_y - \bar{\mathbf{s}}_y)^T \mathbf{Q}^{-1} (\mathbf{s}_x - \bar{\mathbf{s}}_x, \mathbf{s}_y - \bar{\mathbf{s}}_y) \right] \end{aligned} \quad (4.4)$$

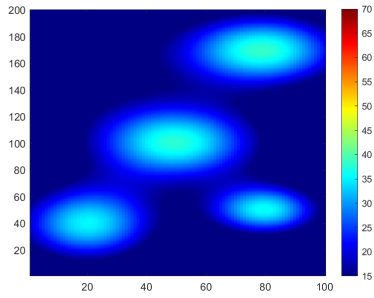
where $A = \frac{1}{2\pi\sqrt{|\mathbf{V}|}}$ is the amplitude with $|\mathbf{V}|$ the determinant of \mathbf{V} .

For the case of uncorrelated variables \mathbf{s}_x and \mathbf{s}_y , the Gaussian PDF can be represented as:

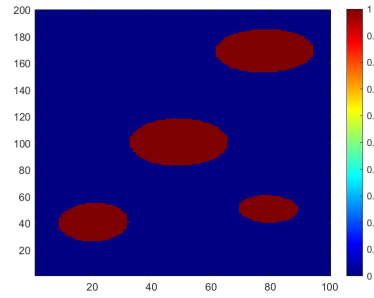
$$f(\mathbf{s}_x, \mathbf{s}_y) = A \cdot \exp \left[-\frac{1}{2} \left(\frac{(\mathbf{s}_x - \bar{\mathbf{s}}_x)^2}{\sigma_x^2} + \frac{(\mathbf{s}_y - \bar{\mathbf{s}}_y)^2}{\sigma_y^2} \right) \right] \quad (4.5)$$

4.2. SIMULATION MODEL DEVELOPMENT IN MATLAB

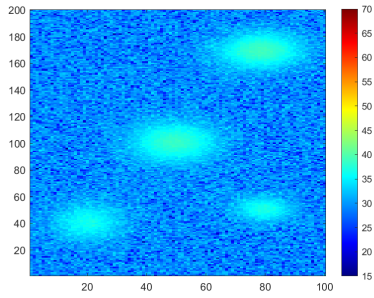
The results of 2D Gaussian models are shown in Fig. 4.1. Adding the thermal noise on Fig. 4.1a, which is normal distribution globally, 4.1b can be plotted. By observing the measurements, it can be noted that phase noise exists at some specific azimuths. As mentioned in the chapter1, inherent imperfections of real-world oscillators and various analog components, environmental factors, and strong reflection from radar near-zones can introduce phase noise into the system. To perform simulations in MATLAB, the phase noise is built under the assumption that it has a relatively smaller variance along range but a high noise level, as shown in Fig. 4.1c. In the zone close to the radar, there is strong reflectivity caused by the point targets, which could be buildings, shown in Fig. 4.1d. Applying the simplest way of target detection, fixed thresholding technique on reflectivity model, the corresponding target masks can be generated in Fig. 4.1e, 4.1f, 4.1g, and 4.1h.



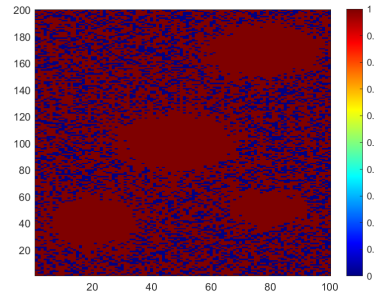
(a) Target Only



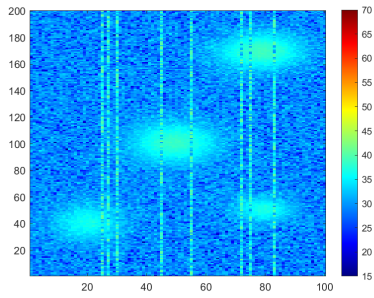
(e) Ground Truth



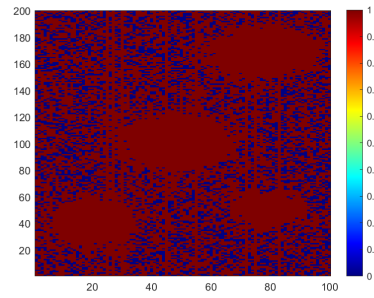
(b) Target, Thermal Noise



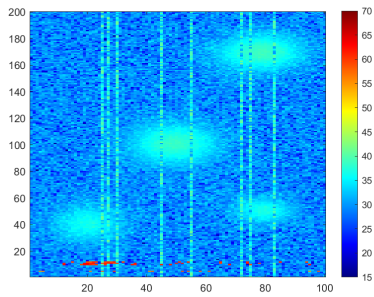
(f) Target, Thermal Noise Mask



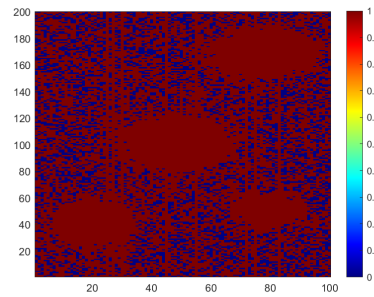
(c) Target, Thermal, Phase noise



(g) Target, Thermal, Phase Noise Mask



(d) Target, thermal, phase noise, Point Targets



(h) Target, Thermal, Phase Noise, Point Target Mask

Figure 4.1: Reflectivity Model in MATLAB

Using the standard thresholding technique, the thermal noise, phase noise, and point targets can be mistakenly classified as target signals, resulting in a higher false alarm rate. On the other hand, the noise can also cause the target signals to fall below the fixed threshold, resulting in missed detections.

4.3. MORPHOLOGY-BASED TARGET MAPPING PIPELINE

This section presents a Morphology-based target mapping pipeline that focuses on reflectivity to enhance the quality of the radar data and accurately identify targets. The pipeline consists of several key steps that aim to detect the point targets, detect the azimuth where phase exists and make them void, denoise the reflectivity data using wavelet techniques, apply morphological operations to map the targets, restore phase noise azimuths, and morphologically fill any remaining gaps. The following subsections provide a detailed explanation of each step. To validate the proposed algorithm, the model mentioned in section 4.2 is used.

4

4.3.1. POINT TARGETS DETECTION USING CFAR

The high-level values in the observations are either point targets or phase noise. These two classes can be differed by applying CA-CFAR (Cell Averaging CFAR) along ranges since the phase noise has a smaller variance along ranges than point targets do. For each azimuth, the values along ranges are divided into windows. Within each window, the CFAR detector calculates the average power of the signal across all the reference cells. This average is referred to as the "local cell average", which is obtained by using a specific number of neighboring cells (guard cells and reference cells) around the cell to test (CUT). The CFAR detector compares the local cell average with the CUT. If the CUT is above the threshold, which can be controlled by the multiplication of a threshold factor with the local cell average, the CUT is determined to be "target present". Once the CFAR detector identifies potential targets based on thresholding, it generates a detection output indicating the presence and location of these targets in the original array. The output may include target coordinates or a binary mask indicating the detected target areas, which is shown in Fig. 4.2. It can be noted that the point targets close to the radar are detected correctly by comparing with Fig. 4.1d.

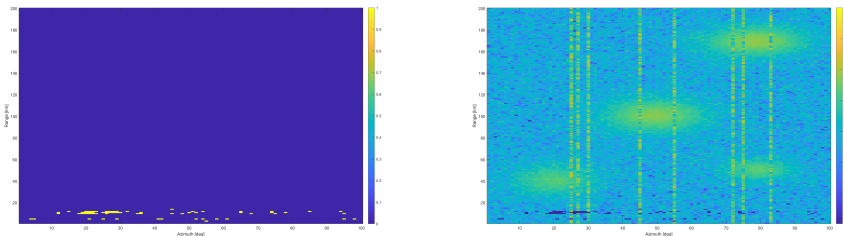


Figure 4.2: Point Target Mask and Result After Point Target Removal

4.3.2. PHASE NOISE DETECTION

Phase noise can be identified by its characteristics: high-level and exist at specific azimuths. Calculating the normalized mean along the range, and then scaling them up to plot the Fig. 4.3, the phase noise can be masked in Fig. 4.4.

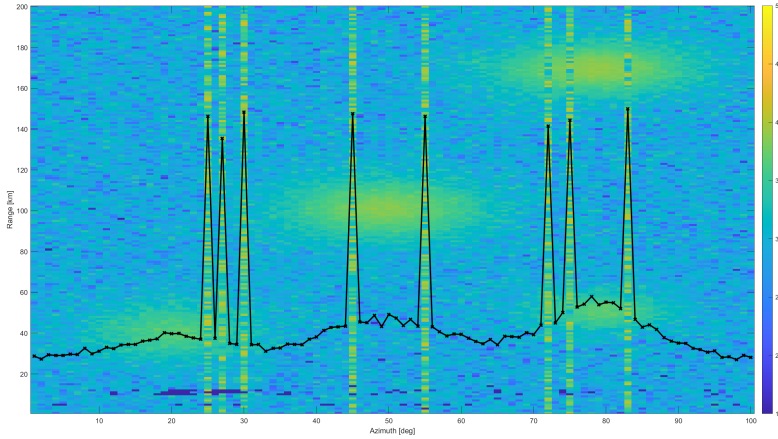


Figure 4.3: Scaled Mean Along Range Dimension

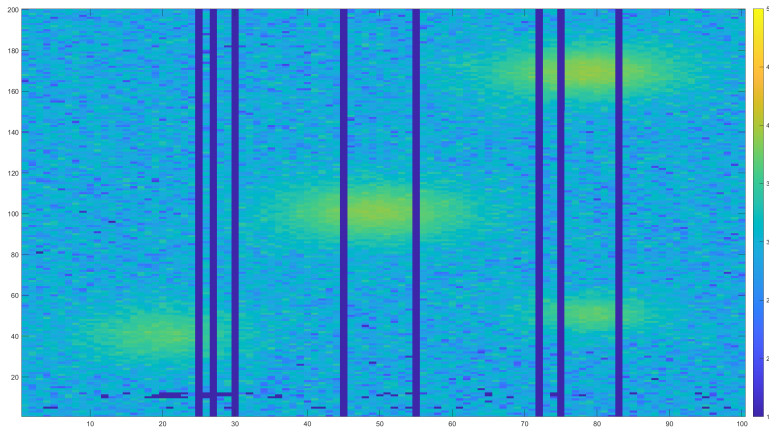


Figure 4.4: Result After Removing Azimuths Existing Phase Noise

4.3.3. WAVELET DENOISE

Since the target signals get contaminated with noise, wavelet-based techniques are applied to denoise. Wavelet denoising is a signal processing technique used to reduce noise from a signal while preserving important features and structures. It is based on

the principles of wavelet analysis, which allows for both time and frequency localization of signals. The basic idea behind wavelet denoising is to decompose the noisy signal into its wavelet coefficients using a wavelet transform, apply a thresholding operation to these coefficients to remove the noise, and then reconstruct the denoised signal using the modified coefficients. Here's an overview of the steps involved in wavelet denoising:

1. Signal Decomposition

The first step is to decompose the noisy reflectivity values into the wavelet coefficients using Discrete Wavelet Transform (DWT). The wavelet transform allows the signal to be represented in terms of different scales and positions (or time points). This provides a multi-resolution representation, where high-frequency details are represented in the higher scales, and low-frequency trends are represented in the lower scales.

2. Thresholding

After the signal is decomposed, wavelet coefficients at each scale are individually analyzed to determine their significance. The key idea in wavelet denoising is that noise tends to have smaller amplitudes compared to signal components. So, a thresholding operation is applied to the wavelet coefficients, which sets small coefficients to zero, effectively removing the noise. There are different thresholding methods that can be used, such as: (1). Hard Thresholding: Set coefficients below a certain threshold to zero. (2). Soft Thresholding: Shrink coefficients toward zero by an amount specified by the threshold. (3). Non-Linear Thresholding: More advanced methods based on statistical models.

3. Signal Reconstruction

Once the thresholding is applied to the wavelet coefficients, the denoised signal is obtained by reconstructing the signal using the modified coefficients. The reconstruction process combines the denoised coefficients from different scales to obtain the final denoised signal. This process of reconstruction is known as an Inverse Wavelet Transform (IDWT).

To select the wavelet type and level which can function well for the simulation data, the "Wavelet Analyzer" in-built tool within MATLAB is utilized, allowing importing the noisy reflectivity image and choosing different types and levels of wavelet transmission to obtain the denoised image. From the in-built tool, it can be found that orthogonal wavelets have better denoising performance than biorthogonal wavelets. Since the image may be less informative than the matrix itself, different types of orthogonal wavelets are applied to the matrix values. The "Haar" wavelet is chosen, and the decomposition level is determined to be 2. By comparing the soft thresholding and hard thresholding methods, soft thresholding is performed on the detail coefficients of the wavelet decomposition vector. This thresholding step selectively removes small-scale noise components while preserving important features, effectively denoising the data. After reconstruction, a cleaner and more refined reflectivity map is shown in Fig. 4.5.

Although wavelet denoising techniques have many advantages, such as being effective in preserving important features of the signal while reducing noise and being well

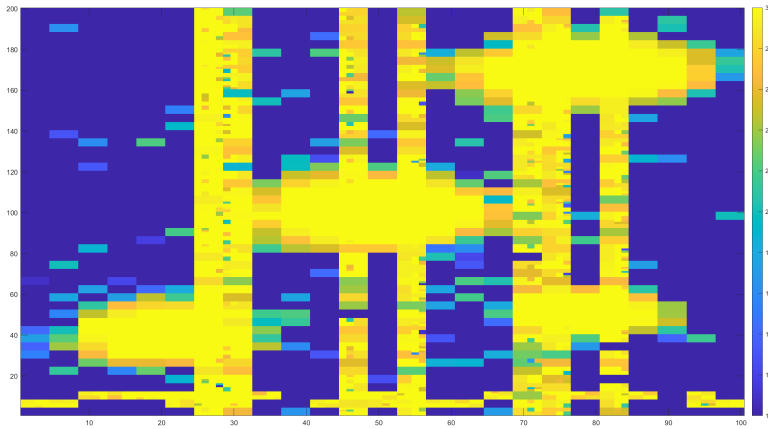


Figure 4.5: Result After Wavelet Denoising

suited for multi-resolution signal analysis, there are some limitations of the wavelet denoising technique. The selection of an appropriate threshold can be challenging and may depend on the characteristics of the noise and signal. Wavelet denoising may introduce some artifacts in the denoised signal, especially when aggressive thresholding is used. And it may not work well for signals with a very low signal-to-noise ratio (SNR).

4.3.4. MORPHOLOGICAL OPERATION

Following the wavelet denoising phase, the subsequent steps require the use of morphological operations to further refine specific features of interest within the reflectivity map. Morphological techniques, encompassing operations like dilation or erosion, are judiciously applied to accentuate or smooth these features.

By manipulating the shape and proportions of targeted regions, it becomes feasible to enhance the visibility and distinctness of the targets embedded within the radar data. This undertaking involves the creation of a primary binary mask, exemplified in Fig. 4.6, which is subsequently subjected to morphological operations.

The primary binary mask is crafted through standard thresholding of the wavelet denoised signal. This entails setting a threshold value that segregates signal components from noise. The resulting binary mask effectively segregates target regions from background clutter, thereby facilitating subsequent morphological operations to be precisely targeted to amplify the desired features while suppressing undesired elements.

By comparing the mask generated by morphological operations and the ground truth, the optimum morphological operations, in this case, are chosen to be: (1) first open; (2) then filling with holes. The structure element used is a disk shape.

The "open" morphological operation proves most effective in scenarios where the primary objective is the elimination of minor noise or delicate structures while maintaining the overall form and prominent characteristics of objects within an image. This

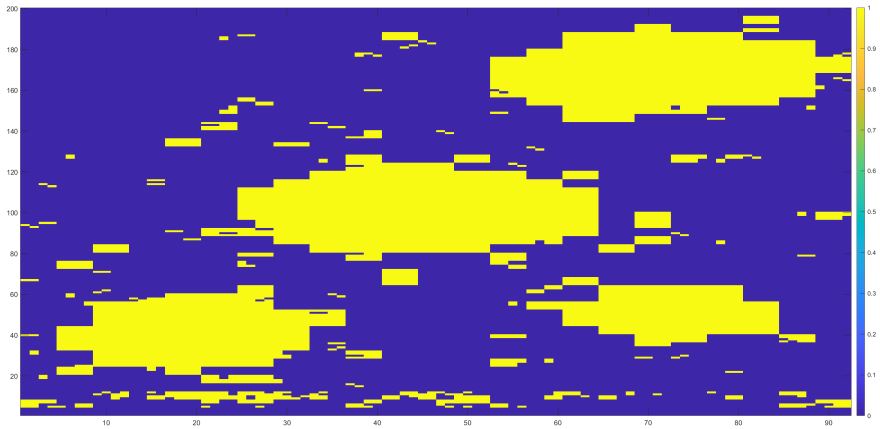


Figure 4.6: Primary Binary Mask by Thresholding the Denoised Values and Removing Azimuths Existing Phase Noise

operation involves a combination of two fundamental morphological processes: erosion, followed by dilation.

Erosion entails the movement of a structuring element, often a small binary mask, across the image. In this process, each pixel in the image is substituted with the lowest value among the pixels encompassed by the structuring element. This step effectively erodes the outer pixels of objects and eradicates small, isolated regions.

On the other hand, dilation involves using the same structuring element to traverse the image. Each pixel is replaced with the highest value from the pixels covered by the structuring element. This operation enlarges objects and fills minute gaps or voids within them. The notion of "filling with holes" aligns with a specific instance of the "closing" operation, which comprises dilation followed by erosion. This operation rectifies small cavities within objects, enhancing their completeness and continuity. It facilitates the smoothing of object boundaries and reinforces the interconnectedness of objects in the image.

The outcome after this procedure is visualized in Fig. 4.7.

An essential consideration lies in the selection of the structure element and the determination of the number of iterations for the morphological operation. These parameters require adjustment according to the unique attributes of the image and the dimensions of the voids or openings that need rectification.

Resizing and iterating structure elements is critical to achieving effective results. For example, employing larger structural elements or performing multiple iterations may prove essential to successfully address more substantial voids. However, care must be taken to prevent over-smoothing or inadvertently merging adjacent objects.

Striking an appropriate balance between structuring element size, number of iterations, and image features is critical to achieving optimal results.

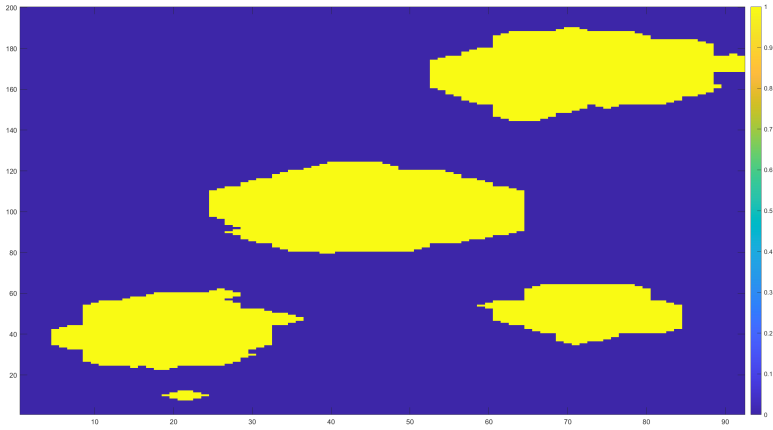


Figure 4.7: Binary Image After Applying Morphological Operation on the Primary Binary Mask

4.3.5. RESTORATION OF PHASE NOISE AZIMUTHS

Having performed the necessary processing and enhancements, the next step is to restore the phase noise azimuths that were marked as void previously, as shown in Fig. 4.8.

These void regions are replaced with zeros, ensuring that the reflectivity map is complete and does not contain any missing or distorted information due to the phase noise.

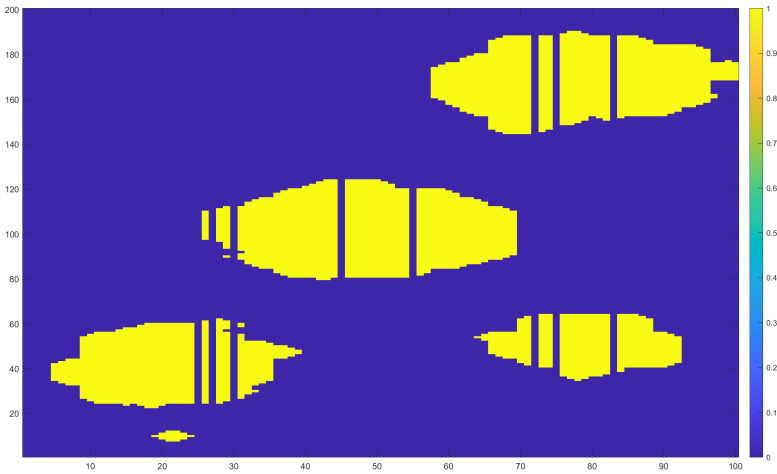


Figure 4.8: Result After Restoring Azimuths Existing Phase Noise with Zeros

This step guarantees the integrity and coherence of the reflectivity data, providing a more accurate representation of the detected targets.

4.3.6. GAP FILLING

The final step in the target mapping pipeline is gap-filling and clearing out the point targets using the mask obtained in the first step. Despite the previous processing steps, there may still be small gaps or discontinuities in the reflectivity map. To address this, another morphological operation is applied to fill in these gaps. By selectively expanding or contracting target regions, the target mapping becomes continuous and coherent, resulting in a more reliable and comprehensive representation of the targets detected by the radar system. After Moving out the point targets, the final target mask is shown in Fig. 4.9. The Mean Square Error between this mask and the ground truth is 0.0875, meaning that in the whole matrix, there is 18 percent of the pixels detected wrongly.

4

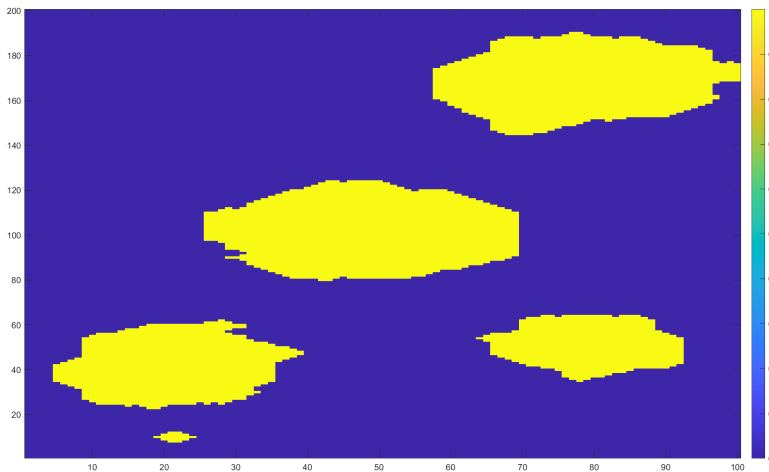


Figure 4.9: Final Binary Mask Derived from the Simulation Model Using Morphology-based Target Mapping Pipeline

Applying this target mapping pipeline based on reflectivity aims to enhance the quality of the radar data, remove noise and artifacts, and produce an accurate and detailed map of the detected targets.

4.3.7. EVALUATION AND PERFORMANCE ANALYSIS

The effectiveness of the proposed target mapping pipelines could potentially be influenced by the Signal-to-Noise Ratio (SNR). To comprehensively assess their performance under varying SNR conditions, a model is constructed for experimentation.

This model creation involves the generation of a target with uniform reflectivity across its entirety. Subsequently, White Gaussian Noise (WGN) is introduced, both globally and

selectively for specific azimuths, to emulate the presence of noise within the radar data. Furthermore, to simulate the impact of phase noise, regions exhibiting elevated reflectivity across all ranges are incorporated.

To gauge the performance under different SNR scenarios, models are constructed for SNR values of 20 dB. These models, exemplifying the interaction between target mapping pipelines and SNR, are visually illustrated in Fig. 4.10.

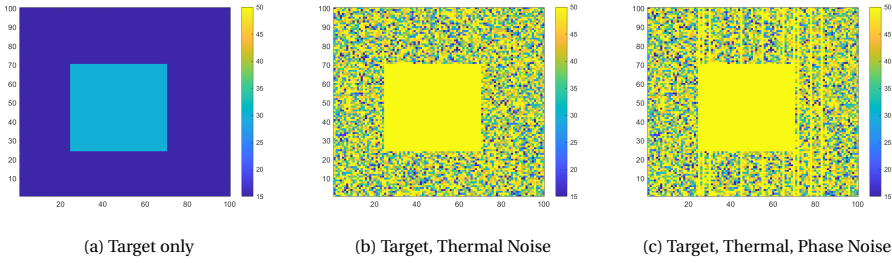


Figure 4.10: Model Used to Evaluate Target Mapping Pipelines at SNR = 20dB

Besides MSE, there are other parameters used to evaluate the performance of the processing pipelines. Precision is defined as equation 4.6. It measures the accuracy of the positive predictions made by the detection algorithm. Recall is defined as equation 4.7. It measures the ability of the detection algorithm to identify positive instances correctly. Both the precision and recall are calculated based on FN (False Negative) and TP (True Positive). The F1Score is the harmonic mean of precision and recall and provides a balance between precision and recall, calculated with equation 4.8. Intersection over Union (IoU) measures the overlap between the predicted bounding boxes and the ground truth bounding boxes, with the equation 4.9.

$$\text{Precision} = \frac{TP}{TP + FP} \quad (4.6)$$

$$\text{Recall} = \frac{TP}{TP + FN} \quad (4.7)$$

$$\text{F1Score} = 2 \frac{\text{Precision} \cdot \text{Recall}}{\text{Precision} + \text{Recall}} \quad (4.8)$$

$$\text{IoU} = \frac{\text{Area of Intersection}}{\text{Area of Union}} \quad (4.9)$$

$$(4.10)$$

where T, F, P, N means "True", "False", "Positive", and "Negative".

With the model, measures of the performance dependence on the SNR can be plotted in Fig. 4.11. As SNR increases, MSE gets lower and converges to 0.01, meaning there are 0.01 percent of the pixels in the whole model detected wrongly. This algorithm works badly when SNR is smaller than -20dB with an MSE of approximately 0.42.

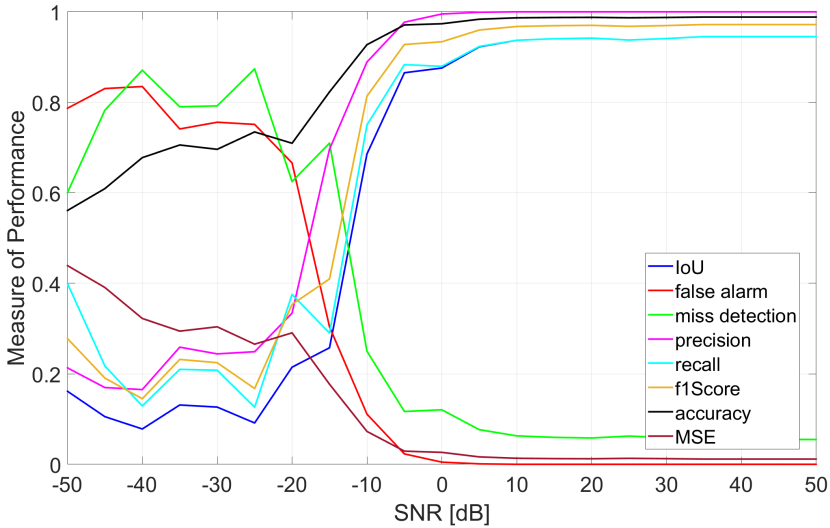


Figure 4.11: Performance Measures Dependence on SNR for Morphological-based Target Mapping Pipeline

For cases where SNR is lower than -20 dB, the performance of the morphology-based target mapping pipeline is poor, with a 0.3 F1Score. For cases where SNR is larger than 20 dB, the performance of the morphology-based target mapping pipeline has a 0.98 F1Score.

4.4. ENTROPY-BASED TARGET MAPPING PIPELINE

The second target mapping pipeline is inspired by classification since the real-world reflectivity data could be considered as a combination of four classes:

$$f(x, y) = s_1(x, y) + s_2(x, y) + n(x, y) + p(x, y) \quad (4.11)$$

where $f(x, y)$ represents the observations in each pixel, $s_1(x, y)$ the point targets, $s_2(x, y)$ the extended targets of interest, $n(x, y)$ the global thermal noise, and $p(x, y)$ the phase noise existing in specific azimuths. Each class can be characterized from two aspects, as the table 4.1 shows. To get the mask of s_2 , the improved pipeline is built to distinguish each class.

	Reflectivity	Distribution
s_1	High, >50dB	Concentrate
s_2	Middle, [30,50]dB	Spread
n	Low, [15,30]dB	Spread
p	Middle to High, >40dB	Along ranges

Table 4.1: Characteristics of the Four Classes in Radar Data

With the definition of four classes involved in the observations, the classifier is designed following the decision tree, shown in Fig. 4.12.

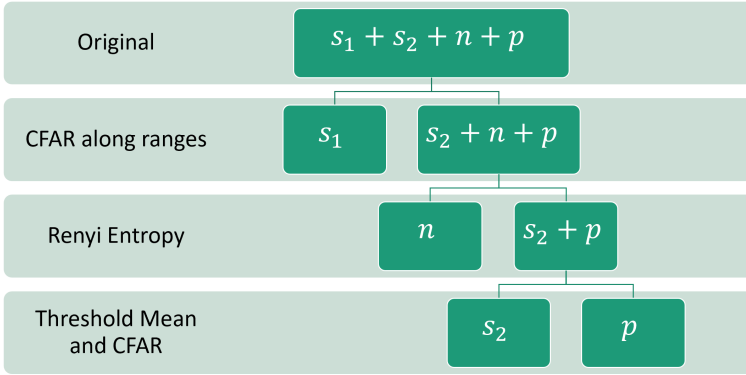


Figure 4.12: Decision Tree for Classifier (Entropy-based Target Mapping Pipeline)

This target mapping pipeline consists of the following parts: point target detection using CFAR, thermal noise detection using a threshold provided by Rényi's entropy, and phase noise detection by a combination of CFAR and thresholding the normalized mean.

4.4.1. POINT TARGETS DETECTION USING CFAR ALONG RANGES

This stage is also included in the first target mapping pipeline. But in this pipeline, the difference is that the point targets are masked and removed for further process. The point target mask and the result after removing the point target are shown in Fig. 4.2.

4.4.2. THERMAL NOISE DETECTION USING RÉNYI ENTROPY

After distinguishing the s_1 , the noise can be detected by Information Entropy Techniques. Shannon's entropy, also known as Shannon entropy or information entropy, is a widely used measure of uncertainty or information contained in a probability distribution. It quantifies the average amount of information required to describe an event from the distribution. Shannon's entropy is defined as:

$$H(X) = - \sum_{i=1}^N p(x_i) \log_2 p(x_i) \quad (4.12)$$

where $H(X)$ is the entropy of the random variable X , $p(x)$ is the probability of the event x , and the summation is taken over all possible events x_1, x_2, \dots, x_N in the distribution. Shannon's entropy is non-negative and reaches its maximum value when the probability distribution is uniform.

Rényi's entropy, named after Alfréd Rényi, is a family of entropy measures that generalize Shannon's entropy. Rényi's entropy is defined as:

$$H_\alpha(X) = \frac{1}{1-\alpha} \log_2 \left(\sum_{i=1}^N p(x_i)^\alpha \right) \quad (4.13)$$

The difference is that $H_\alpha(X)$ introduces parameter α to control the order of the Rényi entropy. Different values of α yield different entropy measures. When α approaches 1, Rényi's entropy converges to Shannon's entropy. Rényi's entropy provides a more flexible framework for measuring the uncertainty or information contained in a distribution. It allows for different orders of entropy that can capture different aspects of the distribution. When α is less than 1, Rényi's entropy gives more weight to the events with higher probabilities, focusing on the most probable outcomes. In the radar measurements, there are several types existing, as discussed previously. Each type can be considered as a probability distribution. Then the key to classifying types is to distinguish by thresholding. Using the probability of values existing on the dataset to realize the classification can be proved in Fig. 4.13.

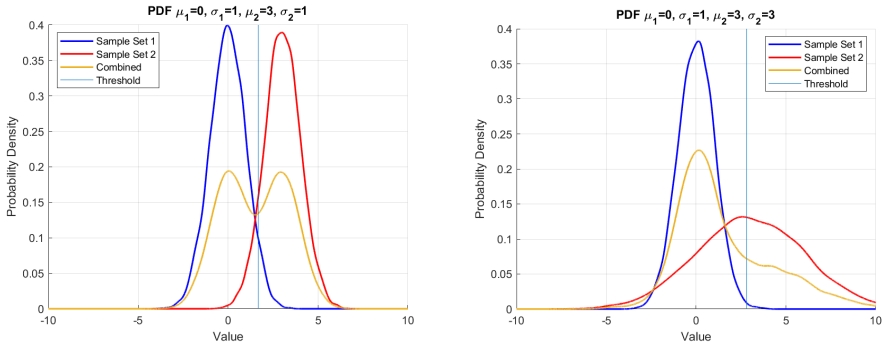


Figure 4.13: Distribution Sets to Validate the Threshold Provided by Rényi's Entropy

The threshold provided by Entropy is around the cross point of two distributions when they have the same variance. While in the cases where the variances are different, the cross point could be biased to the wider one.

Using Rényi Entropy to create a target mask was proposed in the paper [33]. Rényi entropy is a mathematical measure that quantifies the uncertainty or randomness in a probability distribution. It can be utilized to analyze the distribution of pixel intensities in an image matrix and aid in the classification task. Here's the approach to using Rényi Entropy to distinguish the thermal noise:

(1). Compute the probability distribution of value bins within the matrix. This can be achieved by counting the occurrences of each value bin and normalizing them to obtain probabilities. Let $p_i = p(x_1), p(x_2), \dots, p(x_k)$ be the probability distribution for a matrix with k different value bins.

(2) From this distribution, object distribution which represents the WGN, and background distribution, which contains all the remaining information, can be obtained. Denote the object distribution and background distribution as:

$$p_A : p_1/P_A, p_2/P_A, \dots, p_t/P_A \text{ and } p_B : p_{t+1}/P_B, p_{t+2}/P_B, \dots, p_k/P_B \quad (4.14)$$

where $P_A = \sum_{i=1}^t p(x_i), P_B = \sum_{i=t+1}^k p(x_i)$.

(3). Calculate the Rényi entropy using the probability distribution. The Rényi entropy

of order α for each distribution is given by:

$$H_{\alpha}^A(t) = \frac{1}{1-\alpha} \log_2 \left(\sum_{i=1}^t (p_i/P_A)^{\alpha} \right) \quad (4.15)$$

$$H_{\alpha}^B(t) = \frac{1}{1-\alpha} \log_2 \left(\sum_{i=1}^t (p_i/P_B)^{\alpha} \right) \quad (4.16)$$

(4). Set a threshold value by considering the distribution of values for object and background regions. This appropriate threshold is aimed at maximizing the difference or distinctiveness between the object and background distributions. It implies that this threshold can maximize the information gain or reduction in entropy when separating the two classes. In other words, the threshold should be chosen such that it results in the largest reduction in uncertainty or randomness when differentiating objects from the background, minimizing the overlap and improving the accuracy of classification. The threshold t is denoted by:

$$t(\alpha) = \underset{t}{\operatorname{argmax}} [H_{\alpha}^A(t) + H_{\alpha}^B(t)] \quad (4.17)$$

(5). Create a binary mask by comparing the value of each pixel in the matrix with the threshold. If the value exceeds the threshold, classify the pixel as part of the object. Otherwise, classify it as part of the background. In this case, the optimum α is found to be 0.2, which is effective in distinguishing the thermal noise.

The thermal noise mask and the result after removing the thermal noise are shown in Fig. 4.14.

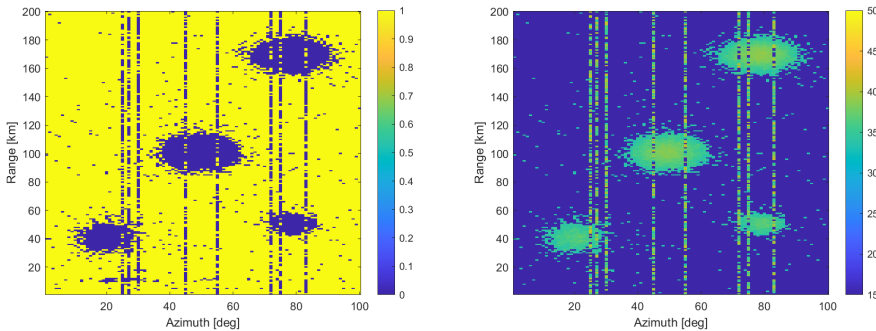


Figure 4.14: Mask for Thermal Noise and Result After Removing Thermal Noise

4.4.3. PHASE NOISE DETECTION

After removing the thermal noise, the phase noise can be identified with CFAR and thresholding the mean along the range. It is visible that the phase noise exists in specific azimuths with high-level values and occupies more pixels along ranges than the target of interest. Therefore, implementing CFAR along azimuth can give the phase noise mask as Fig. 4.15 shows. Another criterion is to filter out these azimuths by limiting the number

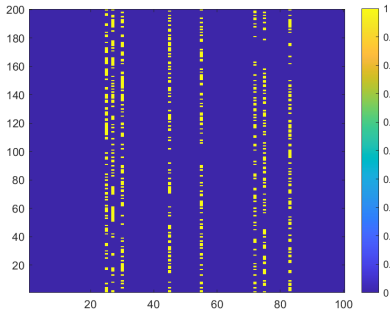


Figure 4.15: Mask for Phase Noise Detected by CFAR

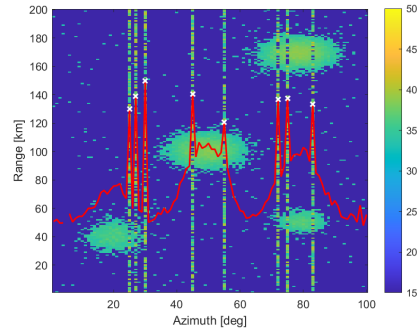


Figure 4.16: Scaled Mean Along the Range Dimension

4

of pixels with invalid values and the normalized mean along ranges bigger than 0.45. The scaled normalized mean along the range is present in Fig. 4.16.

In Figure 4.16, the identified peaks, which are marked as white crosses, bear significance as they correspond to the azimuths affected by phase noise. This occurrence marks a critical point for phase noise detection and subsequent mitigation.

The synergy of two techniques, namely CFAR processing, and thresholding the mean, ultimately reveals the unique pattern of phase noise. This process generates a depiction of the phase noise detection, as depicted in Figure 4.17. By applying the principles of the CFAR approach and considering the thresholded mean, the resultant plot showcases the success of phase noise removal, illustrated in Figure 4.18.

This integrated approach underscores the capacity of the methodology to effectively detect and eliminate phase noise, enhancing the accuracy and reliability of the target mapping procedure.

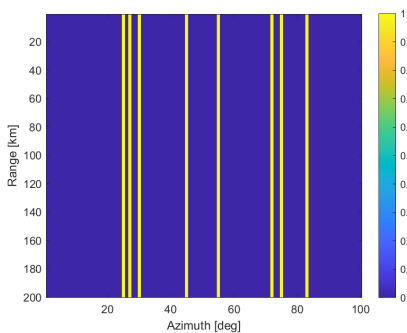


Figure 4.17: Mask for Phase Noise

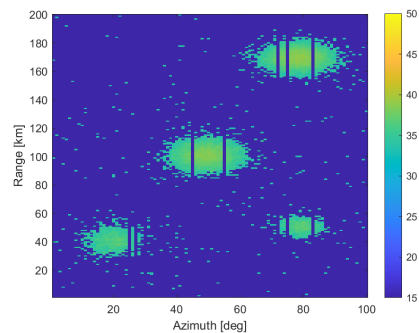


Figure 4.18: Result After Phase Noise Removal

The resultant outcome of the entropy-based target mapping pipeline is displayed in Fig. 4.19. In this particular instance, the Mean Squared Error (MSE) computed between the ground truth and the final detection mask is equal to 0.13245.

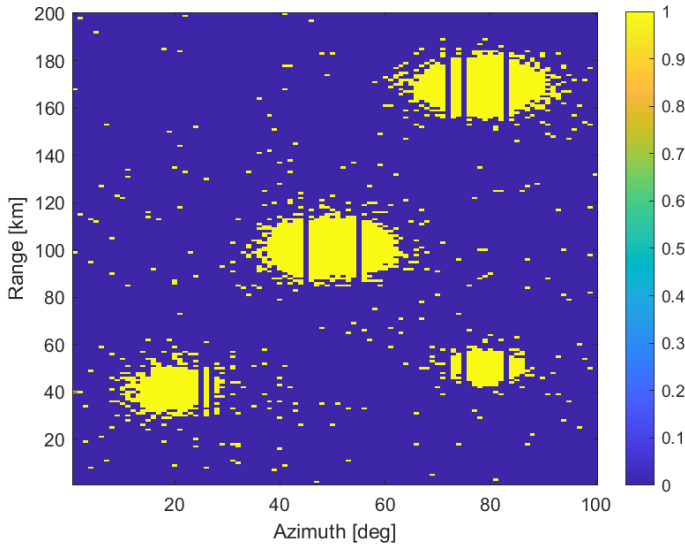


Figure 4.19: Mask for Extended Targets

The MSE, in essence, quantifies the dissimilarity between two binary masks. Its interpretation can be understood as reflecting both the number of instances where detections were missed as well as the occurrences of false alarms. This MSE summarizes the accuracy of the object mapping process, outlining the trade-off between correctly identifying targets and incorrectly identifying non-targets.

4.4.4. EVALUATION AND PERFORMANCE ANALYSIS

By implementing the identical operations as those presented in the first pipeline, the efficacy of the second pipeline can be assessed through the depiction of performance measures about the signal-to-noise ratio(SNR). This analysis is illustrated in Fig. 4.20.

Observing the Fig. 4.20, a notable observation emerges that the entropy-based target mapping pipeline exhibits a performance pattern similar to that of the morphology-based pipeline. The dependency of performance measures on SNR exhibits a congruent trend between these two processing pipelines. It's worth highlighting that the performance measures of the entropy-based target mapping pipeline demonstrate less pronounced fluctuations compared to the measures of the morphology-based target mapping pipeline.

This observation indicates comparable performance levels between the two target mapping pipelines, indicating that the entropy-based approach might offer comparable results in terms of target mapping accuracy and reliability, while potentially showing enhanced stability under varying SNR conditions.

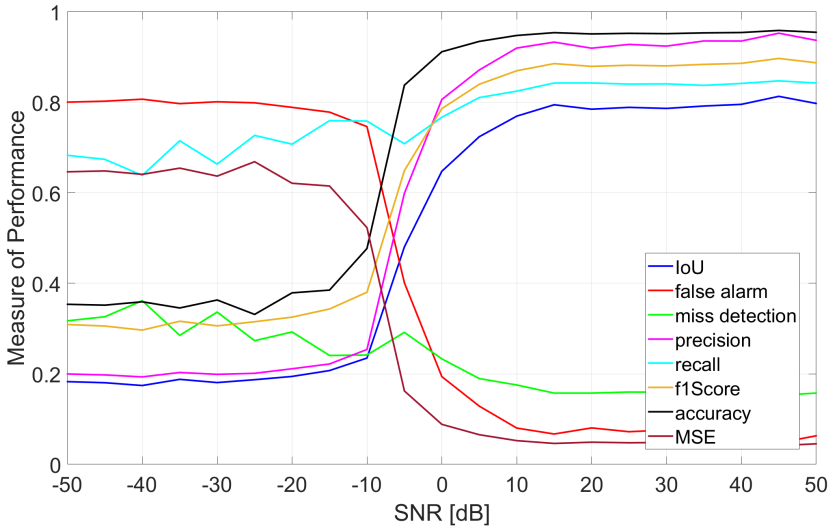


Figure 4.20: Performance Measures Dependence on SNR for Entropy-based Target Mapping Pipeline

4.5. COMPARISON OF TWO PROCESSING PIPELINES

To compare the target mapping performance of the proposed two pipelines, four parameters are taken into consideration: IoU, false alarm rate, missed detection, and F1Score. From the Fig. 4.21, it can be noticed that around -15 dB, the curves can be divided into two portions: below -15dB low SNR region and above -15dB high SNR region. For the four parameters, it can be said that higher-value IoU, lower-value false alarm rate, lower-value missed detection, and higher-value F1Score mean better performance.

It can be observed that in the low SNR region, the morphology-based target mapping pipeline has the following characteristics compared with the entropy-based one:

1. lower IoU;
2. similar false alarm rate but more fluctuated;
3. higher missed detection;
4. lower F1Score.

Therefore, the comprehensive evaluation shows that the performance of the morphology-based target mapping pipeline exhibits a decline compared to the entropy-based target mapping pipeline in low SNR regions. This observation may be attributed to the limitations of wavelet denoising techniques in effectively reducing the noise to a level that enables target detection.

In the morphology-based target mapping pipeline, the application of morphological operations is crucial to detect high-intensity point targets that were previously masked by noise. However, in scenarios with high-level phase noise, these operations may inadvertently amplify the risk of introducing false positives.

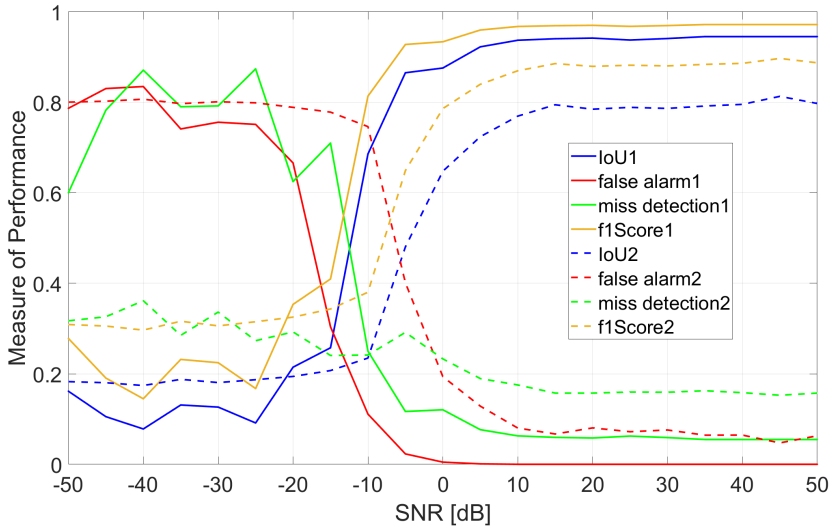


Figure 4.21: Comparison of the Performance Measure for Morphology-based and Entropy-based Target Mapping Pipelines

As for the high SNR region (above -15 dB), the morphology-based target mapping pipeline has the following characteristics compared with the entropy-based one:

1. higher IoU;
2. lower false alarm rate;
3. lower missed detection;
4. higher F1Score.

It means that in the high SNR region, the morphology-based target mapping pipeline performs better than the entropy-based target mapping pipeline. So selecting the suitable pipeline should depend on the application itself. And it is worth mentioning that the morphology-based target mapping pipeline has a larger fluctuation, meaning it may be more vulnerable.

4.6. FINAL TARGET MAPPING OF THE REAL-WORLD DATA

Implementing the proposed pipelines on the real-world data, the intermediate results are obtained. Applying the final masks maps the target of interest.

4.6.1. MORPHOLOGY-BASED PIPELINE APPLIED ON REAL-WORLD DATA

For the morphology-based target mapping pipeline, the results are drawn in Fig. 4.22.

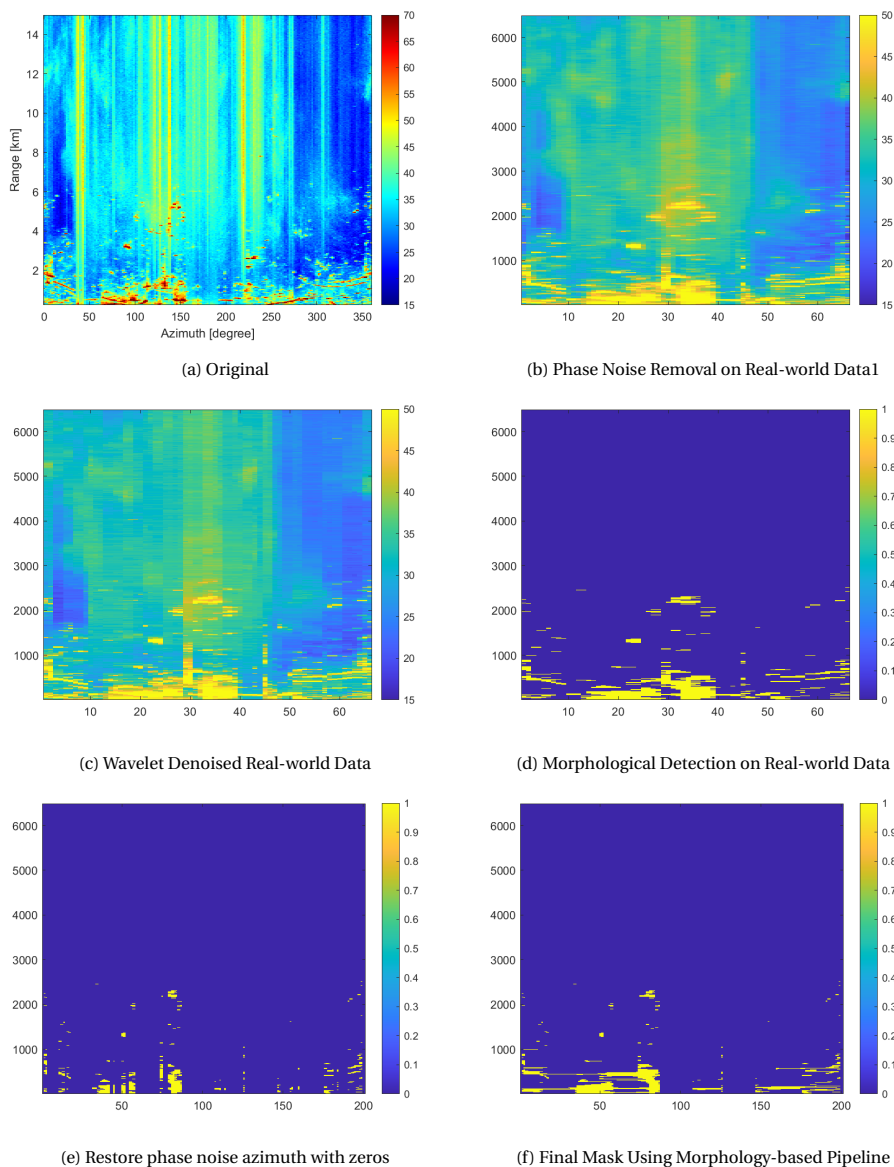


Figure 4.22: Results of Morphology-based Pipeline on Real-world Data

4.6.2. ENTROPY-BASED PIPELINE APPLIED ON REAL-WORLD DATA

For the entropy-based target mapping pipeline, the results are drawn in Fig. 4.23.

It can be found that the entropy-based pipeline has better performance than the morphology-based one. The reasons could be:

1. The low SNR is dominant in the real-world data, which the morphology-based

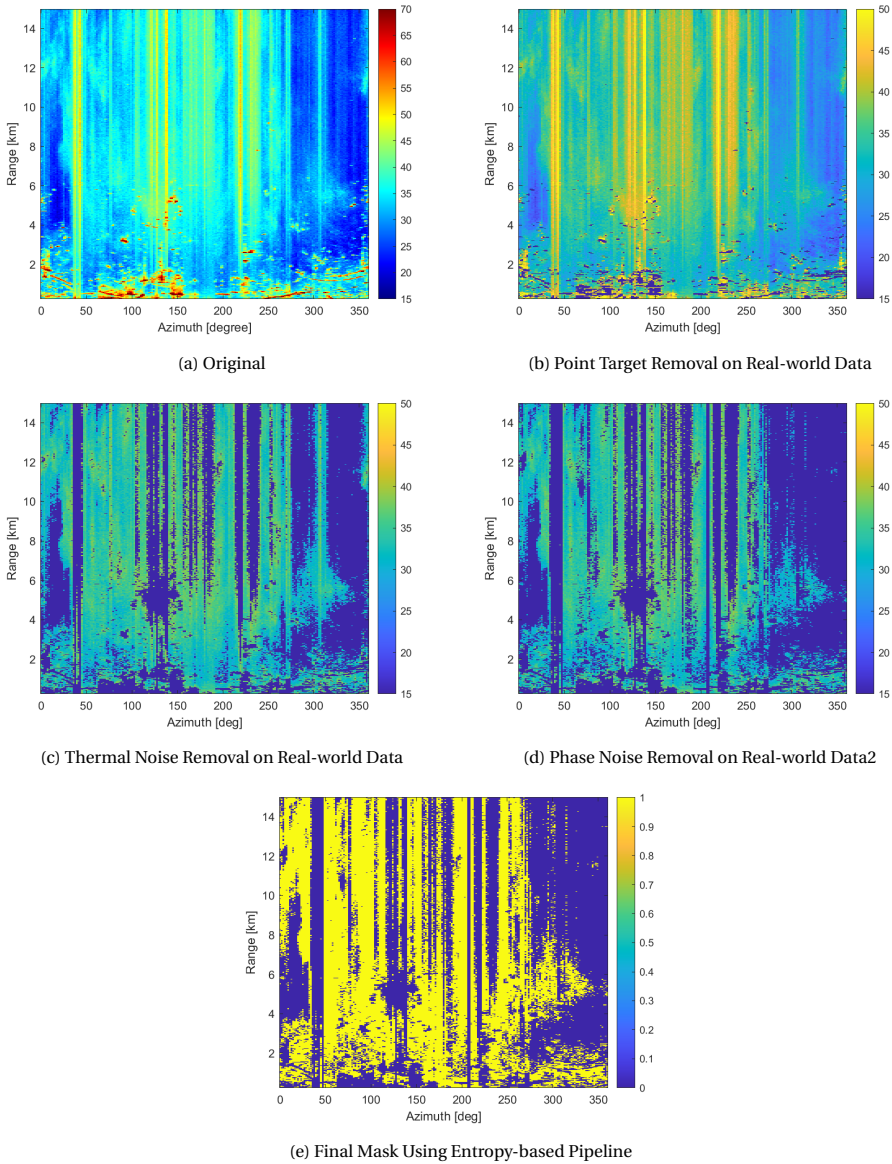


Figure 4.23: Results of Entropy-based Pipeline on Real-world Data

pipeline is not good at dealing with.

2. The disk-shaped structure element is well-suited for the simulation model. However, the size and shape of the extended targets existing in the real-world data are unknown, bringing the challenge of choosing the optimum structure elements.

The level of reflectivity from the extended targets makes it tricky to decide the correct wavelet type and transformation scale.

In addition, since the entropy-based pipeline is designed to identify the data types existing in the measurements, the mask for the different classes can be shown in Fig. 4.24.

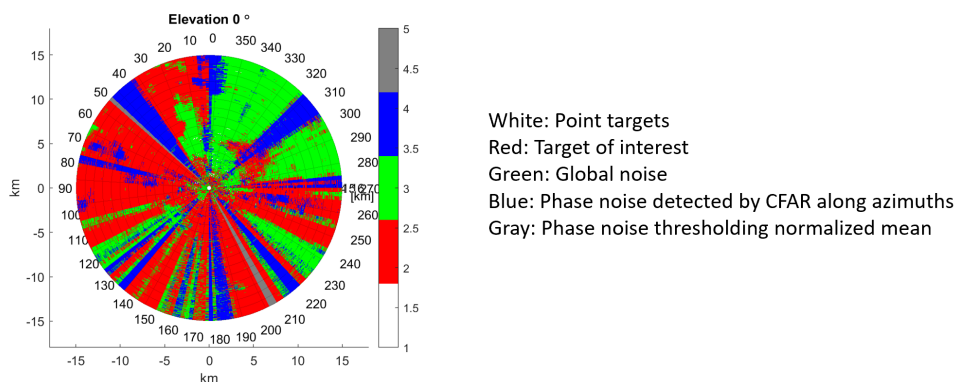


Figure 4.24: Class Identification of Real-world Data Provided by Entropy-based Target Mapping Pipeline

Utilizing the entropy-based pipeline, the before and after-processed PPI for real-world reflectivity can be plotted in Fig. 4.25.

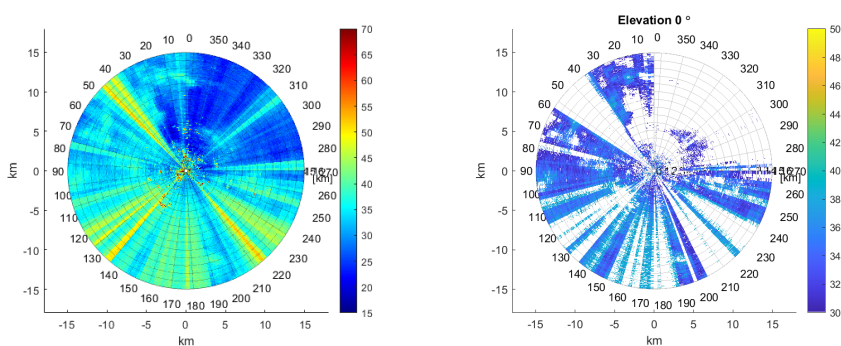


Figure 4.25: Before and After-processed PPI for Real-world Reflectivity Using Entropy-based Target Mapping Pipeline

4.7. FINAL TARGET MASK

In this section, the target binary mask for real-world data is introduced by taking into account the two masks obtained earlier: one from circular variance and the other from reflectivity using the entropy-based pipeline. By merging these two masks, the binary masks of intersection and union are displayed. The potential factors contributing to the variation between these two masks are also examined.

4.7.1. TARGET MASKS

As previously mentioned, the target binary mask derived from the circular variance is acquired based on the principle that when the circular variance exceeds the designated threshold, it can be determined as noise; conversely, if it falls below the threshold, it can be recognized as the target. Using the threshold of circular variance 0.8, the mask is shown in Fig. 4.26.

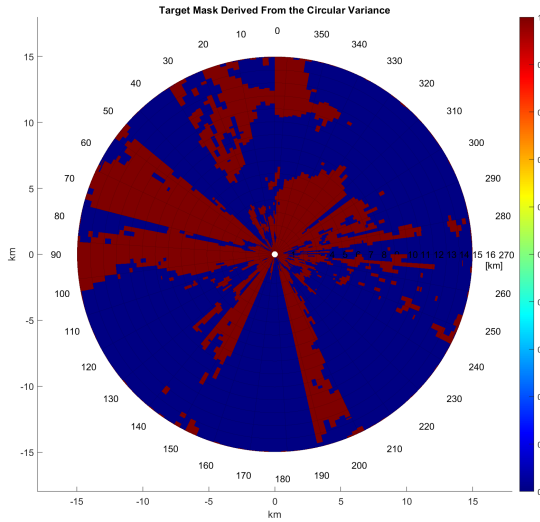


Figure 4.26: Mask Provided by Circular Variance of the Doppler Spectrum

The mask of the entropy-based target mapping pipeline is shown in Fig. 4.27.

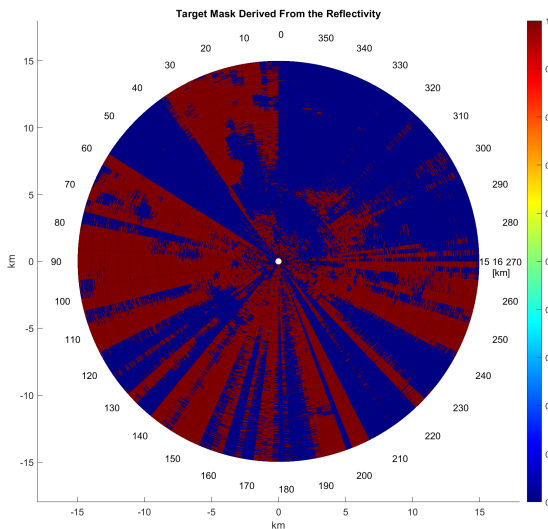


Figure 4.27: Mask Provided by Entropy-based Target Mapping Pipeline on Reflectivity

The mask which takes the two masks into combination is shown in Fig. 4.28, where green is the mask from the circular variance, blue represents the mask from the reflectivity, and red is the mask of intersection. Applying the intersection mask on the real-world data, the result is shown in Fig. 4.29.

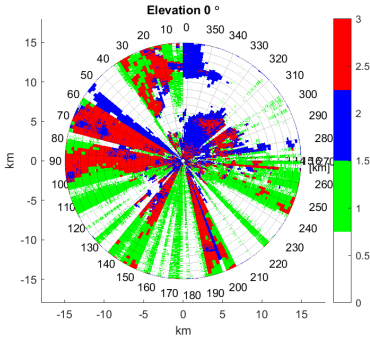


Figure 4.28: Combination of the Mask Provided by Circular Variance and the Mask Provided by Entropy-based Target Mapping Pipeline on Reflectivity

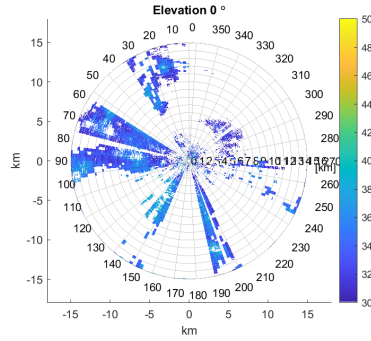


Figure 4.29: Intersection of the Mask Provided by Circular Variance and the Mask Provided by Entropy-based Target Mapping Pipeline on Reflectivity

The union of the two masks and the result after applying the union on the real-world radar reflectivity data are shown in Fig. 4.30 and 4.31.

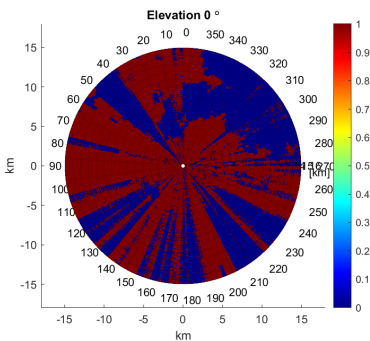


Figure 4.30: Union of the Mask Provided by Circular Variance and Mask Provided by Entropy-based Target Mapping Pipeline on Reflectivity

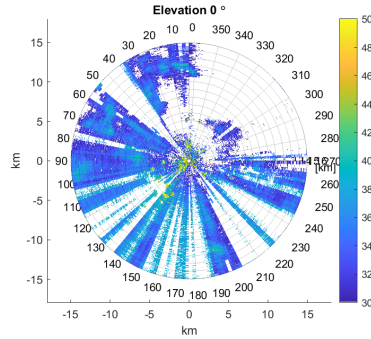


Figure 4.31: Apply Union of the Mask Provided by Circular Variance and Mask Provided by Entropy-based Target Mapping Pipeline on the Real-world Reflectivity

It can be observed that there are some pixels identified as objects by the circular variance and defined as noise by the entropy-based pipeline. It could happen if the extended target has insignificant reflectivity, which is not under the consideration of the pipeline. The reflectivity model 4.32 and 4.33 can prove it. The visibility of the targets depends on the bounds defining the targets.

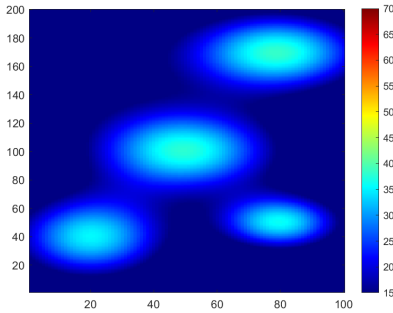


Figure 4.32: Reflectivity Model (target only)

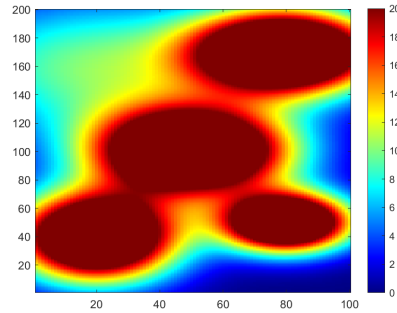


Figure 4.33: Reflectivity Model (target only but with lower bound)

4.8. CONCLUSION

In this chapter, two target mapping pipelines with a focus on reflectivity are proposed. The first pipeline, based on morphology, involves several steps: (1) identifying point targets using CFAR, (2) detecting phase noise by thresholding the mean along the range and excluding them, (3) wavelet denoising, (4) employing morphological operations to detect the target of interest, and finally (5) restoring the phase noise azimuths and filling any gaps using morphological techniques.

On the other hand, the second pipeline, which is entropy-based, consists of (1) identifying point targets using CFAR along the range, (2) identifying thermal noise using a threshold based on Renyi's entropy, and (3) detecting phase noise by combining CFAR along the azimuth and thresholding the normalized mean along the range.

Through evaluating the simulation model's performance, it can be concluded that when the Signal-to-Noise Ratio (SNR) is below -15dB, the entropy-based pipeline performs better. Conversely, when the SNR is above -15dB, the morphology-based pipeline is more effective. Some parameters to measure the performance are shown in table 4.2. The values are average in the low SNR and high SNR regions.

To substantiate the effectiveness of the target mapping pipelines, their practical applicability is tested on real data. The results of this implementation reveal a clear trend, which is the entropy-based pipeline exhibits superior performance compared to the morphology-based one. This performance difference is especially noticeable when deal-

		Low SNR (≤ -15 dB)	High SNR (>15 dB)
Morphology-based	IoU	0.1458	0.9099
	Flase Alarm Rate	0.7088	0.0108
	Missed Detection	0.7556	0.0835
	F1Score	0.2500	0.9513
Entropy-basede	IoU	0.1867	0.7084
	Flase Alarm Rate	0.7967	0.1603
	Missed Detection	0.3041	0.1843
	F1Score	0.3146	0.8159

Table 4.2: Summary of Performance Measures for Morphology-based and Entropy-based Pipelines

ing with extended objects with complex, scattered shapes and different sizes.

Another significant advantage inherent to the entropy-based pipeline is its ability to comprehensively represent the various data types contained in radar measurements. This broader perspective encapsulates the inherent ability to identify and classify the different types of information present in radar data.

Conclusions from real-world validations further support the notion that the entropy-based object mapping pipeline is a robust and general solution, especially in scenarios involving complex object structure and data type variations.

5

DOPPLER DEALIASING

This chapter begins by presenting a model that highlights the challenges posed by Doppler aliasing, which occurs when the actual Doppler frequency of a target exceeds the Nyquist limit. Doppler aliasing can lead to incorrect velocity measurements and hinder accurate target tracking and identification. Then it introduces a simple algorithm aimed at eliminating Doppler aliasing. Discussion of the approach, its challenges, and its limitations are present. Next, it explores an advanced existing dealiasing tool known as UNRAVEL. UNRAVEL employs a more sophisticated algorithm that considers 2D and even 3D continuity. Moreover, this chapter presents a novel approach to Doppler dealiasing based on optimization techniques. The development of this approach involves formulating the problem as an optimization task and utilizing optimization algorithms to find the best possible solution. By comparing and evaluating different optimization methods, their performance and effectiveness in dealing with Doppler aliasing can be assessed. The optimization results demonstrate the improved accuracy and reliability of the proposed Doppler dealiasing approach.

In summary, this chapter provides a comprehensive overview of Doppler de-aliasing techniques, including a gradient-based algorithm, advanced existing tools UNRAVEL, and optimizer-based methods. It discusses their rationale, challenges, limitations, and comparative performance. The findings and techniques presented in this paper contribute to advancing Doppler anti-aliasing methods, improving the accuracy of velocity measurements, and enabling more reliable target tracking and identification in radar data analysis.

In radar systems, the Doppler effect measures the velocity of moving targets. A target in motion induces a frequency shift in the radar signal known as the Doppler frequency. In some cases, the Doppler frequency can be modeled using a cosine function, resulting in what is referred to as a cosine-modeled Doppler velocity. The cosine-modeled Doppler velocity assumes that the target's velocity is constant and its motion is purely along the radial direction from the radar. This simplification is often applicable for targets moving at a relatively constant velocity and without significant changes in direction.

Aliasing in the Doppler domain arises when the Doppler frequency exceeds the Nyquist frequency. When aliasing occurs, the higher frequencies in the Doppler spectrum fold back into the lower frequencies, leading to incorrect measurement or representation of the Doppler velocity. This can result in false velocities or incorrect estimation of target motion. Aliasing is a significant problem in radar systems, as it can introduce ambiguity and distort the Doppler spectrum. Recall that the unambiguous Doppler is defined as:

$$|v_{Doppler}| \leq v_{unamb} = \frac{\lambda \cdot PRT}{4} \quad (5.1)$$

Then the observed velocity is related to the unambiguous velocity:

$$v_o = v_t \pm 2n v_{unamb} \quad (5.2)$$

where v_o is the observed velocity, v_t is the true velocity.

Assuming that the wind speed and direction are constant within the radar scan coverage, the horizontal wind-originated velocity $w_1, w_2, w_3, \dots, w_n$ as a function of the azimuth $a_1, a_2, a_3, \dots, a_n$ can be formulated as a cosine curve:

$$w_i = w_{max} \times \cos(a_i + \phi) \quad (5.3)$$

Here, w_{max} signifies the maximum horizontal velocity magnitude, while ϕ symbolizes the angle delineating the direction of the wind relative to the radar.

Since the radar measures the radial velocity, in cases where the elevation of the radar scan exhibits a non-zero value, the observed Doppler velocity $v_1, v_2, v_3, \dots, v_n$ at one constant elevation θ is also affected by the vertical speed of raindrops, which is dominated as a constant D as explained in the Fig. 5.1.

$$v_i = w_i \times \cos\theta + D \times \sin\theta \quad (5.4)$$

Then the observed Doppler velocity for a non-zero constant elevation scenario can be expressed as:

$$v_i = w_{max} \times \cos(a_i + \theta) \times \cos\theta + D \times \sin\theta \quad (5.5)$$

At elevation θ , let $v_{max} = w_{max} \times \cos\theta$ and $G = D \times \sin\theta$, equation 5.5 can be simplified as:

$$v_i = v_{max} \times \cos(a_i + \theta) + G \quad (5.6)$$

This equation (referred to as the Doppler equation) shows the relationship between observed Doppler velocity, azimuth angles, elevation, and the components of wind and vertical raindrop speed, providing a fundamental understanding of the observed velocity phenomenon in the cases of varying elevation angles.

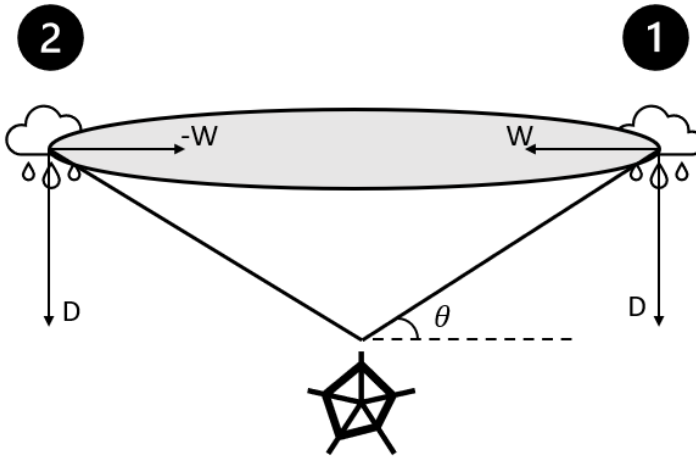


Figure 5.1: Demonstration of Raindrop Velocity with Elevation Angle Not Equal to Zero

Given $v_{max} = 1.5 \times v_{unamb}$, the sketch for the ideal situation where aliasing takes place is plotted in Fig. 5.2.

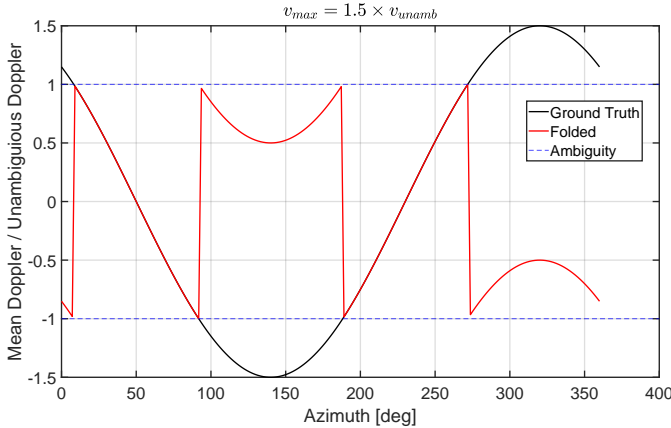


Figure 5.2: Velocity at Azimuths with Occurrence of Doppler Folding

5.1. MODEL USED TO EVALUATE THE DOPPLER DE-ALIASING TECHNIQUES

The lack of ground truth makes validating the Doppler dealiasing algorithms tricky. Considering the effect of thermal noise as the fluctuation and phase noise as missing data, the simulation model is built in MATLAB to evaluate the performance of dealiasing algorithms. The simulation model under the condition that the maximum fluctuation value is 1 [m/s] shows 10 percent missing data in Fig. 5.3.

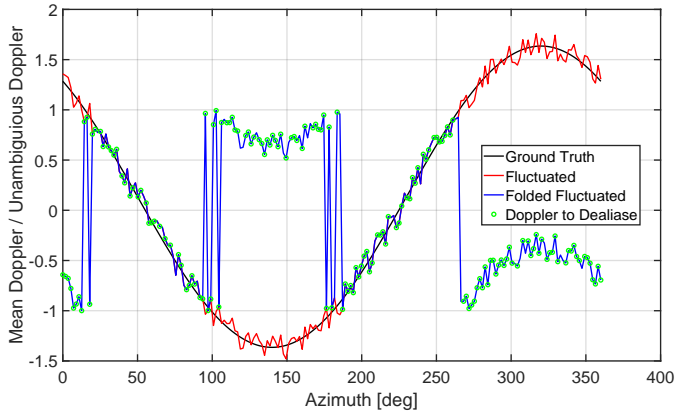


Figure 5.3: Doppler to dealias

5

5.2. SIMPLE ALGORITHM TO ELIMINATE DOPPLER ALIASING

From the filtered Circular Mean Doppler introduced in the section 3.6, it is discernible that the discontinuities caused by Doppler ambiguity are more distinct than that in the linear Mean Doppler plane. This section introduces a simple algorithm that checks the continuity along azimuth and eliminates the Doppler dealiasing.

5.2.1. APPROACH

The one-dimensional continuity approach takes advantage of the fact that the Doppler spectrum of a target typically exhibits a smooth and continuous behavior. By exploiting this continuity, it is possible to resolve the ambiguity caused by aliasing and correctly estimate the target's velocity [34]. The steps involved in using 1D continuity for dealiasing Doppler are as follows:

1. Find the discontinuity points by calculating the gradient. These points, whose gradients are above the threshold, will be defined as discontinuity points.
2. Cut the curve into pieces.
3. Make the piece-wise folded velocity-azimuth curve continuous. It can be achieved by adding $\pm 2n v_{\text{unamb}}$ to the first point within each piece until the gradient at that point is below the threshold.

5.2.2. RESULTS

Applying the simple algorithm based on the continuity along range dimension on the model introduced in Fig. 5.3, the de-aliased result is shown in Fig. 5.4, in which case the RMSE is 8.1 [m/s].

This algorithm is theoretically feasible but brings the challenges of deciding the threshold. It is possible that the gradient at some points could never fall short of the threshold if the threshold is too high. And reducing the threshold could diminish the sensitivity of

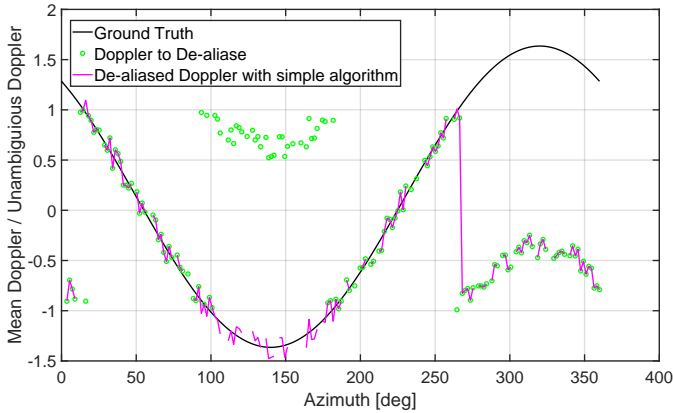


Figure 5.4: De-aliased Doppler Based on the Continuity Along Range

the discontinuity points. Besides that, with global noise and phase noise at specific azimuths, the gradients of such noisy velocity values become less informative in detecting the discontinuity points.

5.3. ADVANCED EXISTING DE-ALIASING TOOL UNRAVEL

UNRAVEL was proposed in the paper [26]. It is an open-source, modular, Doppler velocity dealiasing algorithm for weather radars. The advantages of UNRAVEL introduced are:

1. No need for external reference velocity data: UNRAVEL is an algorithm that does not require external reference velocity data, making it easily applicable.
2. Possibilities to be modified or replaced independently.
3. Good performance: UNRAVEL has shown good performance in dealing with Doppler velocity aliasing in weather radars. It takes advantage of the strengths of previous algorithms and constrains them to a certain domain of competence by putting checks and limitations on each module.
4. Automated scheme: UNRAVEL finds reference velocities in the input velocity field. It does not require manual intervention or external data sources.

The noisy velocity data is generated in the way as the model 5.5. Considering the situation of targets existing anywhere, meaning the velocity can be observed anywhere, the actual velocity, folded velocity, and unraveled velocity are present as follows. To analyze the factors which could affect the performance of UNRAVEL, under the assumption that the targets spread anywhere, there are four scenarios taken into account, respectively: (1). Target only, (2). Target and thermal noise, (3). Target and phase noise, and (4). Target, thermal noise, and phase noise. The results for the first scenario are shown in Fig. 5.5. The RMSE between the accurate velocities and UNRAVEL velocities is 0.17 [m/s].

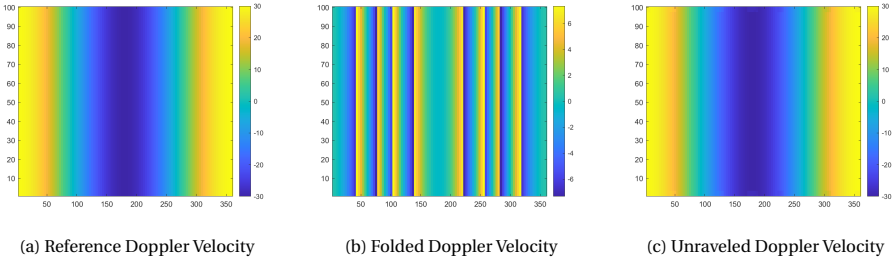


Figure 5.5: Results of UNRAVEL for Scenario: Targets Diffuse in All pixels and Targets Only

The processing ratio representing the percentage of valid data determined by UNRAVEL is 0.98.

The second scenario is all cell existing targets and global thermal noise. The results are present in Fig. 5.6. The RMSE between the true and UNRAVEL velocities is 10.25 [m/s]. The processing ratio representing the percentage of valid data determined by UNRAVEL is 0.60.

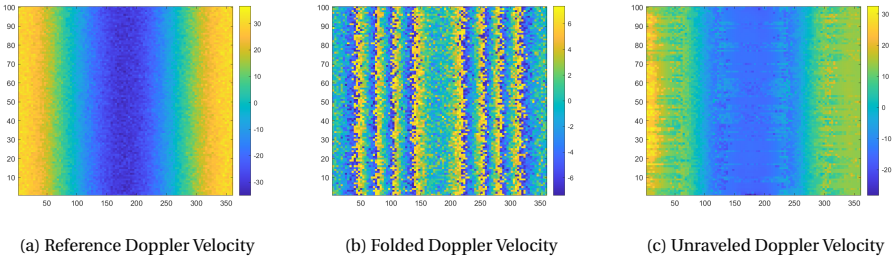


Figure 5.6: Results of UNRAVEL for Scenario: Targets Diffuse in All pixels and Targets, Thermal Noise Both Exist

The third scenario is all cell existing targets and specific azimuths existing phase noise. The results are present in Fig. 5.7. The RMSE between the true velocities and UNRAVEL velocities is 11.50 [m/s]. The processing ratio representing the percentage of valid data determined by UNRAVEL is 0.97.

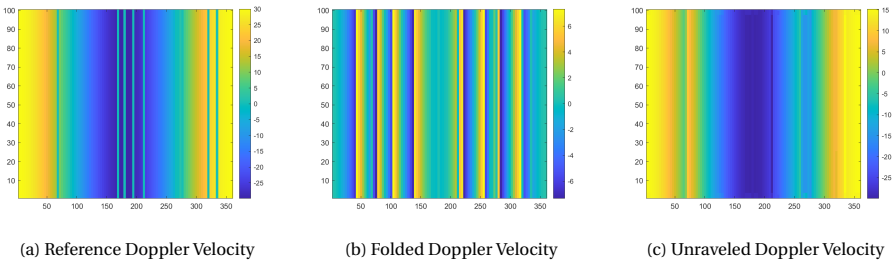


Figure 5.7: Results of UNRAVEL for Scenario: Targets Diffuse in All pixels and Targets, Phase Noise Exist

The last scenario is all cell existing targets, thermal noise, and specific azimuths existing phase noise. The results are present in Fig. 5.8. The RMSE between the true velocities and UNRAVEL velocities is 23.66 [m/s]. The processing ratio representing the percentage of valid data determined by UNRAVEL is 0.74.

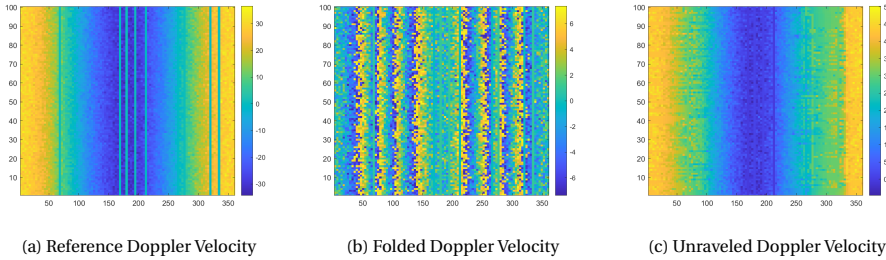


Figure 5.8: Results of UNRAVEL for Scenario: Targets Diffuse in All Pixels and Targets, Thermal Noise and Phase Noise All Exist

It is noted that the influence of thermal noise on the performance of UNRAVEL is more significant than phase noise since there is a smaller percentage of values processed. The RMSE and processing ratio can be summarized in the table 5.1.

Scenario (Target Diffuse in all pixels)	RMSE [m/s]	Processing Ratio
Target only	0.17	0.98
Target and thermal noise	10.25	0.60
Target and phase noise	11.50	0.97
Target, thermal noise, and phase noise	23.66	0.74
Target, thermal noise, phase noise with missing data	12.99	0.93

Table 5.1: Performance of UNRAVEL

In addition, there is another challenge existing in this case. Raindrops are not evenly distributed in the atmosphere. They can vary in size from very small droplets to larger raindrops, and they can be concentrated in specific areas or dispersed more widely depending on the weather conditions. When raindrops are detected by radar with a high resolution, they may span multiple resolution cells or be concentrated within a single cell, depending on their size and distribution. In some cases, rain could exist at all resolution cells within the radar's coverage area if there is a widespread and uniform rain event. However, more often, raindrops will be present in specific areas or regions, leading to variations in radar reflectivity across the coverage area. It means only partial cells have effective Doppler velocities, and the remaining cells occupied by Doppler shifts resulted from global thermal noise and even phase noise. Implementing UNRAVEL on the model where targets exist partially, the results are shown in Fig. 5.9. The RMSE between the true velocities and UNRAVEL velocities is 12.99 [m/s]. The processing ratio representing the percentage of valid data determined by UNRAVEL is 0.93.

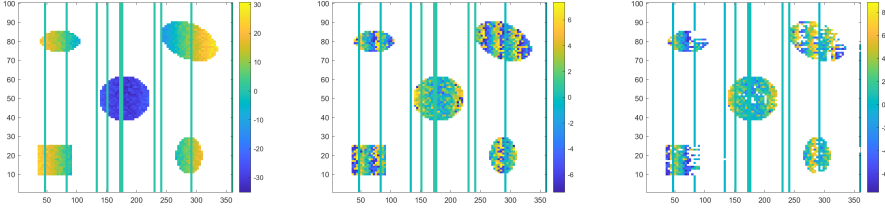


Figure 5.9: Results of UNRAVEL for Scenario: Targets Diffuse in Certain Pixels and Targets, Thermal Noise and Phase Noise All Exist

It is observed that UNRAVEL has poor performance in this simulation model. It could be possible that UNRAVEL is not tuned to the optimum configuration since this algorithm has many parameters that can be changed to fit different applications. But by now, the de-aliased real-world data provided by UNRAVEL is doubtful.

5

5.4. DOPPLER DEALIASING BY OPTIMIZER-BASED APPROACH

An optimization framework is adopted to address the issue of Doppler aliasing and estimate the true velocity-azimuth curve. With real-world data, for each range gate, the velocity-azimuth points V_R can be denoted as:

$$V_R = \{v_{R_1}, v_{R_2}, v_{R_3}, \dots, v_{R_n}\} \quad (5.7)$$

Under the assumption and equation 5.6 introduced in the previous sections, the mathematical model used to represent the expected true velocities V_E and folded velocities V_F are defined as

$$v_{E_i} = A \cos(a_i + \phi) + G \quad (5.8)$$

$$\text{and } v_{F_i} = \text{mod}(v_{E_i} + v_{\text{unamb}}, 2v_{\text{unamb}}) - v_{\text{unamb}} \quad (5.9)$$

where a_i is the corresponding azimuth, A , ϕ , and G are the parameters to estimate.

Considering the complexity of computing the gradient of the objective function with regards to the three parameters, the objective function is formulated as the MSE between the model predictions and the observed velocity-azimuth points instead of RMSE, and it is given by:

$$\text{MSE} = f = \frac{1}{N} \sum_{i=1}^N (v_{R_i} - v_{F_i})^2 \quad (5.10)$$

where N is the number of non-"NaN" values in the set V_R , i.e., $N = |\{v_{R_i} \in V_R : v_{R_i} \text{ is not NaN}\}|$. This MSE quantifies the discrepancy between the predicted velocities and the actual observed velocities. The goal of such an optimization problem is to determine the optimal values for the parameters A , ϕ and G that minimize the MSE between the model of folded velocities V_F and the observed velocity-azimuth points V_R .

The cost is measured as the root square of the objective function to facilitate consistency when comparing performance with the gradient-based approach and UNRAVEL.

5.4.1. DEVELOPMENT

To estimate the optimal parameter values, an optimization algorithm was employed. MATLAB optimizers such as "fmincon", "patternsearch", and "particleswarm" are utilized. The optimization algorithm adjusted the parameters iteratively, aiming to minimize the objective function and find the best possible fit between the predicted model and the observed velocity-azimuth points.

Three factors could affect the optimization: max actual velocity, max fluctuation caused by global noise and phase noise, and the fraction of missing values determined by the circular variance. The robustness of optimizers could be evaluated by the difference between the actual value and estimation value of three parameters a , ϕ , and G . The results of the simulation are obtained in three scenarios:

1. Change the max velocity;
2. Generate the fluctuation randomly and then use the Monte-Carlo method to remove the bias;
3. Generate the location of missing values randomly with the controllable fraction.

Here are the explanation and simulation results of the optimizers:

"FMINCON" OPTIMIZER

The "fmincon" function is designed for solving constrained nonlinear optimization problems. It stands for "function minimization under constraints". The main purpose is to find the local minimum of a given objective function while considering constraints on the variables involved. The function takes into account the problem's nonlinear nature and can handle problems with both continuous and discrete variables.

The algorithm implemented in "fmincon" is based on a combination of interior point and sequential quadratic programming methods. It uses iterative techniques to search for the optimal solution by gradually refining the estimate. With a wise starting guess to avoid the algorithm running too long, it can find the first-order optimality in the region defined by the low and upper bounds of parameters based on the derivative rule. In this case, The low and upper bounds are determined by nature law. According to the equations 5.9 and 5.10, the gradient with respect to A , ϕ , and G can be computed as:

$$\nabla_A f = -2 \cdot \frac{\sum_{i=1}^N (v_{R_i} - v_{F_i})}{N} \cdot \sin(a_i + \phi) \quad (5.11)$$

$$\nabla_\phi f = -2 \cdot \frac{\sum_{i=1}^N (v_{R_i} - v_{F_i})}{N} \cdot A \cdot \cos(a_i + \phi) \quad (5.12)$$

$$\nabla_G f = -2 \cdot \frac{\sum_{i=1}^N (v_{R_i} - v_{F_i})}{N} \quad (5.13)$$

where N is the number of non-"NaN" values in the set V_R , i.e., $N = |\{v_{R_i} \in V_R : v_{R_i} \text{ is not NaN}\}|$.

Scenario 1: Different Max Velocities

For the "fmincon" optimizer, the performance for different max velocities is shown in Fig. 5.10.

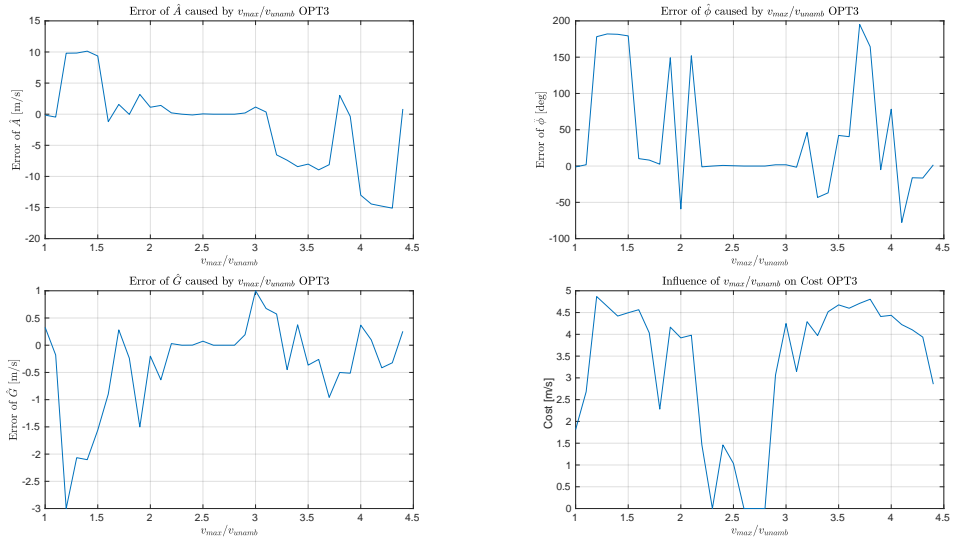


Figure 5.10: Performance of "fmincon" Optimization for Different Actual Max Velocities

Scenario 2: Different Fluctuation

Changing the maximum fluctuation, the performance of the "fmincon" optimizer is shown in Fig. 5.11.

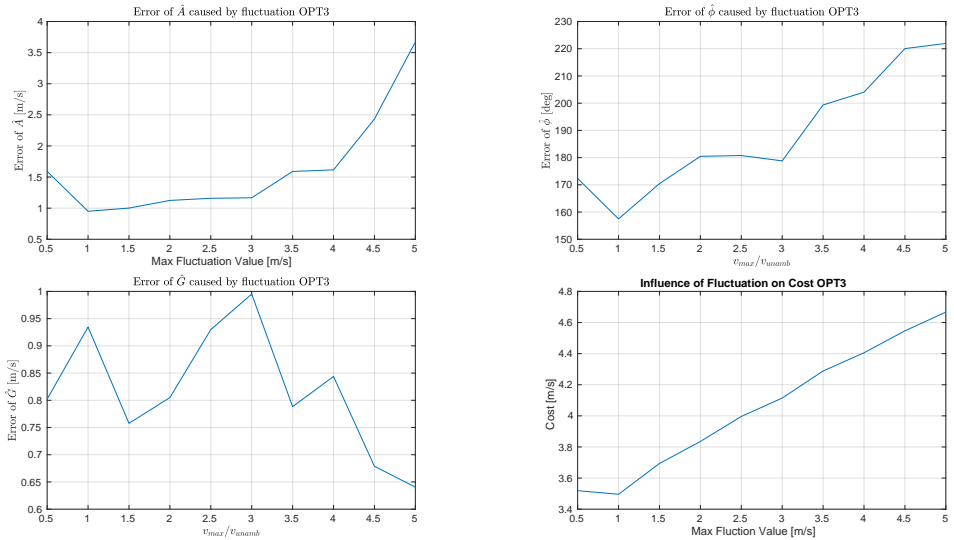


Figure 5.11: Performance of "fmincon" Optimization for Different Fluctuations Caused by Noise

Scenario 3: Different Fractions of Missing Values

Changing the fraction of missing values, which could represent the invalid data caused by noise, the performance of the "fmincon" optimizer is shown in Fig. 5.12.

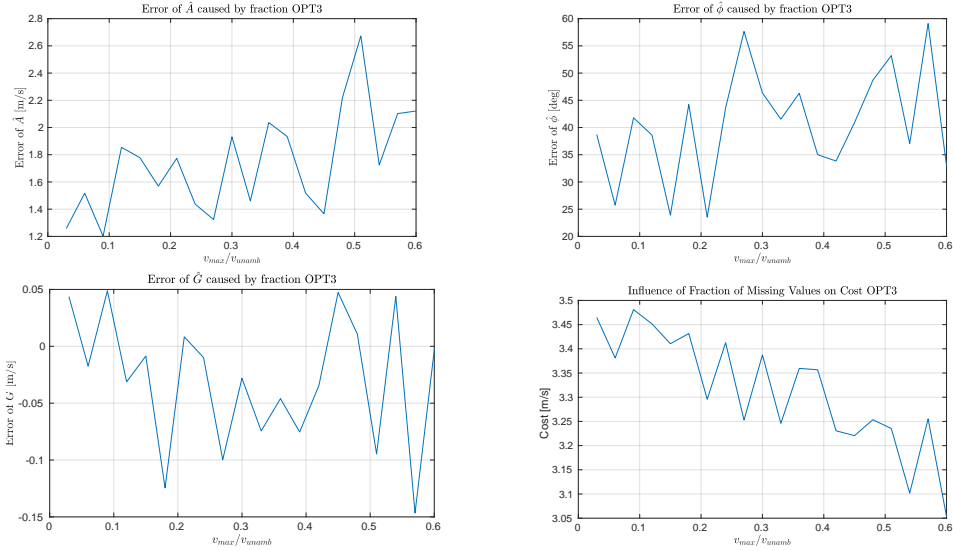


Figure 5.12: Performance of "fmincon" Optimization for Different Fractions of Invalid Data Caused by Noise

From the figures about "fmincon" above, it can be observed that:

1. The estimation of the parameters A , ϕ , and G is the most sensitive to the changing of max velocities.
2. The cost, which means the RMSE between the estimation Doppler and actual Doppler, increases as the increasing fluctuations. However, the cost has a decreasing trend as the fraction increases. It can be explained as the valid data becomes less.

"PATTERNSEARCH" OPTIMIZER

The "patternsearch" function is a robust optimization algorithm used to find the minimum of a nonlinear, continuous, or integer-valued multi-variable function. Different from "fmincon", "patternsearch" finds the global minimum of a given objective function without requiring any derivative information. Instead, it explores the parameter space by iteratively probing different points, seeking to converge to the optimal solution while maintaining the integrity of the search pattern. The algorithm starts with an initial guess and successively generates new candidate points based on certain patterns or directions. The algorithm aims to find the best solution or a close-to-best solution by trying out different options and evaluating its success using a variety of methods, including polling and pattern moves. This is done by testing the objective function at these candidate points. The performance of this optimizer is shown in Fig. 5.13, 5.14, and 5.15.

Scenario 1: Different Max Velocities

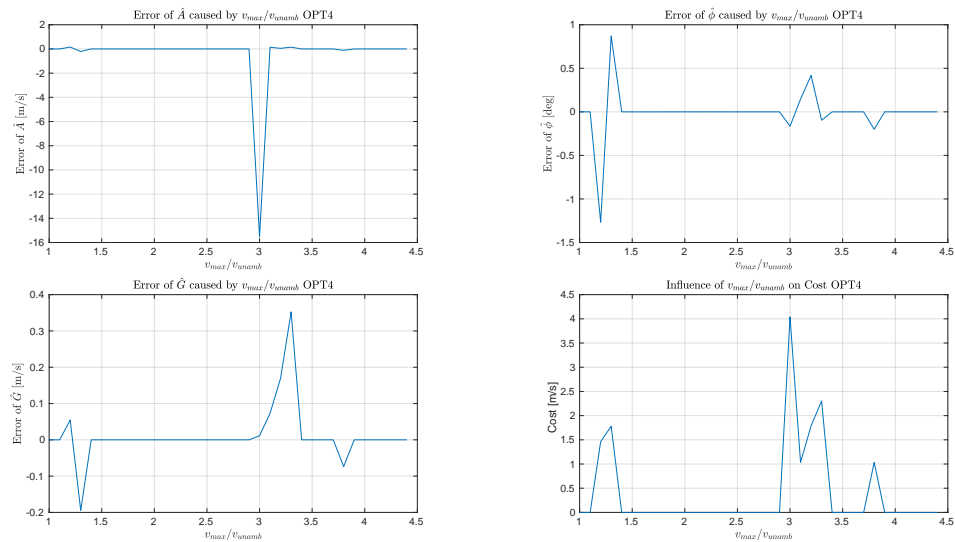


Figure 5.13: Performance of "patternsearch" Optimization for Different Actual Max Velocities

Scenario 2: Different Fluctuations

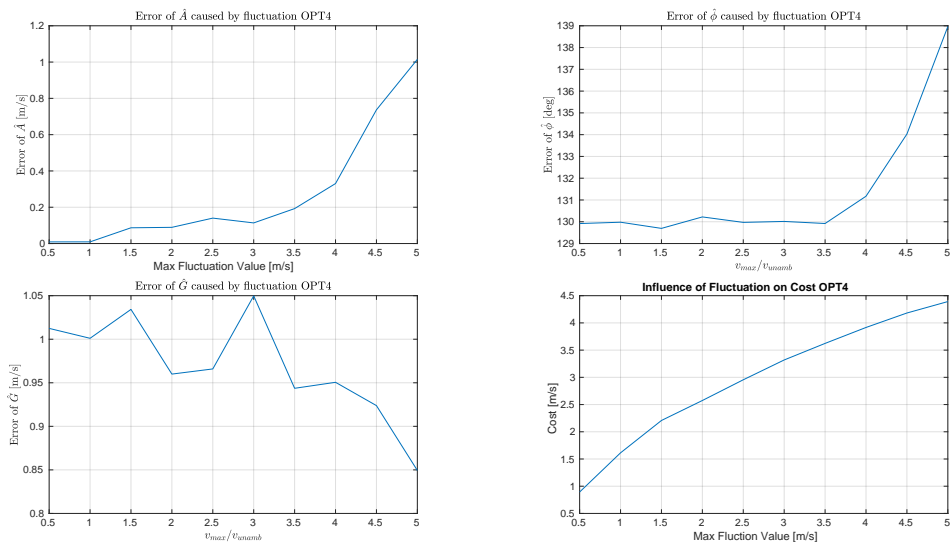


Figure 5.14: Performance of "patternsearch" Optimization for Different Fluctuations Caused by Noise

Scenario 3: Different Fractions of Missing Values

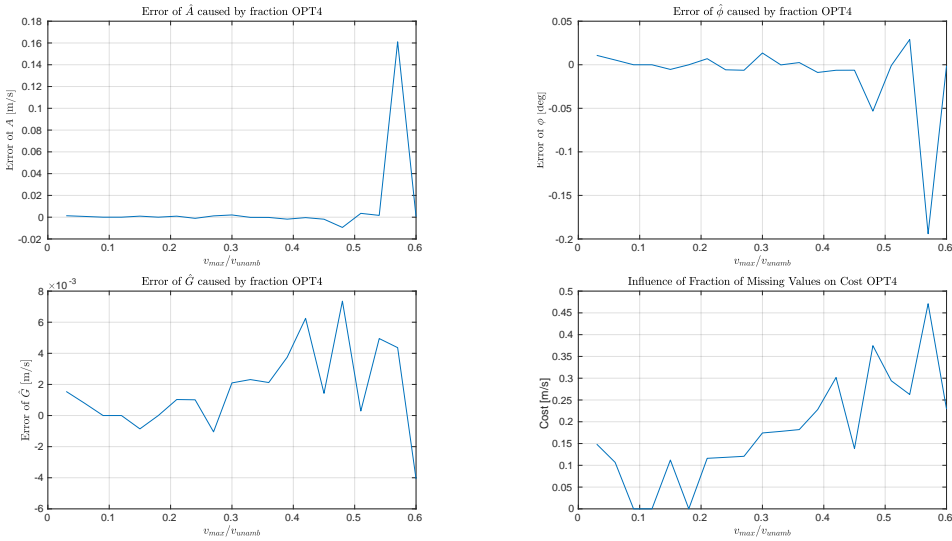


Figure 5.15: Performance of "patternsearch" Optimization for Different Fractions of Invalid Data Caused by Noise

It can be noticed from the figures about "patternsearch" above that:

1. When confronted with scenarios involving different maximum velocities, the parameter estimations for A , ϕ , and G exhibit a significantly higher degree of proximity to the actual values. This "patternsearch" optimizer's distinct performance is notably superior to that achieved by the "fmincon" optimizer. The "patternsearch" optimizer consistently achieves remarkably accurate Doppler retrievals in certain instances.
2. In scenario 3, where the fraction of missing values changes, the "patternsearch" optimizer has negligible errors about the estimation of G .
3. Nonetheless, it's important to acknowledge that the "patternsearch" optimization technique is not immune to significant errors, particularly in random cases. This susceptibility stems from its heightened sensitivity to the initial guess or starting point. If the initial estimate deviates markedly from the actual state, "patternsearch" may face challenges in convergence, and there's a potential for it to converge to a local minimum rather than the desired global minimum.

To delve deeper into the origins of pronounced errors occurring in random instances, the objective function is simplified to depend on two essential parameters: A and ϕ . This simplification offers a foundation for analyzing the optimization process more comprehensively. To gain visual insight, a meticulous investigation of the optimization plane is

depicted in Fig. 5.16. Discernible is that the objective function takes the form of a non-convex multimodal landscape characterized by the presence of multiple local minima.

The complexity inherent in this field of optimization, combined with the sensitivity of the "patternsearch" method to initial approximations, highlights its sensitivity to challenges in ensuring accurate convergence. Specifically, "patternsearch" tends to get stuck in local minima rather than trying to reach a global minimum.

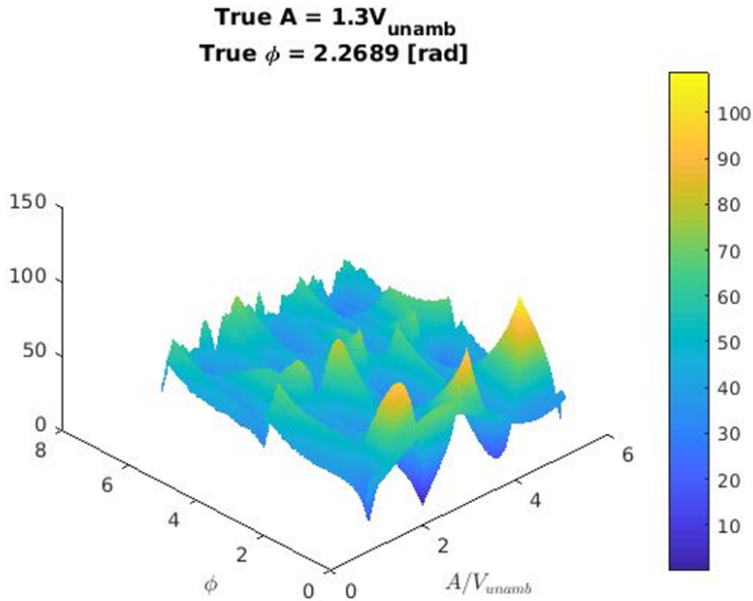


Figure 5.16: Dependence of Objective Function on Parameters for Optimization Process

"PARTICLESWARM" OPTIMIZER

The "particleswarm" function implements the particle swarm optimization (PSO) algorithm. PSO was proposed by Kennedy and Eberhart in 1995 [35]. As stated in the original paper, socio-biologists posit that a collective behavior observed in a school of fish or a flock of birds allows them to "benefit from the collective knowledge of all members." In simpler terms, when a bird, for instance, is flying and randomly searching for food, its discoveries can be shared among all the birds in the flock, leading to an optimized hunting experience for the entire group.

It's noteworthy that the Particle Swarm Optimization (PSO) algorithm is particularly adept at handling non-convex and multimodal functions due to its capacity to adeptly traverse the search space, thereby avoiding local optima. The ability of PSO to maintain distinct sets of particles empowers it to concurrently explore multiple solution regions, rendering it especially advantageous for non-convex problems that involve numerous local minima.

Drawing inspiration from the collective foraging behavior of birds, the Particle Swarm Optimization (PSO) algorithm commences its journey by dispersing a collection of par-

ticles randomly. Each of these particles undertakes an independent quest to uncover the minimum point within the objective function landscape, setting off in diverse random directions.

Throughout each iteration, every particle's exploration unfolds across two avenues: it scrutinizes the region surrounding the smallest point it has encountered hitherto, and concurrently, it takes into account the smallest point identified collectively by the entire assemblage of particles.

As the optimization process progresses through a series of iterations, the particle swarm collectively navigates this dynamic landscape, eventually converging to a specific point that attains the role of the function's global minimum.

Similar to "patternsearch", "particleswarm" is a derivative-free global optimization method. It is designed to solve unconstrained optimization problems, seeking the minimum or maximum of a given objective function without requiring derivative information. In gradient descent, the minimum of a function $f(X)$ is found by moving X to the direction of $-\nabla f(X)$ as it is where the function goes down the fastest. For any particle at the position X at the moment, how the particle moves does not depend on which direction is the "downhill" but only on where are the best position ever found thus far.

For the "particleswarm" optimizer, the performance for different max velocities is shown in Fig. 5.17, 5.18, and 5.19. Some observations are described after the figures.

Scenario 1: Different Max Velocities

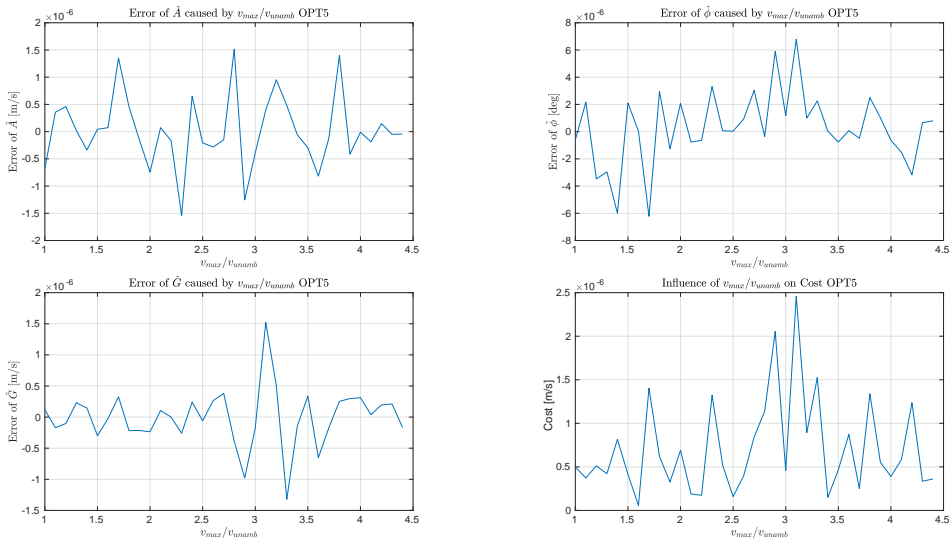


Figure 5.17: Performance of "particleswarm" Optimization for Different Actual Max Velocities

Scenario 2: Different Fluctuations

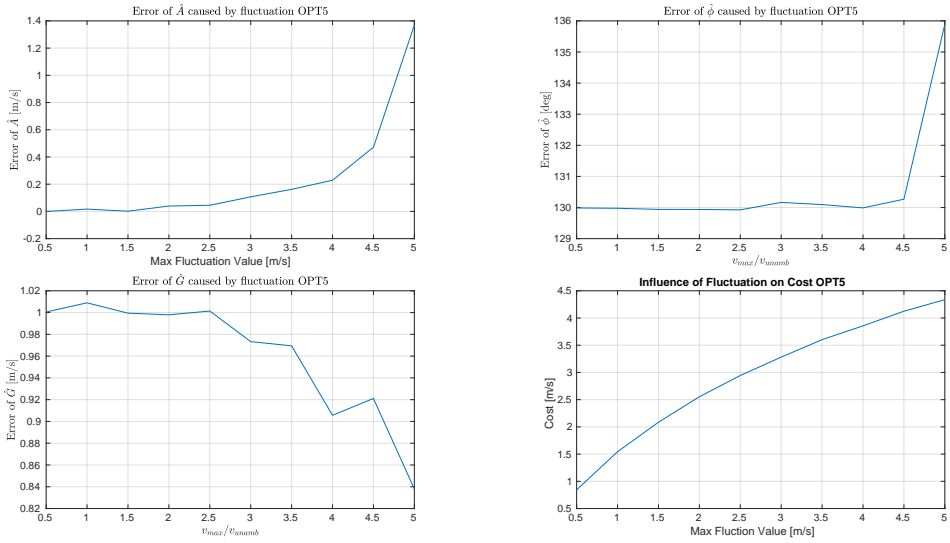


Figure 5.18: Performance of "particleswarm" Optimization for Different Fluctuations Caused by Noise

Scenario 3: Different Fractions of Missing Values

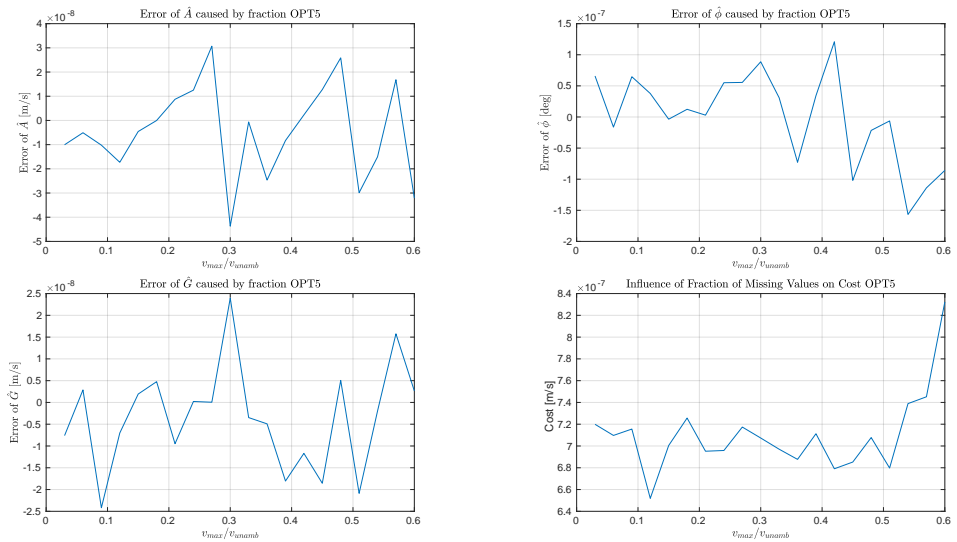


Figure 5.19: Performance of "particleswarm" Optimization for Different Fractions of Invalid Data Caused by Noise

The observations from the figures about "particleswarm" above consist of:

1. In the first and third scenarios, "particleswarm" has insignificant errors, which means it can retrieve the Doppler velocity well.
2. In the second scenario, the "particleswarm" optimizer has an increasing tendency. At an explicit velocity of 7.3938 [m/s], the fluctuation value increases to 5 [m/s]. In real-world radar measurements, the fluctuation caused by noise rarely has such a high value. Therefore, the error caused by fluctuation is allowable.

5.4.2. OPTIMIZATION COMPARISON

To solve the optimization problem, various algorithms are used. These algorithms iteratively adjust the values of the input variables in a way that gradually improves the value of the objective function until a satisfactory solution is found. The cost represents the value associated with a specific solution, while the objective function defines the goal of the optimization problem. The objective function, which measures the difference between the expected and actual Doppler values, is minimized by finding the optimal values for the input variables. The minimum value of the objective function is the best possible outcome according to the problem's constraints and goals. Therefore, the cost achieved after applying the Monte Carlo method can be used to evaluate the performance of three optimizers under different scenarios. The dependence of cost on parameters is plotted in figures 5.20, 5.21, and 5.22.

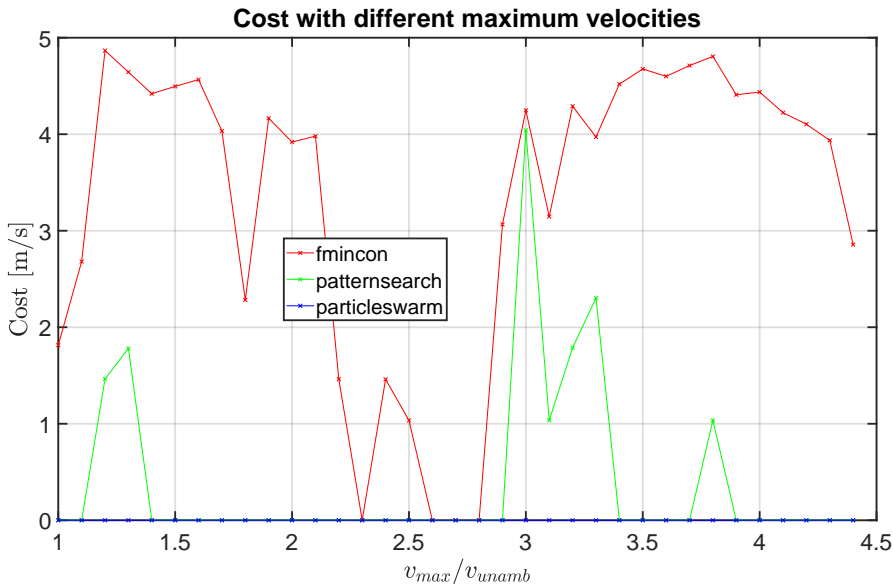


Figure 5.20: Dependence of Cost on Actual Max Velocity for Three Optimizers

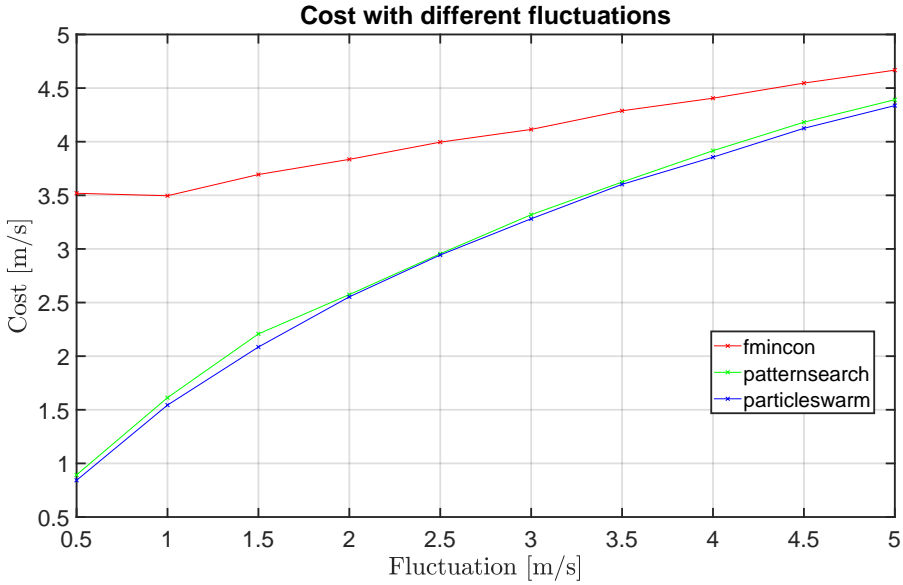


Figure 5.21: Dependence of Cost on Fluctuation Caused by Noise for Three Optimizers

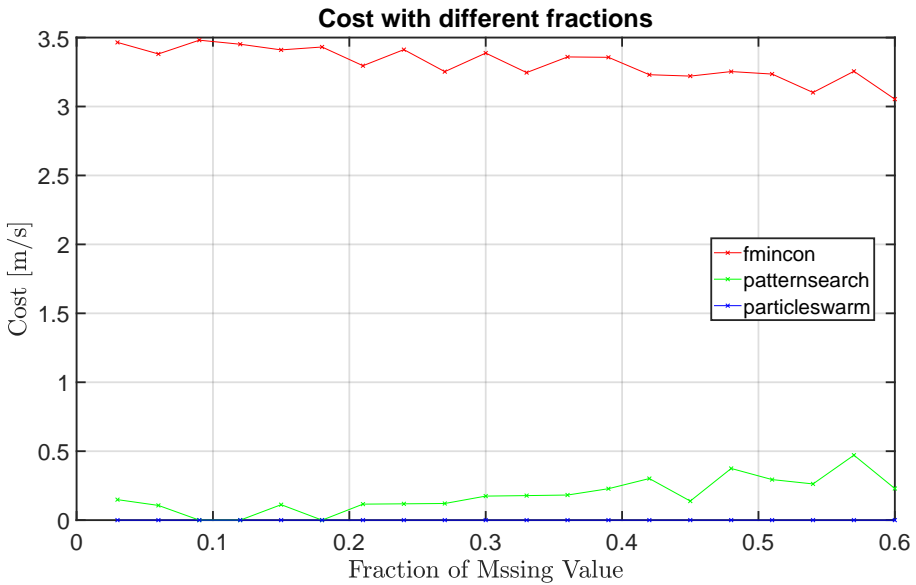


Figure 5.22: Dependence of Cost on Fraction of Invalid Data for Three Optimizers

Generally speaking, in the face of three factors that may affect the optimization performance, namely the maximum velocity, the maximum fluctuation value, and the frac-

tion of missing data, the "particleswarm" optimizer has better performance than similar optimizers. The "fmincon" optimizer has the most significant error. When the maximum velocity changes or the fraction of missing data changes, the "particleswarm" optimizer always has an error close to 0, which means it can restore the actual velocity very well. The "particleswarm" optimizer has slightly less error than "patternsearch" when subjected to different max-fluctuation values or ranges. The "particle swarm" optimizer not only demonstrates its ability to explore the search space efficiently but also ensures reliable and consistent performance even with significant modifications of the target parameters. Its robustness in adapting to these changes highlights its suitability for solving parameter Real-world optimization problems where values are uncertain or dynamically adjusted. In general, the "particleswarm" optimizer can handle fluctuations in different factors. Its resilience and versatility make it ideal in scenarios where such changes are expected or anticipated preferred.

5.5. DE-ALIASING TECHNIQUES COMPARISON

To validate the proposed "particleswarm" optimizer-based approach, the de-aliasing techniques introduced in this chapter are compared in this section by applying them to the model developed previously. Considering that UNRAVEL is only applicable for at least two-dimensional Doppler velocities, the performance of UNRAVEL can be evaluated by the RMSE and processing ratio for different scenarios, which is summarized in table 5.1.

Applying the simple algorithm and optimizer-based approaches with "fmincon", "patternsearch", and "particleswarm" to the model introduced in Fig. 5.3, the de-aliased results are shown in Fig. 5.23.

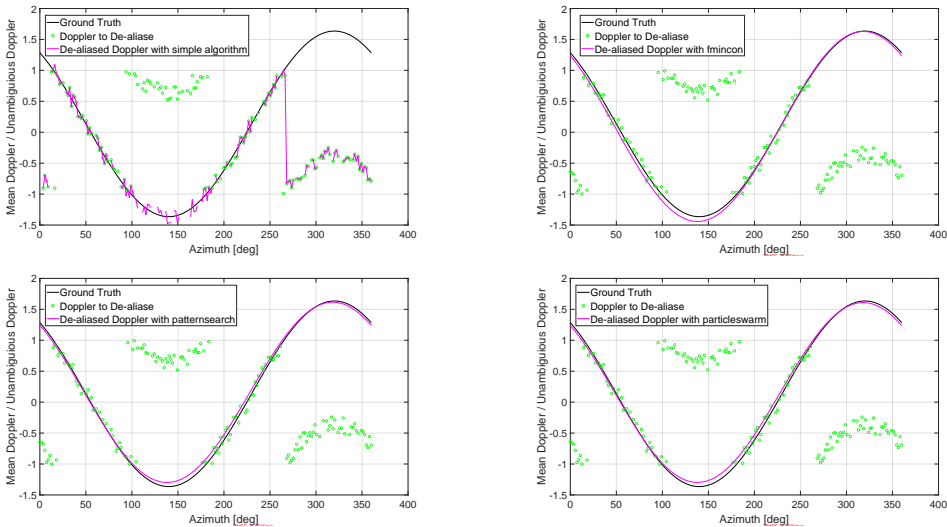


Figure 5.23: Comparison of De-aliasing Techniques

The RMSE between the de-aliased Doppler and Ground Truth using different techniques are concluded in table 5.2, from which the "particleswarm" optimizer-based approach is proven to have the least error.

Error	RMSE [m/s]
Gradient-based Simple Algorithm	8.0927
fmincon	3.1891
patternsearch	2.4936
particleswarm	2.4929

Table 5.2: RMSE of Doppler De-aliasing Techniques

5.5.1. OPTIMIZATION RESULT

With the analysis above, the "particleswarm" optimizer has been proven to have the lease error. Applying the "particleswarm" optimizer to the filtered Mean Doppler, which was introduced previously, the de-aliased Doppler is shown in Fig. 5.24.

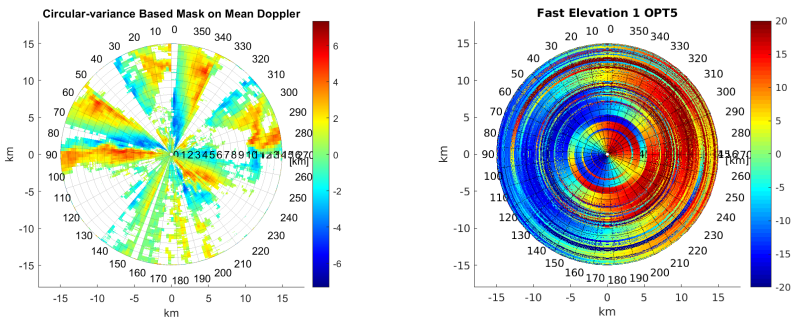


Figure 5.24: Before and After Optimization Doppler Velocity

5.6. CONCLUSIONS

This chapter compares three approaches to solving the Doppler aliasing problem: a simple algorithm based on continuity along the range dimension, an advanced existing UNRAVEL algorithm, and an optimizer-based approach. Due to the lack of ground truth of the real-world observations, the Doppler velocity model is developed to validate the techniques, considering the effect of thermal noise(fluctuation) and the impact of phase noise (missing data). It is proven that the gradient-based algorithm is vulnerable to fluctuation, as well as UNRAVEL. The performance of algorithms can be assessed by the RMSE between de-aliased results and ground truth. It should be mentioned that during the development of the optimizer-based de-aliasing techniques, "particleswarm" was selected as the best optimizer. Then the RMSE values of the three algorithms are 8.0927, 12.99, and 2.4929 with unit m/s. With the simulation results, the "particleswarm" optimizer-based approach outperforms any other techniques proposed in this chapter. The de-aliased Doppler of the real-world observations is then obtained accordingly.

6

CONCLUSION AND RECOMMENDATIONS

6.1. CONCLUSIONS

The main objective of this thesis project is to retrieve meteorological parameters using a fast-scanning phased array radar and evaluate its performance. This thesis focuses only on precipitation-like targets (i.e., raindrops). To convert the phased array radar data into variables that help characterize the precipitation, the steps followed to achieve this goal are the following.

- Derive parameters related to precipitation;
- Propose a target mapping pipeline consisting of clipping the global thermal noise, detecting the phase noise, and eliminating the effect, thus detecting the extended targets;
- Propose a Doppler de-aliasing technique;
- validate the proposed processing pipeline and techniques;

The most commonly derived radar parameters to characterize meteorological targets are derived from the Doppler spectrum and are known as the Doppler moments, and they are:

- The reflectivity (zeroth Doppler moment) of the hydrometeors. Meteorologists are interested in reflectivity to estimate rainfall intensity and identify regions of potentially severe weather, such as intense thunderstorms.
- The mean Doppler velocity (first Doppler moment) determines the wind direction and speed. Analyzing Doppler velocities in a thunderstorm can reveal the presence of updrafts and downdrafts, essential for understanding storm dynamics and potentially severe weather events like tornadoes.

- The Doppler spectrum width (the second moment of the Doppler moment) is related to the turbulence and variability in the wind field within the radar volume. It can be used to identify areas of turbulence, microbursts, and atmospheric instability, which are crucial for aviation safety and severe weather forecasting.

Before addressing the problem of Doppler de-aliasing (Determine an accurate estimate of the location of the mean Doppler velocity outside the unambiguous velocity limit), for the problem of target mapping, we consider the problem of accurate moment estimation when Doppler aliasing takes place. This is due to the fact that the existing linear Doppler moment estimators tend to provide erroneous estimates of Doppler moments when Doppler aliasing takes place. Considering the folding nature of the Doppler spectrum, a novel calculation of the spectrum moments based on circular statistics (see chapter 3) is proposed in this thesis. To our best knowledge, linear moment estimation and shift-back estimation are the most common-used methods when it comes to calculating the mean Doppler and spectrum width [36]. I suggest circular moment estimation using Batschelet's theory [30] and Mardia's theory [31]. The comparative results (Fig. 3.3 and Fig. 3.2) suggest that the circular moment estimation using Mardia's theory has the least error. The circular moment estimates, especially the Doppler spectrum width, are immune to the effect of Doppler aliasing.

To the author's knowledge, for the first time, a target mapping technique based on circular variance is proposed. This approach proved particularly valuable in scenarios where traditional reflectivity-based target mapping approaches fall short, such as situations dealing with unknown size and unknown shape diffused targets. The results indicated that the circular variance-based target mapping technique can provide comprehensive and accurate information about the observed targets.

Besides the circular variance-based target mapping technique, two target mapping pipelines with a focus on reflectivity are proposed. Each of them is a combination of various existing techniques. By analyzing the characteristics of the point targets, extended targets of interest, thermal noise, and phase noise, the 2D target reflectivity model is developed to validate the reflectivity-based pipelines.

The first one, which is a morphology-based pipeline, consists of the following steps: (1). Point target detection using CFAR; (2). Phase noise detection and then nullified by thresholding the mean value along the range dimension; (3). Denoise using wavelet techniques; (4). Morphological operation to detect the target of interest; (5). Restoring the phase noise azimuths and morphological filling of the gaps.

The second one, which is an entropy-based target mapping pipeline, includes: (1). Point target identification using CFAR along range; (2). Thermal noise identification with threshold provided by Renyi's entropy; (3). Phase noise detection by combining the CFAR detector along the azimuth and thresholding the normalized mean along the range.

By evaluating the performance of the simulation model, it can be concluded that in the cases where SNR is below -15dB, the entropy-based pipeline is better, with 0.0409 less IoU, 0.0879 less false alarm rate, 0.4715 more missed detection, and 0.0646 less F1Score. While in the cases above -15 dB, the morphology-based pipeline works better, with 0.2015 more IoU, 0.1495 less false alarm rate, 0.1008 less missed detection, and 0.1354 more F1Score. The two pipelines are also implemented on real-world data. And since the extended targets have diffused shapes and sizes, the entropy-based pipeline

has a better outcome than the morphological-based one. Another advantage of the entropy-based pipeline is that it can provide an overview of the data types existing in the radar measurements.

As the velocities of raindrops in severe storms can exceed the maximum unambiguous velocity defined by the radar pulse repetition frequency, aliasing (folding) takes place in the Doppler spectrum, greatly affecting the moment computation. The existing Doppler de-aliasing techniques are mostly about checking the continuity from range(1D), azimuth(2D), elevation (3D), and even temporal (4D), stated in the chapter 2. Assuming that wind speed and direction are constant within the radar scan coverage. The wind-originated Doppler velocity as a function of the azimuth is modeled as a cosine curve. According to the cost function introduced in chapter 5, a Doppler dealiasing technique based on the "particleswarm" optimizer was proposed for the first time. The algorithm has been applied both to computer-simulated and real radar observations. This approach offers enhanced accuracy and reliability, enabling more precise velocity measurements for various applications, including weather forecasting, aviation, and wind energy.

In conclusion, the calculation of Doppler spectrum moments that are related to the meteorological objects of interest was introduced in chapter 3 with the novel circular spectrum moments estimation. The target mapping algorithm based on the circular variance was proposed in the chapter 3. The target mapping pipelines based on reflectivity were proposed in chapter 4, with the simulation model and validation results. The "ParticleSwarm" optimizer-based Doppler dealiasing technique was concluded as the best approach to dealise Doppler in chapter 5.

6.2. RECOMMENDATIONS

Due to the time limitation, the following research is not included in the scope of this thesis project. It is recommended to explore the integration of circular calculation and circular variance-based techniques with advanced machine learning algorithms, particularly deep learning, to enhance target classification and identification. By leveraging the power of machine learning, the accuracy and efficiency of target mapping can be further improved.

For the morphology-based target mapping pipeline, exploring different morphological operations and structuring elements tailored to specific target features is suggested to improve pipeline performance in complex scenarios. As for the entropy-based pipeline, the sensitivity of parameters existing in the entropy theory on the performance of distinguishing different distributions is recommended for further study.

Regarding Doppler dealiasing techniques, it is recommended to improve and refine the Doppler velocity model closer to real-world scenarios.

Additionally, to ensure the effectiveness and reliability of the proposed techniques, it is suggested to extend the evaluation and selection process beyond simulation data. Real-world data from diverse meteorological scenarios should be thoroughly analyzed and validated to ascertain the practical applicability and generalizability of the proposed methods.

By considering these recommendations, future research can continue to advance radar data processing for meteorological applications, enhancing the accuracy and reli-

ability of weather-related analyses and forecasting tasks.

REFERENCES

- [1] A. W. Doerry, "Radar receiver oscillator phase noise," Apr. 2018.
- [2] K. Siddiq, R. J. Watson, S. R. Pennock, P. Avery, R. Poulton, and B. Dakin-Norris, "Phase noise analysis in fmcw radar systems," in *2015 European Radar Conference (EuRAD)*, 2015, pp. 501–504.
- [3] V. Bringi and V. Chandrasekar, *Polarimetric Doppler Weather Radar: Principles and Applications*. Cambridge University Press, Cambridge, New York, 2001, pp. 211–294.
- [4] Y. Hong, J. Zhang, and Z. Pu, "A review of phased array weather radar signal processing: Current status and future trends," *Proceedings of the IEEE*, vol. 101, pp. 583–603, 2013.
- [5] Z. D. S., "Quality control of doppler radar data," *Journal of Atmospheric and Oceanic Technology*, vol. 7, pp. 596–608, 1990.
- [6] W.C.Lee and I.Zawadzki, "Quality control of radar reflectivity data for rainfall estimation," *Journal of Atmospheric and Oceanic Technology*, vol. 22, pp. 1694–1709, 2005.
- [7] V. G. Krajewski, W. F. Smith, J. A., and N. A. A., "Quality control of radar-based precipitation measurements: A critical review," *Water Resources Research*, vol. 45, 2009.
- [8] M. A. Richards, *Fundamentals of Radar Signal Processing, Second Edition*. McGraw-Hill Education, 1976, pp. 496–538.
- [9] F. Wu, W. Yang, L. Xiao, and J. Zhu, "Adaptive wiener filter and natural noise to eliminate adversarial perturbation," *Journal of Electronics*, vol. 9, pp. 1–14, 2020.
- [10] H.-W. Chen, C. Volpe, M. Tarnowski, and S. Snarski, "Robust extended target detection using nonlinear morphological operations," in *Proceedings of SPIE - The International Society for Optical Engineering*, SPIE Defense, Security, and Sensing, vol. 7694, 2010.
- [11] M. Berenguer, D. Sempere-Torres, C. Corral, and R. Sanchez-Diezma, "A fuzzy logic technique for identifying nonprecipitating echoes in radar scans," *Journal of Atmospheric and Ocean Technology*, vol. 23, pp. 1157–1180, 2006.
- [12] M. M. R. and A. G., "Fuzzy logic and singular value decomposition based through wall image enhancement," *Radio Engineering*, vol. 21, pp. 580–589, 2012.
- [13] S. N. Wijesundara, K. L. Bell, G. E. Smith, and A. O'Brien, "Comparison of maximum-likelihood estimation and other methods for clutter doppler centroid estimation," *IEEE Transactions on Aerospace and Electronic Systems*, vol. 55, pp. 2359–2369, 2019.

- [14] E. Masazade, A. K. Bakir, and P. Kirci, "A kalman filter application for rainfall estimation using radar reflectivity measurements," *Turkish Journal of Electrical Engineering and Computer Sciences*, vol. 27, pp. 1198–1212, 2019.
- [15] M. Kazemisaber, "Clutter removal in single radar sensor reflection data via digital signal processing," Linnaeus University, Jun. 2020.
- [16] C. Chinrungrueng, "Combining savitzky-golay filters and median filters for reducing speckle noise in sar images," in *Systems, Man and Cybernetics, 2003. IEEE International Conference*, IEEE Xplore, vol. 1, 2003.
- [17] D. N. Moisseev and V. Chandrasekar, "Polarimetric spectral filter for adaptive clutter and noise suppression," *Journal of Atmospheric and Oceanic Technology*, vol. 26, pp. 215–228, 2009.
- [18] A. K. C. Jaideva C. Goswami, *Fundamentals of Wavelets: Theory, Algorithms, and Applications*. John Wiley and Sons, Inc., 2010, pp. 94–307.
- [19] B. P. Epps and E. M. Krivitzky, "Singular value decomposition of noisy data: Noise filtering," *Experiments in Fluids*, vol. 60, pp. 126–150, 2019.
- [20] R. P. S. and C. Ziegler, "De-aliasing first-moment doppler estimates," *Appl. Meteor.*, vol. 16, pp. 563–564, 1977.
- [21] Z. J. and S. Wang, "An automated 2d multipass doppler radar velocity dealiasing schem," *Atmos. Oceanic Technol.*, vol. 23, pp. 1239–1248, 2006.
- [22] B. W. R. and S. C. Albers, "Two- and three-dimensional de-aliasing of doppler radar velocities," *Atmos. Oceanic Technol.*, vol. 5, pp. 305–319, 1988.
- [23] L. E. and J. Sun, "A velocity dealiasing technique using rapidly updated analysis from a four-dimensional variational doppler radar data assimilation system," *Atmos. Oceanic Technol.*, vol. 27, pp. 1140–1152, 2010.
- [24] E. M. D. and S. D. Smith, "Efficient dealiasing of doppler velocities using local environment constraints," *Atmos. Oceanic Technol.*, vol. 7, pp. 118–128, 1990.
- [25] G. J. L. L. Wang and Q. Xu, "A three-step dealiasing method for doppler velocity data quality control," *Atmos. Oceanic Technol.*, vol. 20, pp. 1738–1748, 2003.
- [26] V. Louf, A. Protat, R. C. Jackson, S. M. Collis, and J. Helmus, "Unravel: A robust modular velocity dealiasing technique for doppler radar," *Journal of Atmospheric and Oceanic Technology*, vol. 37, no. 5, pp. 741–758, May 2020, ISSN: 15200426. DOI: 10.1175/JTECH-D-19-0020.1.
- [27] D. S. Zrnić, "Simulation of weather-like doppler spectra and signals," *Journal of Applied Meteorology and Climatology*, vol. 4, pp. 619–620, 1975.
- [28] J. K. R. and R. E. Passarelli, *Signal processing for atmospheric radars*. National center for atmospheric research Boulder, Colorado, 1989, p. 25.
- [29] Kanti V. Mardia and Peter E. Jupp, "Directional Statistics," Tech. Rep.
- [30] E. Batschelet, *Circular Statistics in Biology* (Mathematics in biology). Academic Press, 1981.

- [31] P. E. J. Kanti V.Marida, *Dirctional Statistics* (Circular Data). John Wiley and Sons, Inc, 2000.
- [32] M. Fang and R. Doviak, "Spectrum width statistics of various weather phenomna." [Online]. Available: <https://api.semanticscholar.org/CorpusID:36383393>.
- [33] M. El-Sayed and M. Ahmed, "Using renyi's entropy for edge detection in level images," vol. 11, pp. 1–11, Jan. 2011.
- [34] L. Shuyuan, W. Hongqing, and T. Zuyu, "A simple algorithm for eliminating doppler velocity aliasing," *Department of Atmospheric Science, Peking University*,
- [35] J. Kennedy and R. Eberhart, "Particle swarm optimization," in *Proceedings of ICNN'95 - International Conference on Neural Networks*, vol. 4, 1995, 1942–1948 vol.4.
- [36] R. F. Woodman, "Spectral moments estimation in mst radars," *Radio Science*, vol. 20, pp. 1185–1195, 1985.